Influence of cosmic radiation on aerosol and cloud formation over short time periods

Bondo, Torsten

Publication date:
2010

Document Version
Publisher's PDF, also known as Version of record

Influence of Cosmic Radiation on Aerosol and Cloud Formation over Short Time Periods

National Space Institute

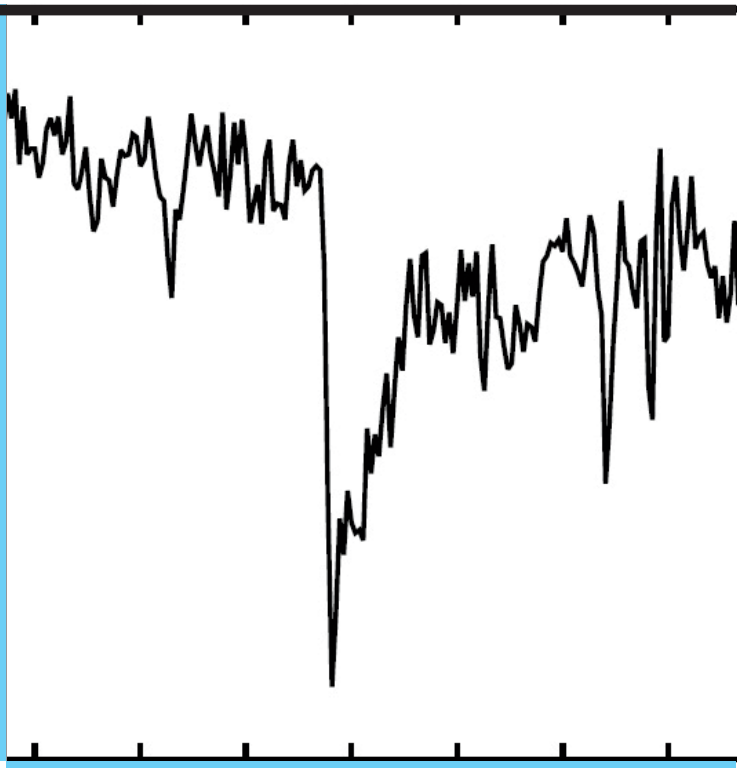

Torsten Bondo
PhD Thesis
December 2009

DTU Space
National Space Institute

Influence of Cosmic Radiation on Aerosol and Cloud Formation over Short Time Periods
PhD thesis by Torsten Bondo
December 2009

Financed by National Space Institute, DTU Space
Supervised by Henrik Svensmark, National Space Institute, DTU Space
ISBN 978-87-92477-05-7

Technical University of Denmark
Juliane Maries Vej 30
DK-2100 København Ø
www.space.dtu.dk

Abstract

This thesis describes a study of Forbush decrease events. These are rapid decreases in the cosmic ray intensity in the Earth's atmosphere, which are caused by a temporary increased magnetic shielding at Earth due to solar eruptions. The aim is to investigate how these transient ionization phenomena in the atmosphere affect aerosol and cloud creation and whether it is realistic to observe Forbush decrease events in climate data.

The thesis involves a theoretical examination of the ionization caused by Forbush decreases based on studies of hourly neutron monitor data and muon telescope data as proxies for cosmic rays. A list of the ionization change in the troposphere of the strongest Forbush decreases as compared to the ionization change over the solar cycle is calculated and indicates that only a few events induce ionization changes comparable to the solar cycle.

Studies of recently available high resolution satellite data and aerosol ground based measurements are presented. Here it is observed that significant decreases in the angstrom exponent from AERONET aerosols and cloud liquid water from satellites take place after the largest Forbush decreases. The timescales of this indicate that the ionization decrease caused by the Forbush decreases diminishes the aerosol nucleation rate which, over time, affects first cloud condensation nuclei size aerosols and then clouds.

As a part of the thesis, a model of the growth of neutral sulfuric acid aerosols has been developed. Assuming an initial distribution of stable nucleated clusters, the model takes condensation and coagulation into account and includes various loss mechanisms. This model is used to investigate the growth of aerosols into cloud condensation nuclei size particles and to study the influence of nucleation rates and background vapour gas concentration on aerosol and cloud optical properties over short time. The model is used to examine experimental efforts at DTU Space on the role of ions in nucleation, as well as it is used to investigate observational data on Forbush decreases in aerosols. The model confirms the existence of decreases in angstrom exponents observed in AERONET aerosol data under assumption of realistic ion induced nucleation rates.

The work presented in the thesis indicate that the largest Forbush decreases affect aerosol formation and in turn cloud cover on a global scale.

Resume på dansk (Abstract in Danish).

Under voldsomme soludbrud kan ioniseringen i Jordens atmosfære formindskes over et par timer for derefter at genfinde samme niveau i løbet af et par dage. Dykket i ionisering kaldes et Forbush decrease og sker som følge af en midlertidig forstærkelse af solvinden. Da solvinden udgør den magnetiske afskærming fra de kosmiske stråler, der danner ioniseringen i Jordens atmosfære, kan soludbruddet forårsage dyk i ioniseringsniveauet i atmosfæren. Denne afhandling omhandler effekten af dykket i ionisering under et Forbush decrease på aerosoldannelse og skydannelse.

Afhandlingen præsenter en teoretisk gennemgang af, hvordan ioniseringen ændres under et Forbush decrease, og en liste af Forbush decreases angives ud fra hvor meget ændring i ionisering hver event forårsager i forhold til ioniseringsændringer over den 11 årige solcyklus. Denne liste bruges som udgangspunkt for en analyse af Forbush decrease effekter i skydata fra satellit og aerosoldata fra jordstationer. Her observeres tydelige dyk i både aerosol og skydata efter de største Forbush decreases.

Den sidste del af afhandlingen beskriver udviklingen af en aerosol vækstmodel, der kan modellere væksten af neutrale svovlmolekuler. Modellen anvendes til at analysere eksperimentelle studier foretaget på DTU Space af ioners indvirkning på aerosol dannelse. Til sidst modelleres de observationelle resultater af Forbush decreases i aerosol data.

Afhandlingens resultater indikerer at de største Forbush decreases er i stand til at påvirke aerosol- og skydannelse på et globalt plan.

Contents

List of Figures

List of Tables

List of Abbreviations

AE	Angstrom Exponent
AIE	Aerosol Indirect Effect
AERONET	Aerosol Robotics Network (Holben et al., 1998)
AOT	Aerosol Optical Thickness
CCN	Cloud Condensation Nuclei
CLW	Cloud Liquid Water
CME	Coronal Mass Ejection
FD	Forbush Decrease
GHG	Green House Gases
GCR	Galactic Cosmic Rays
I	Ion Concentration
IIN	Ion Induced Nucleation
ISCCP	International Satellite Cloud Cover Project
κ	Half Life of Particles
κ_{par}	Loss Rate of Particles
k_i^c	Condensation Coefficient
$k_{i,j}^e$	Coagulation Coefficient
LCF	Liquid Cloud Fraction
MODIS	Moderate Resolution Imaging Spectroradiometer
n_i	Particle Number
$P_{H_2SO_4}$	Production Rate of Sulphuric Acid
Q	Ionization Rate
RF	Radiative Forcing
s	Production Rate of Stable Clusters
SAP	Sulphuric Acid Particles
SSM/I	Special Sensor Microwave/Imager
TSI	Total Solar Irradiance
τ	Optical Thickness
UV	Ultra Violet

Chapter 1

Scientific Papers and Reports

This thesis is a summary of the following published papers, articles in preparation and report.

Paper I Svensmark, Henrik, Bondo, Torsten and Svensmark, Jacob (2009), *Cosmic ray decreases affect atmospheric aerosols and clouds*, Geophys. Res. Lett., 36, L15101, doi:10.1029, 2009GL038429 (Svensmark et al., 2009).

Paper I examines how Forbush decreases (FDs) affect the troposphere through ionization changes. Satellite data from 3 sensors are presented as well as aerosol measurements from the ground based network AERONET (AErosol RObotic NETwork). The work presented in the paper constitutes a major part of the work behind my PhD thesis including the data analysis of the satellite measurements, neutron monitors, muon telescopes and ground based stations. The novelty of this work lies in an improved characterization of how Forbush decreases affect ionization in the lower troposphere compared to previous studies and the use of AERONET aerosol data for examining the effects of cosmic rays on clouds. The paper indicates that cloud and aerosol formation scale with the size of the Forbush decrease and take place on timescales of days related to aerosol growth to Cloud condensation nuclei sizes. Some of the work from Paper 1 and additional work from this part of my thesis is presented in Chapter 2 and 3. Other methods of determining ionization changes in the troposphere are presented in Chapter 3 and thus provides an overview of how cosmic ray induced tropospheric ionization during a Forbush decrease can be modeled.

Paper II Enghoff, Martin B., Pedersen, Jens Olaf P., Bondo, Torsten, Johnson, Matthew S., Paling, Sean and Svensmark, Henrik, *Evidence for the role of ions in Aerosol Nucleation*. Phys. Chem. A, 2008, 112 (41) (Enghoff et al., 2008).

Paper II is an extension of the experimental work on ion induced nucleation in an atmospheric chamber presented in Svensmark et al. (2007). In this paper a new and smaller atmospheric chamber is introduced and used to probe the role of ions in aerosol nucleation. The paper indicates a dependence of ionization on the number of nucleated aerosols. Together with Martin Enghoff and Freddy Christiansen, I developed the aerosol growth model which I used to examine the experimental results in the paper. The model is developed based on text book material and published articles. It represents as such not an academic novelty but it is a computationally fast and efficient code that has proved to be a useful tool related to the work of our group. The aerosol growth model is presented in the first part of Chapter 4.

Paper III: Bondo, Torsten, Enghoff, Martin B. and Henrik Svensmark. *"Model of optical response of marine aerosols to Forbush decreases"*. Atmos. Chem. Phys. Discuss., 9, 22833-22863, 2009. (Bondo et al., 2009)

The aerosol growth model is extended in **Paper III** and used in combination with a Mie Scattering program to examine the optical properties of a clean marine environment during a Forbush decrease. The idea of the paper is to perform a sensitivity study on how ionization changes during a FD affect aerosol growth by changing the atmospheric content of of sulfuric acid vapour gas, sea salt concentration and nucleation rates. It directly links to the work in Paper 1 and comparisons to the satellite observations in Paper 1 are presented. I did the programming and most of the modeling work related to this paper. This work will be presented in the second part of Chapter 4.

Paper IV: J. Duplissy, M.B. Enghoff, K.L. Aplin, F. Arnold, H. Aufmhoff, M.Avngaard, U. Baltensperger, **T. Bondo**, R. Bingham, K. Carslaw, J. Curtius, A. David,B. Fastrup, S. Gagn´e, F. Hahn, R.G. Harrison, B.Kellett, J. Kirkby,M.Kulmala, L. Laakso, A. Laaksonen, E. Lillestol1, M. Lockwood,J.Makela, V. Makhmutov, N.D. Marsh, T. Nieminen, A. Onnela,E. Pedersen, J.O.P. Pedersen, J. Polny, U. Reichl, J.H. Seinfeld, M. Sipila,Y. Stozhkov, F. Stratmann, H. Svensmark, J. Svensmark, R.Veenhof,Y.Viisanen, P.E.Wagner, G.Wehrle, E.Weingartner, H.Wex, M.Wilhelmsson, and P.M.Winkler. *"Results from the CERN pilot CLOUD experiment"*. Atmos. Chem. Phys. Discuss., 9, C5845-C5847, 2009. (Duplissy, 2009)

During the first months of my thesis, I spent a two week period at CERN working at a pilot experiment for the CLOUD experiment (http://cloud.web.cern.ch/cloud/). The CLOUD project aims to examine the influence of cosmic rays on clouds using artificially generated cosmic rays from a CERN beam. The purpose of the pilot experiment was to make initial experiments at CERN in a smaller atmospheric chamber primarily to gain insight in to how to design a bigger atmospheric CLOUD chamber. My work consisted mostly in practical aspects of running the experiment. Since **Paper IV** has little direct relevance to the thesis work, it will not be mentioned further and not be added to the Appendix.

ISAC report WP503 Marsh, Nigel and Bondo, Torsten. *ISAC report WP503*

ISAC was an European Space Agency (ESA) funded study of the Influence of Solar Activity Cycles on Earth's Climate (ISAC). The work was done in cooperation with solar physicists at the Swedish Institute of Space Physics in Lund and climatologists at the Space and Atmospherics Department, Imperial College, London and the sun-climate group at DTU Space (Christiansen et al., 2007). The study involved a literary survey of solar-climate mechanisms, data identification of relevant solar and climate data as well as in depth correlation studies of solar parameters with climate. **ISAC report WP503** is a review of the role of ionization in aerosol nucleation processes. Except for offering background information, this report has no direct relevance to the thesis and has not be added to the Appendix. The report can be downloaded from http://www.space.dtu.dk/English/Research/Projects/ISAC.aspx

Paper I, Paper II and **Paper III** can be read in their full length in Appendix D.

Chapter 2

Introduction

This chapter introduces how cosmic ray induced ionization is speculated to have an influence on aerosols, clouds and climate via an aerosol nucleation mechanism involving ions. Theory, observations and experiments of this ion aerosol mechanism is given. Last, by introducing Forbush decreases, transient decreases in ionization caused by Solar Eruptions, the context of the thesis is made clear.

2.1 Climate Change

Climate change research aims to reach a full understanding of how Earth's climate changes over time. In order to do this each climate changing process must be understood. However, singling out the contribution from the individual processes is not an easy task since both natural as well as anthropogenic changes occur simultaneously and do take part in the same climate changing processes.

Humans affect the climate in several ways. The most common known cause of anthropogenic climate change is through the exhaust of green house gases (GHG) which can lead to surface heating by atmospheric reradiation of infrared rays from the Earth's surface. However, the climate also responds to the exhaust of aerosols and chemicals from cities and factories and changes in Earth's soil use. Deforestation by humans will both affect atmospheric carbon dioxide content and change the Earth's albedo and therefore constitute a good example of how humans affect the climate.

Climate variations can also lead to several complicated feed back processes where natural or anthropogenic heating/cooling can lead to more heating/cooling (positive or negative climate feedback). Water vapour, the most abundant GHG, varies both seasonally and regionally. An increase in water vapour leads to an increase in GHG that lead to surface warming. This warming can again lead to more evaporation and more heating. The cryosphere (sea ice and polar caps ice coverage) presents another example of the complexity of Earth's climate. Any global temperature change will eventually affect the Earth cryosphere by increasing or decreasing the amount of sea ice. This, in turn, affects the salinity content of the ocean seas which drives the thermohaline circulation (global ocean water circulation) and will lead to sea level as well as sea temperature changes followed by more heating/cooling. Regional changes occur simultaneously along with the global changes and do sometimes occur contrary to global trends. For instance a slow down of the thermohaline circulation due to an increase in Greenland and North Cap melt could lead to more extreme winters in Europe. Regions with an increase in precipitation, drought and snow fall may also occur and are important for understanding the global context.

Natural climate change has happened throughout Earth's history. Good examples of this are the Eemian inter-glacial (120.000 years ago) or the Holocene maximum (6000 years ago), where the climate was considerably warmer than today[1]. The Holocene - the past 12.000 years - is an interglacial period similar to the Eemian which has provided sufficient climate stability for the evolution of modern civilization.

Natural climate change phenomena can occur within the closed atmospheric system (internal modes of oscillation) when for example volcanos erupt or during the El Niño-Southern Oscillation where changes in the sea surface temperatures of the Eastern Pacific affect global atmospheric transport patterns such as trade winds, tropical circulation and precipitation. However, natural climate change also occurs external to the Earth atmosphere.

The Earth's orbit around the Sun also changes with time and gives rise to climate variations. Here Earth's climate changes with variations in Earth obliquity, precession, and eccentricity on time scales of 20, 40 of 100 thousand years: the Milankovich cycles. Furthermore the Solar radiation is never constant and changes with time. Since the Sun is the main energy source at Earth this will of course affect climate. Present climate models do contain reconstructions of the Sun's total radiation (TSI - Total Solar Irradiance), determined among other things from radioactive isotopes, sun faculae [2] and sun spot numbers, e.g (Solanki, 2003). Even though these reconstructions are related to some uncertainty they show that solar radiation varies on an 11 year (Schwabe), 22 year (Hale) and longer cycles, the 11 year cycle being the most pronounced. Solar physicists claim that the solar radiation has increased through the last 200 years (McCracken and Beer, 2007; Muscheler et al., 2007) and some researchers claim that there has been an increase in solar radiation over the last 20 years (Bieber et al., 2007) but there is wide consensus that TSI alone has not been the cause of the global mean temperature increase of approximately 1 degree observed over the last approx 50 years (Foukal et al., 2006).

In Figure 2.1 the changes in Earth's net irradiance budget (Radiative Forcing - RF[3]) induced by various mechanisms over the industrial time are listed as investigated by the Intergovernmental Panel On Climate Change (IPCC). The figure shows that the radiative forcing from the TSI is approximately 20 times smaller than the combined anthropogenic changes caused by an increase in emission of greenhouse gases, thereby excluding the role of direct solar radiation in present day global temperature increase (see previous paragraph).

Along with these widely accepted elements of climate change expressed by Figure 2.1, there are people working on describing alternative climate changing processes, see section 2.7.1 and Table 2.11 of Forster et al. (2007). Among these processes are indirect solar mechanisms where solar radiation changes impact certain atmospheric processes and in turn affect climate. The radiative forcing impact as well as the level of understanding of these processes are by the IPCC believed to be poorly understood and are therefore not included in Figure 2.1. But the indirect processes continues to be examined and must be understood to get the full picture of climate change.

For the purpose of this thesis, the two most notable of these indirect solar mechanisms

[1] Some researchers believe that the ice cap of Southern Greenland was reduced with as much as 25% as compared with today under the Eeemian (Johnsen and Vinther, 2007) and some claim that the Southern ice was gone (Cuffey and Marshall, 2000)

[2] Sun faculae are bright plage components at the Sun

[3] " See Forster et al. (2007) for a more precise definition.

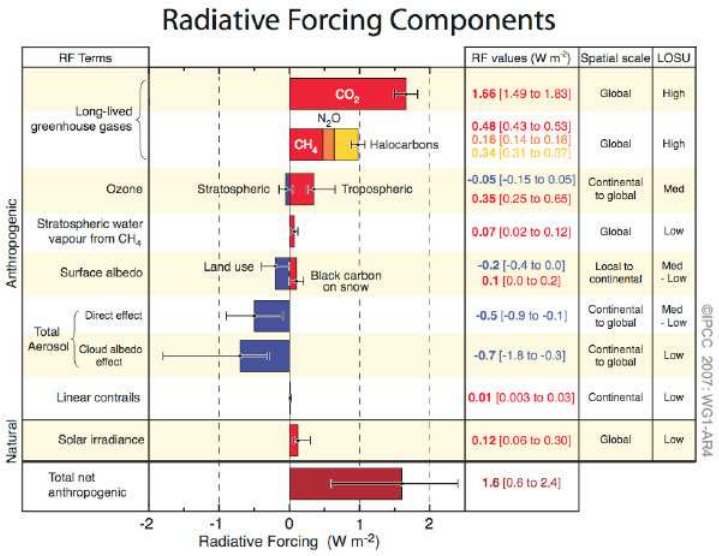

Figure 2.1: Radiative forcing (RF) since 1750 expressing Earth radiation budget changing factors. A negative RF implies cooling. (Forster et al., 2007).

are:

- Indirect climate changes via changes in the solar UV radiation. Several authors examine changes in the ultra violet radiation from the Sun and its affect on stratospheric ozone production and in turn stratospheric temperature, wind and circulation pattern that may propagate down to Earth surface (Haigh, 1994; Labitzke, 1987, 2005; Meehl et al., 1976). A good summary of the effect of UV on climate are found in Haigh (2007). A curious but less documented hypothesis deals with the heating of the sea surface by the direct UV radiation which in turn cause an increase of the dimethyl sulphide flux to the atmosphere which affect cloud creation and hence climate (Larsen, 2005).
- Indirect climate changes via changes in aerosols and cloud cover caused by cosmic rays.

This thesis deals with the latter of the two indirect effects listed.

2.2 Cosmic Rays, Clouds and Climate

Galactic Cosmic Rays (GCR) mainly consist of protons and alpha particles that are accelerated to high energies by supernovas in our Milky Way. Once the cosmic rays reach our solar system they are met by the heliosphere - that extends to where the pressure between the solar wind and the interstellar gas is in balance. Since the solar wind carries the solar magnetic field the heliosphere acts as a shield for the electrically charged high energy particles allowing only the most energetic particles to penetrate through to the Earth.

On arrival at the top of the Earth's atmosphere the protons and alpha particles initiate collision processes that generate a cosmic ray shower of secondary particles. The shower consists of a multitude of elementary particles. Among these are ionizing muons and electrons which are the main source of ionization in the troposphere (Ney, 1959). The geomagnetic field also offers a latitudinal protection with least radiation protection near the poles (Smart and Shea, 2005). As will be described, in section 3.1 these cosmic ray showers can be monitored directly at Earth via various ground based detectors or indirectly via measurements

of radioactive isotopes stored in ice core records (Muscheler et al., 2007). Figure 2.2 shows the 11 year solar modulated periodicity of ionization as well as the altitudinal differences in the ionization rate in the atmosphere during solar maximum and minimum.

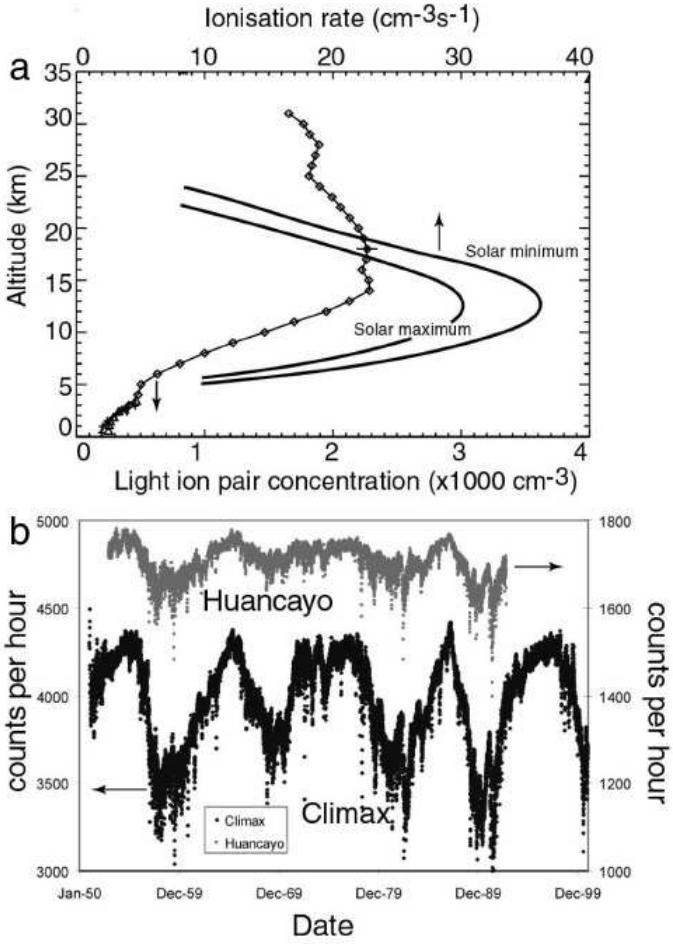

Figure 2.2: Variation of ionization rate (for solar maximum and solar minimum) and typical ion concentration variations with height. (b) Surface measurements of neutrons at two different locations (Climax and Huancayo). From (Harrison and Carslaw, 2003)

Ney (1959) was the first to point to a link between cosmic rays and stratospheric and tropospheric changes. Since then solar activity and climate has been the subject of study and debate. This debate has intensified ever since global temperature increase became part of the public debate as some of the work published in this period indicate that solar activity may have influenced tropospheric climate over timescales ranging from hours to millions of years [4]. On timescales of hundreds of millions of years, related to stellar movement of the Sun through our galaxy, Shaviv and Veizer (2003) have pointed towards a correlation between Earth's climate and cosmic rays. On time scales of thousands of years Bond et al. (2001) have pointed out that correlations between sea-ice rafted debris in the North Atlantic and cosmic ray proxies seem to dominate in the Holocene. On the same time scale Neff et al. (2001) observed strong correlations between Monsoon/global precipitation pattern and solar proxies. On centennial time scales Reid (1987); Shaviv (2008) have reported on correlations between sea surface temperatures and sunspot number.

[4] see also previous section for the link between solar activity and UV

In Svensmark and Friis-Christensen (1997) a correlation between total cloud cover and cosmic rays over a period coinciding with solar cycle 22 was reported. This indicated that a potential physical mechanism between solar activity and climate was linked to cloud formation. Follow up articles confined this correlations to low clouds (Svensmark, 2000; Marsh and Svensmark, 2000b,a), see Figure 2.3. Since clouds are important for the total radiation budget of the Earth (see next section) it was a potential important mechanism that was reported. In the papers it was argued that the increase in solar irradiance since the Maunder minimum (eg. (McCracken and Beer, 2007)) may indirectly via the increase in solar activity, decrease in cosmic rays and decrease in clouds have been responsible for parts of the temperature increase over this period. It was estimated that cosmic rays induced a radiative forcing as large as $1 - 1.5W/m^2$ over the last 250 years (see Figure 2.1) and therefore these papers caused a great amount of debate. Additional reports on correlations between cloud cover changes and GCR (Pallé and Butler, 2001; Marsh and Svensmark, 2003; Todd and Kniveton, 2001; Pallé, 2005; Usoskin and Kovaltsov, 2008; Harrison and Stephenson, 2006) have established examinations of cosmic rays and clouds as a controversial field in climate change science.

However, the reported correlations can do no more than pointing towards an underlying

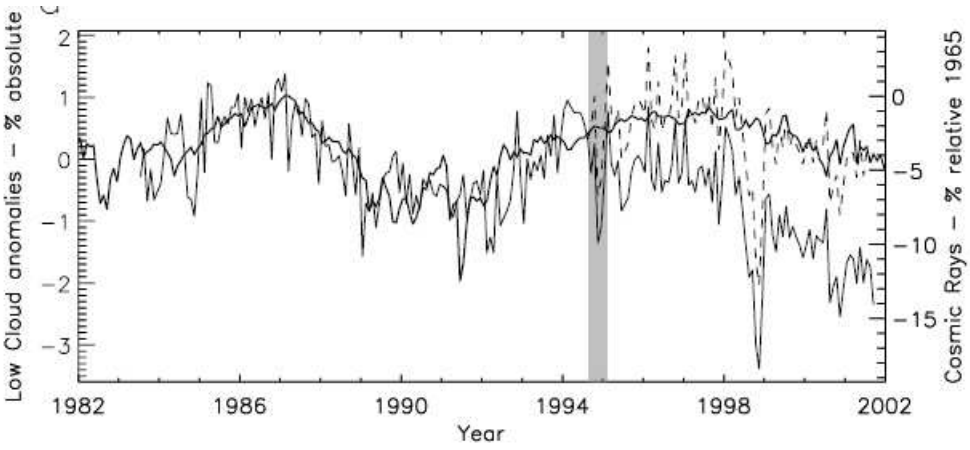

Figure 2.3: Low coud cover and cosmic rays from 1982 to 2002. (Marsh and Svensmark, 2003).

physical mechanism. For instance low-level clouds correlate equally well with variations in other solar parameters, i.e., TSI and the UV component (Christiansen et al., 2007). Furthermore, many papers have criticized the proposed causality link eg. (Kernthaler et al., 1999; Kristjánsson et al., 2002; Kazil et al., 2006; Sloan and Wolfendale, 2008; Kristjánsson et al., 2008; Pierce and Adams, 2007, 2009). [5] leading to confusion of the validity of the observed correlations. Since cloud formation remains the largest source of uncertainty for global climate projections (Forster et al., 2007) it is therefore of vital interest to examine whether such a chain of reaction do exist and to determine its magnitude and nature.

A physical mechanism where ions play a role in stabilizing the formation of aerosol clusters that may grow to modify cloud cover was first proposed in Dickinson (1975) and again proposed in Svensmark and Friis-Christensen (1997). This mechanism states that variations in galactic cosmic ray caused by solar magnetic field variations lead to ionization changes in the troposphere that are hypothesized to affect aerosol formation. Since aerosols make up

[5] Good summaries of the effect of GCR on climate are found in (Carslaw et al., 2002; Gray et al., 2005; Kirkby, 2007; Svensmark, 2007)

the core of each cloud droplet (see next section) the ion mechanism is a candidate to explain the correlations observed between solar activity and climate.

To summarize the working hypothesis of the thesis is:

1. Cosmic rays are modulated by the solar- and geomagnetic field (fact)
2. Cosmic rays are the main source of ionization in the lower atmosphere (fact)
3. Ionization may be important in aerosol nucleation processes in the atmosphere (contentious)
4. Aerosols are important for the creation of clouds (fact)

This chain of reactions will be referred to as the GCR-Ion-Aerosol-Cloud link or in short GCR-Aerosol-Cloud link. All details of this link will be explained in the following clarifying how cosmic ray modulated ions may affect aerosol formation. First, a brief introduction to how aerosols and clouds affect the climate is given.

2.3 Aerosols, Clouds and Climate

Clouds exert a strong net cooling of climate of approximately 13 W/m^2(Ramanathan et al., 1989). The overall cooling comes from the reflection of the incoming solar radiation in lower lying stratocumuli clouds ($\sim -44W/m^2$) balanced by a greenhouse warming ($\sim 33W/m^2$) from trapping of heat in the higher lying cirrus clouds. As illustrated by Figure 2.4 the net forcing after a fractional change in cloud cover of 0.1 is at places as high as 4 W/m^2. This indicates that the global radiation budget and climate is very sensitive to changes in cloud cover.

Atmospheric aerosols are mixtures of solid or liquid particles suspended in the air. They

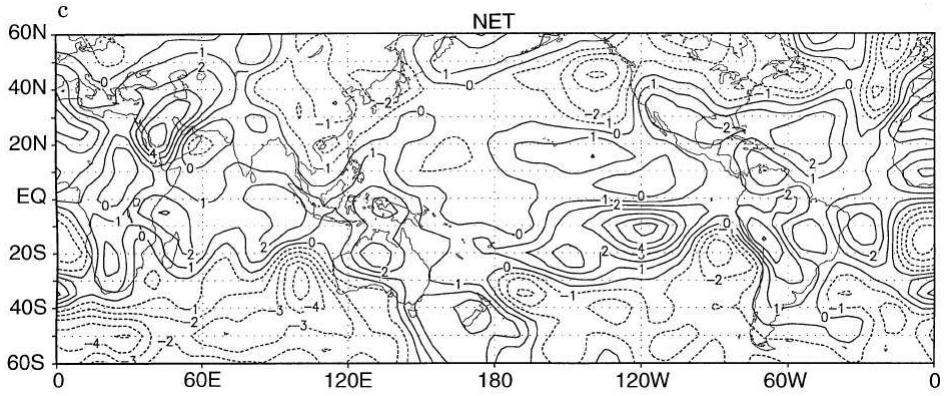

Figure 2.4: Net Radiation Balance Sensitivity (W/m^2) to a change in fractional cloud cover of 0.1(Ringer and Shine, 1997).

affect climate by what is called the aerosol direct effect and indirect effect.

The Aerosol direct effect is the radiation imbalance caused by reflection of incoming short wave radiation by aerosols. The aerosols can either be natural: such as dimethyl-sulfide, dust, minerals and sea salt or anthropogenic: such as sulfur dioxide, nitrates and black carbon. Current estimates based on satellite data and models of the forcing from the anthropogenic aerosol direct effect is $-0.5[\pm 0.4]W/m^2$ caused mainly by the increase in sulfur

dioxide emissions from fossil fuels (Forster et al., 2007). However, in clear skies the forcing is much higher with model averages of $-5.4W/m^2[\pm 0.9]$ from the combined effect of natural and anthropogenic sources (Forster et al., 2007).

When water vapour in the air is supersaturated (relative humidity above 100%), aerosols over approx. 30 nm (Arnold, 2006) may become activated and form cloud droplets by spontaneous growth. The particles experiencing activation are called Cloud Condensation Nuclei which form the building blocks of clouds. In this way aerosols in a super saturated environment may grow to affect cloud formation.

(Ferek et al., 2000) reported that an increase in aerosol concentrations due to ship exhaust can lead to drizzle suppression affecting cloud cover lifetimes. This effect was also examined using MODIS satellite data in (Rosenfeld et al., 2006) where it was demonstrated that under the right conditions a local increase in CCN could force a transitions between a non-cloudy state to a cloudy state. These papers demonstrate the Aerosol Indirect Effect (AIE or the first indirect or Twomey effect) where an increase in the amount of aerosol particles assuming a constant liquid water content will increase the effective surface reflecting area (S., 1974; Forster et al., 2007; Lohmann and Feichter, 2005). The second indirect effect is the extension of the cloud lifetime due to less precipitation assuming a varying cloud liquid water content. The Twomey and cloud lifetime effect and various other aerosol cloud effects are shown in Figure 2.5.

Recent estimates of the forcing of the aerosol indirect effect based on both models and

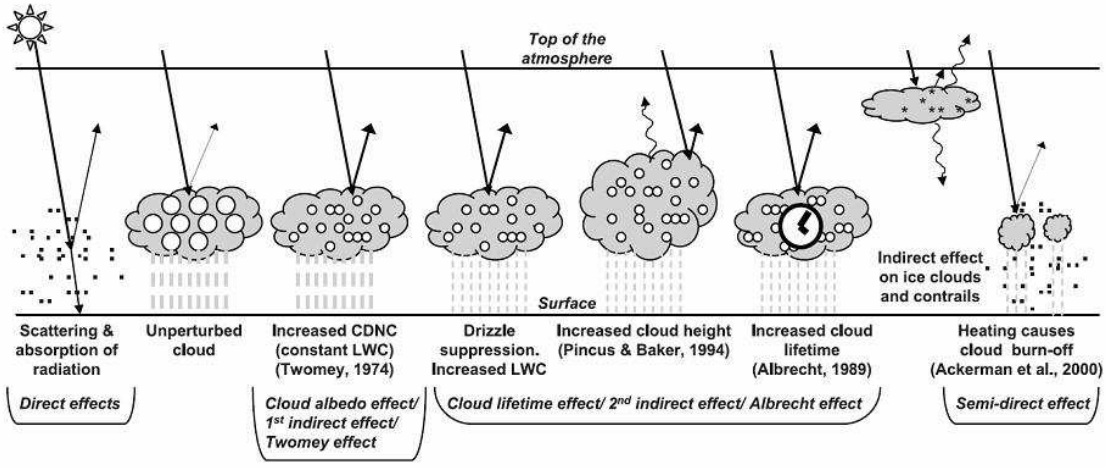

Figure 2.5: Various effects of aerosol influence on cloud cover. Forster et al. (2007).

measurements lead to values as high as 0.4 W/m^2 and as low as -1.5 W/m^2 (Forster et al., 2007). To narrow down this large uncertainty remains one of the most important challenges of climate science. A natural step is therefore to understand all the processes that create and modulate aerosol cluster formation. One of the aerosol formation processes is Ion Induced Nucleation (IIN) involving the ions created by cosmic rays.

2.4 Ion Induced Nucleation

The interaction of tropospheric ions with atmospheric molecules and the conversion to cluster ions was mentioned by Hoppel (1985). The ions were speculated to play a role in stabilizing an initial cluster until the cluster became large enough to grow via neutral

growth mechanisms into a particle or cloud condensation nuclei (CCN). If this mechanism also has an impact on the number of aerosols acting as cloud condensation nuclei (CCN) at typical atmospheric super saturations of a few percent (Arnold, 2006) it will have an impact on cloud creation. The process that describes the role ions play in aerosol growth and nucleation is called Ion Induced Nucleation (IIN).

2.4.1 Observations of Ion Induced Nucleation (IIN)

A combination of a series of laboratory measurements, observations and modeling over the last couple of decades have broadened the picture of how aerosol nucleation occurs. It has become clear that in order to describe atmospheric aerosol nucleation, the theory of homogeneous nucleation, where self-nucleation of single or more species forms clusters above the critical sizes, must be extended to also include ion mechanisms and ternary nucleation (involving third part components) (Seinfeld, 2006). This has been demonstrated in a number measurements of atmospheric nucleation where the established theory of homogeneous nucleation failed to describe the observed data (Hoppel et al., 1994; Clarke et al., 1998; Birmili et al., 2003).

Several other studies have examined the growth of both positive and negative ion families clustered with water and different trace gases in the troposphere in sizes up to 10 nm e.g., (Eichkorn et al., 2002; Laakso et al., 2004; Laakso et al., 2007; Hirsikko et al., 2007; Kulmala et al., 2007). In Lee et al. (2003) growth of aerosols, both neutral and charged, is measured in the upper troposphere/lower stratosphere from 4 nm and up to several 100 nm well above the nucleation size. Here the observations match a simple IIN model. See figure 2.6. This is also the case in Yu and Turco (2000) where the detection and growth of large ion clusters as measured by Weber et al. (1996) was modeled and supported the role of ions in the nucleation process.

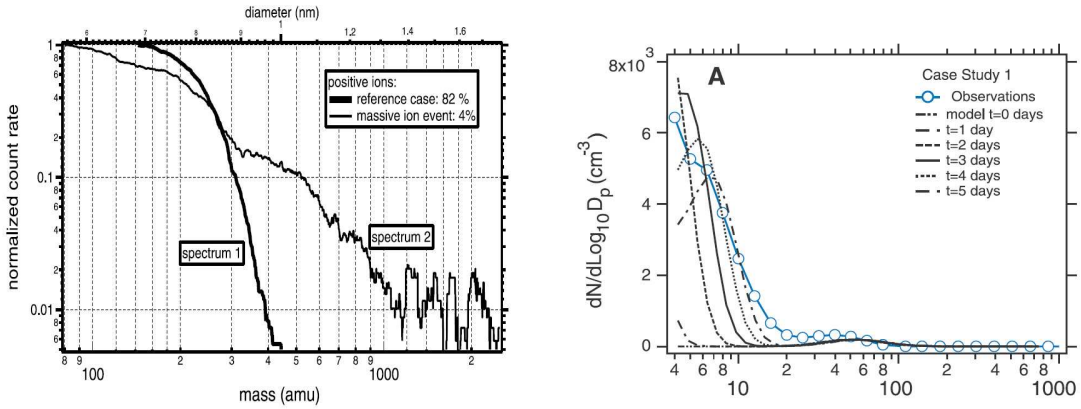

Figure 2.6: left: (Eichkorn et al., 2002) Positive ions (<2nm) are detected in the upper troposphere. An indication of ion-mediated formation and growth of aerosol particles. The black thick curve is representative of the growth of neutral ions in 82% of the cloud free environments. The other black curve is from a measurement of massive ion growth. . right: (Lee et al., 2003) Particle growth in the upper troposphere and lower stratosphere measured from 4 nm and up till several 100 nm well above the nucleation size. The observations match an IIN model of the particle growth.

2.4.2 Theoretical Work on Ion Induced Nucleation

In the 1980's Raes and Janssens (1985) were among the first to formalize the theory of ion induced nucleation based on the classical theory of homogeneous nucleation. This formal-

ism was extended in Turco et al. (1998); Yu and Turco (2001) where condensational growth and coagulation of neutral and charged particles into stable nanoparticles are simulated. A kinetic model is used that solves for interactions among ions, neutral and charged clusters of various sizes, vapor molecules using H_2SO_4 and H_2O vapors. The model is referred to as an Ion Mediated Nucleation (IMN) model and involves ions of either positive or negative charges such that successive addition of compounds (e.g., H_2SO_4) to the ion cluster occurs until it is stable, even when neutralized. This particular model emphasizes that charged particle clusters grow more rapidly than neutral clusters. The reason for this is the thermodynamic advantage in the stability of electrically charged clusters and particle growth rates due to electrostatic forces, See Figure 2.7. Furthermore the model finds that there is a significant growth of particle clusters above the nucleation size in the marine boundary layer where the H_2SO_4 concentration is highest. A follow up-study in (Yu, 2006; Yu, 2009) arrives at the same conclusion with a second generation model using improved thermodynamic data.

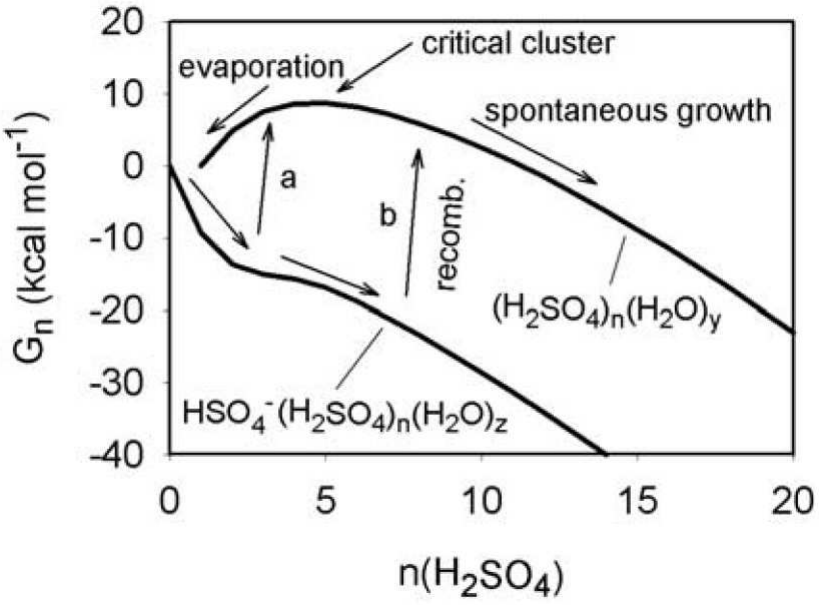

Figure 2.7: The kinematic aerosol model of Lovejoy treats evaporation, growth and recombination of negatively charged and neutral clusters. The Negative ions can recombine b) and continue with spontaneous growth. If the number of H_2SO_4 molecules attached to a neutral cluster is less than the critical number of molecules a) the cluster does not continue growth and evaporates. (Lovejoy et al., 2004)

Yu's results are mainly due to the inclusion of other thermodynamical rate constants in contrast with the studies by Lovejoy et al. (2004) and Eisele et al. (2006). In Yu's paper Ion Assisted Nucleation (IAN)is investigated which besides the conventional growth mechanisms such as condensation and coagulation includes ion-ion recombination where two ions of opposite sign (e.g., HSO_4-ve to NH_4+ve) produce a small stable neutral cluster. A kinetic model is used that is able to model particle growth up to CCN sizes, See Figure 2.7. They find that IIN over land (which contains IAN) is negligible in the lower troposphere and that only small sulphuric acid clusters containing up to 2 H_2SO_4 molecules are created via ion-assisted nucleation and that these clusters do not continue in growth. [6]

[6]See "http://www.cosis.net/members/journals/df/article.php?a_id=3605" for a thorough discussion on the differences in the thermodynamic models of Yu and Lovejoy.

2.4.3 Laboratory work on aerosol formation

Raes et al. (1985) were among the first to make laboratory studies of the role of ions in aerosol nucleation. Using a mixture of SO_2, H_2O and NO_2 the group investigated the role of UV and gamma rays in producing aerosols. Both UV, and gamma rays were found to increase the aerosol production. However, the mixture does not resemble any atmospheric clean condition since the SO_2 values of about 500 ppb are unrealistically high (500 times the atmospheric content of 10-200 ppt (Seinfeld, 2006)). This makes interpretation of these measurements with regard to climatic effects difficult.

In Kim et al. (1997) again a mixture of SO_2, H_2O and NO_2 combined with a radioactive source is used to produce aerosol particles. Kim et al used a voltage collector to separate charges enabling detection of charged ion cluster fractions. For low SO_2 values they find evidence of IIN nucleation since most clusters are charged. Kim et al find that an increase in SO_2 leads to an increase in sulfuric acid concentration. For a certain SO_2 threshold the fraction of charged particles drops and homogeneous nucleation to dominate. This is in accordance with the formalism described in Raes and Janssens (1985). Their experiments seemed to indicate that negative ions were most important for the nucleation. In this experiment again the SO_2 values of about 100-1000 ppb are unrealistically high as compared to the atmosphere.

Berndt et al. (2005) studies the formation of H_2SO_4/H_2O particles with and without organics under near-atmospheric conditions using an atmospheric pressure flow tube where H_2SO_4 is produced via the reaction of OH radicals with SO_2 in water vapour. Berndt argues that the measured fractions of positively and negatively charged particles indicate that IIN did not take place in this laboratory study. Furthermore, they measure both organic compounds and ammonia and concludes that organics did not play a role in the growth and that ternary nucleation (involving ammonia) did not play a role for the generation of new particles. The fact that Berndt et al. did not see any evidence of IMN or IAN does however not rule out the possibility that ions could have played a different role in the creation of particles (<2 nm) since only particles above 2 nm were measured. The growth of ion induced particles could have occurred at smaller sizes.

Berndt's postulation that IIN nucleation does not take place is not in agreement with recent experiments and kinematic models at DTU Space (Svensmark et al., 2007) and **Paper II**. At DTU Space a 7 m^3 reaction chamber at standard pressure and temperature and with variable UV light, ionization level (via radioactive sources) and atmospheric content of SO_2 (80-230 ppt), O_3 (25 ppb) and water vapour is used to model particle growth at lower troposheric conditions. Results from the chamber indicates that stable clusters are formed from SO_2, O_3, and H_2O in the presence of ions and the experiments and simulations suggest that an initial distribution of sub 3 nm stable clusters is formed containing H_2SO_4, see Figure 2.8. It is found that the particle growth rate is proportional to the negative ion density indicating that negative ions are continuously generating stable clusters and that ions are important for the creation of particles in conditions similar to that of the lower troposphere.

In **Paper IV** an international group of scientists performed a CERN pilot experiment on the role of ions in sulfuric acid vapour aerosol nucleation to pave way for the bigger CLOUD experiment (http://cloud.web.cern.ch/cloud/). 44 aerosol bursts were produced in a 8 m^3 reaction chamber containing atmospheric levels of ozone, SO_2 and water vapour and using variable ion intensities produced by the CERN beamline. Of the 44 nucleation bursts produced during the runs only a few indicated that the aerosol formation was ion dependent.

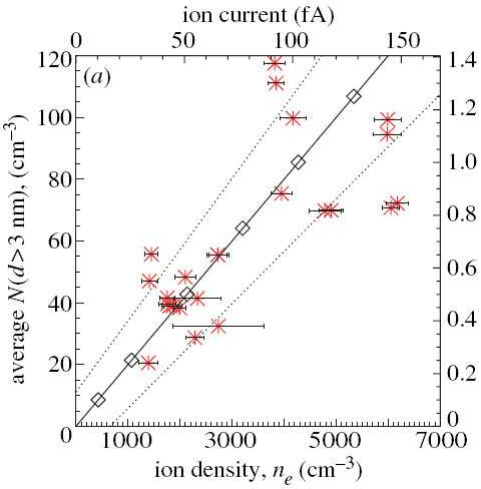

Figure 2.8: Results from the DTU Space reaction chamber show that the ion density is proportional to the creation of new particles (>3nm) under atmospheric conditions similar to the lower troposphere. (Svensmark et al., 2007)

No clear conclusions came out of the pilot run and it shall hence be interesting to follow the development of CLOUD to see what future studies will give.

2.4.4 Other Ion Mechanisms in the Atmosphere

Since cosmic rays through ionization modulate the current flow in the atmosphere, the global atmospheric electric circuit is also believed to be affected by cosmic rays (Rycroft et al., 2000). In numerous papers Tinsley examines this effect, e.g. (Tinsley, 2000). He studies how the vertical currents of the global electric circuit may generate highly-charged droplets at cloud boundaries in the troposphere. After evaporation of these droplets, highly charged CCNs remain which may increase collision efficiency of similar liquid droplets. This process is referred to as electroscavaging and is thought to stabilize the formation of ice particles in supercooled liquid water clouds and postulated to have an effect on climate similar to that of the GCR-Aerosol-Cloud link (Tinsley, 2000) (see also (Carslaw et al., 2002)).

Finally, it is also speculated that Charge Assisted Growth might take place in certain clusters (Eisele et al., 2006). Here it is claimed that positive and negative ions attach to pre-existing neutrally stable clusters, which may increase the reaction rates with other molecules and lead to more CCN. Since the density of ions to neutral particles in the tropospheric atmosphere is very low this process is secondary and less important than other IIN methods.

2.5 Forbush Decreases

As described above several recent observations and models seem to indicate that IIN does take place in the troposphere and that these mechanisms are able to play a role in the generation of cloud condensation nuclei. Yu's studies suggest that it is the particles in the lower troposphere and marine boundary layer (below 5 km) which are most sensitive to changes in ionization. According to these schemes an increase in GCR would lead to an increase in the number of aerosols and CCN on the time scales of hours to days.

One way to examine this hypothesis is to explore features related to Forbush decreases

(FDs) (Forbush, 1937b,a)[7]. Forbush decreases occur when the density of the background GCR vary due to disturbances in the solar wind caused by a Coronal Mass Ejection (CME) or occasionally by solar flares (Hilary, 2000). The variation in GCR is due to an enhanced heliospheric shielding by the magnetic field transported with CME/flare and results in a step decrease over a couple of hours in the concentration of cosmic rays arriving at Earth, followed by a gradual recovery over days to weeks. FDs are therefore short time modulations on top of the solar cycle induced ionization and the title of the thesis refers to these short time scales as compared with the solar cycle length.

Typically, FDs are recorded by Neutron monitors (see section 3.1) that measure the secondary neutrons from the cosmic ray showers on ground. Data from these detectors are used as proxies for the relative variations in ionization near Earth's surface over the solar cycles and during FDs. An example of FD event recorded at Halloween 2003 is shown in Figure 2.9, where a sharp decline in counts is observed with a gradual recovery over the next days.

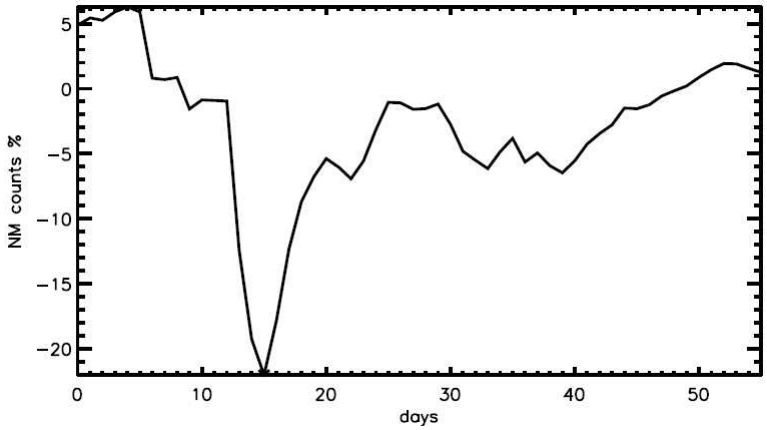

Figure 2.9: Neutron Monitor counts from a Forbush decrease event at Halloween 2003.

There are mainly three reasons why an analysis of Forbush decreases effects in clouds and aerosols is interesting.

1. FDs have a distinct geometry that is easy to recognize in neutron monitors

2. FDs take place on the same time scales as aerosol formation which offers a possibility to test the GCR-Ion-Aerosol-Cloud link in real time.

3. A FD signal in clouds or aerosols would be a clear signature of a GCR-Aerosol-Cloud link. The reason for this is that FD modulate the atmospheric ionization with a distinct decreasing signature over days. FDs only modulate to a minor extent and with an increasing signature the TSI or UV component of the incoming solar radiation (Troshichev and Gabis, 1998). Since any reported climate changing mechanisms involving UV and TSI are supposed to take place on much longer timescales related to either warming of the sea surface (e.g. Reid (1987)) or temperature propagations down the atmosphere (e.g. Haigh (2007)) a significant decreasing signal in the clouds or aerosols during a FD would come from the cosmic rays.

[7]Forbush decreases are named after American physicist Scott E. Forbush 1904-1984 who was one of the pioneers in the field of cosmic rays.

FDs therefore provide a natural experiment to test the proposed GCR-Ion-Aerosol-Cloud link. But as many researchers have discovered analyzing FD effects on climate is difficult. The next section will focus on previous works examining FD effects on climate.

2.5.1 Forbush decrease effect on climate

Forbush decreases have a distinct geometrical shape in the Neutron monitors and in many papers it has therefore been speculated whether this shape could be identified in climate parameters. So far ambiguous conclusions have been reached.

Pudovkin and Veretenenko (1995) were among the first to investigate FD effects on climate. They looked at 65 Forbush decreases from 1969 to 1986 and found significant response in cloud cover over Russia in a latitudinal band from 60-64°. They found that it was mainly cirrus clouds (high level) that correlated well with the FDs. This argument backs up Tinsley's work on Earth- air currents and electro-freezing for high level clouds (see section 2.4.4. Whether this regional response translates into a global significant result and can be reproduced has been the main critique points of this work.

Another regional case, Todd and Kniveton (2001), looked at the decrease of cloud cover after FDs in 1983 to 2000 ISCCP D1 data. Epoch superposition analysis was used to average the effect of noise out (see section 4.6). A small high significance decrease in high cloud cover after FDs was found. The signal was by far largest for high latitudes indicating an effect of the geomagnetic field or a problem with the cloud data. This work was continued in Todd and Kniveton (2004) arriving at similar conclusion but acknowledging the problem of determining cloud cover over high latitude regions mainly covered by ice. The studies support the mechanism investigated by Tinsley.

In Kniveton (2004) the author observes significant correlations in ISCCP D1 cloud data with cosmic rays especially when the effect of rainfall is removed to easier see any externally (solar driven) forced signal. Here it was shown that cloud cover from regions with thick clouds is significantly reduced after and during a FD but is increased for thinner clouds over ocean.

Harrison and Stephenson (2006) used over 50 years of ground level observations from UK station of the diffuse fraction of light to examine whether days with more or less cosmic rays were more or less bright. The diffuse fraction was thereby used as a proxy for cloud cover. Here a slight significant result was found indicating that days with high cosmic ray flux increased aerosol formation in the atmosphere and thereby the diffuse fraction. Again, it is unclear if this regional result could translate into a global signal. Since the diffuse fraction would also represent liquid water clouds this points more to a GCR-Aerosol-Cloud link.

Recently, Kristjánsson et al. (2008) examined MODIS cloud effective radius, cloud optical depth, cloud fraction and liquid water content from 22 FD events over Southern Hemisphere ocean regions. The idea of the study was to test the GCR-Aerosol-Cloud link by looking at pristine marine region supposedly more prone to changes in clouds caused by cosmic rays. The novelty of this paper lies in the study of other geophysical parameters than cloud fraction. Negative results with regard to the GCR-Aerosol-Cloud link were obtained for most FDs except for the six strongest which were shown to give significant responses. To allow for the clouds to respond to the cosmic rays a time lag of a few days were also analyzed but tended to weaken the correlations and no clear effects of time lag were seen. Superposition of FDs and corresponding correlation coefficients between the

geophysical parameters and all the study areas were presented. Many of the approaches taken in analyzing FDs in this study is not far from what this thesis will present. As later will be shown, it is however important to rank the FD according to ionization strength, and not just Neutron Monitor strength as done in this study. Furthermore, now that MODIS daily data is globally available, a global study followed by regional case studies seem to be a more natural starting point, rather than singling out a regional case only. The reason for this is that local weather phenomena makes regional studies difficult.

Sloan and Wolfendale (2008) looked at FDs using monthly global data from ISCCP in several events and at 4 events with daily data. They found no significant response in the monthly data and in four FD events with daily resolution. Since FDs occur on hour/day time scale, it is questionable if analyzing FD with monthly data is sensible using only 4 FD with daily data is probably too few events. This will be clear throughout the thesis.

2.6 Scientific Objective and Method

There is still uncertainty in the climate community on how ions affect aerosol formation and whether these nuclei are capable of significantly influencing cloud microphysics and optical properties on time scales related to aerosol growth. Since aerosol growth do occur on timescales of hours to days the short time ionization variation during Forbush decreases seem to be the natural mechanism to probe these questions since a similar clear decrease is not observed in UV or TSI. But as the previous section showed ambiguous results are obtained. There have been many reasons for the difficulty in analyzing FD effects on climate:

1. FDs are all distinct and only a few have the archetypical triangle shape in neutron monitors. Most FDs have different decreases that vary in length, shape and strength. Furthermore, the signal may be on a downward or upward trend when the FD occurs. Therefore, all kinds of decreases in the NM can be expected and it is difficult to make complete lists of FDs based on a common criteria.

2. To test the GCR-Aerosol-Cloud link, the list of FDs used in the literature (see previous section), have been compiled using the strength of the FD minimum in a NM as the strength of the FD induced ionization. As this thesis shows, this is not the correct approach.

3. FDs occur on timescales of hours/days and may occur simultaneously with global weather phenomena including storms, volcano eruptions and El Nino-Southern Oscillation etc. These weather phenomena may influence cloud cover and aerosol distributions which can make the analysis of the climate effects of FDs difficult.

4. Only relative few major FDs exist and therefore many events may be too small to have an effect above the background climatic noise. This limits the statistics.

5. If the GCR-Aerosol-Cloud causal link is erroneous no climate effect may be seen at all.

This may be some of the reasons why the literature reaches diverging conclusions and new ways of analyzing the FD events are needed. The following approach is taken in this thesis to overcome these difficulties:

- **Chapter 3** A theoretical investigation of the largest 26 FDs based on neutron monitor and muon telescope data establishes a list of the expected ionization change in the troposphere during the FDs as compared with the ionization changes over the solar

cycle. This deals with problem 1 by identifying the size of the effect and when to expect a signal if the GCR-cloud correlations previously observed over the solar cycle are causal.

- **Chapter 4** A data investigation using globally averaged aerosol and cloud observations and the above mentioned reference list of FDs deals with problem 2 and 3. By carefully analyzing the statistical behaviour of FDs as a function of their ionizing strength it becomes clear when a signal is expected to have an influence on aerosol formation.

- **Chapter 5** A theoretical investigation on how the optical properties change during a FD using a numerical aerosol growth model link the previous chapters by combining theory, models and observations.

Chapter 3

Variations in Cosmic Ray Induced Ionization during a Forbush Decrase

The focus of this chapter is to describe the relative variations in the cosmic ray induced ionization in the atmosphere during a FD. The main result in this chapter is a derivation of a table of the 26 largest FD events in the period 1987-2007 and their relative decrease in ionization in the troposphere with respect to the solar cycle.

3.1 Cosmic Ray Showers

The solar wind and the Earth's geomagnetic field modulate the flux of cosmic ray particles arriving at the top of Earth's atmosphere(Usoskin et al., 2004). These cosmic ray particles initiate showers of sub-atomic particles that are the main source of ionization in the atmosphere (Ney, 1959) generating maximum ionization at $\sim$ 15km altitude. In the lower troposphere (<6km) the ionization in the atmosphere is mainly generated by relativistic muons with typical energies $\geq$ 0.5GeV. The muons are produced by pion decay where the initial pion is produced in the collision process by a cosmic ray primary particle with protons or helium nuclei in the atmosphere. Ion production within the atmosphere is, apart from the modulation by the solar and geomagnetic magnetic field affected by the following competing reactions (Duldig, 2000);

- The height of the 125 hPa pressure level (approx 15 km) where pions are produced. A warmer stratosphere means a higher 125 hPA pressure level which means longer transit times and more muon decay before measurement . This is the negative temperature effect - warmer atmosphere less muons.
- The atmospheric temperature around the pion production level. A warmer stratosphere near the pion production level means lower density which means longer pion interaction length and less muon decay before reaching the surface. This is the positive temperature effect - warmer atmosphere more muons.
- An increase in the surface pressure during a temperature increase will increase the atmospheric absorption and ionization losses. And vice versa. This is the barometric effect.

Therefore both solar and geo-magnetic shielding as well as the atmosphere determine the ion production rates in the troposphere. Surface based ionization chambers provide good measurements of the muon intensity in the lower part of the troposphere. However, these chambers have not been in continuous operation and only a limited number of stations exist.

More useful are therefore the database of neutron monitor data (see next section) that over a long period of time have measured the secondary neutrons from the cosmic ray showers. The measured neutrons are not directly a source of the ionization in the lower troposphere but provide an indication of the relative variations in ionization near Earth's surface over the solar cycles and during FDs. Furthermore, a number of muon telescopes have been in operation since 1970. These telescopes measure the directional dependence of muon intensities over a wide range of the incoming spectrum and are therefore very relevant for ionization measurements in the lower troposphere. Defined by their altitude and latitude and relative to the strength of the geomagnetic field and the strength of solar modulation, these ground based instruments (NM's and muon telescopes) respond to different energies of the incoming cosmic ray spectrum.

Here it becomes useful to define the median energy as the energy at which half of the incoming spectrum is deposited in the detector. The median energy (see section 3.5.1) is a function of both altitude and latitude and is therefore a unique value for each detector. Later in the chapter (see section 3.8) this quantity will be used to estimate the expected response of FDs on the atmospheric ionization throughout the troposphere. First, the NM data used in the analysis is described.

3.2 Neutron Monitor Data

The Neutron Monitor World Data Center (ftp://cr0.izmiran.rssi.ru/cosray!/) provides hourly barometric corrected neutron monitor counts from over 130 globally distributed stations from 1953 to present days. This database offers an excellent opportunity to study Forbush decreases (FDs) over a long time period.

The most sensitive detector of this network is the detector at the the South Pole (SOPO), which due to its high altitude of 2820 m and location has a combination of low atmospheric mass above the detector (which means that it is more sensitive to lower energies) and little magnetic shielding. This station has data from March 1964-present and a geomagnetic cut-off (see Section 3.4) of 0.09 GeV (based on geomagnetic field conditions during 1965). The least sensitive station is Lae Station which due to its placement close to equator (latitude of -6.73 degrees) and zero altitude has a geomagnetic cut-off of 15.52 GV. The geomagnetic cut-off data are listed in Appendix B table 7.1 and 7.2

3.3 Forbush Decrease Events in Neutron Monitor Data

A typical FD event is characterized by a rapid decrease in counts followed by a slow recovery process to the average count rate, see figure 3.1. The first steep decrease of the triangle shape signal is actually believed to be a result of two decreases where the first is caused by the magnetic fields right behind the propagating front of the CME. The second sharp decrease occurs once the magnetic field regions of the ejecta (main plasma region of the CME) encapsulates the magnetic field of the Earth (Hilary, 2000). Once the CME has passed the Earth the NM signal slowly recovers over a time depending on the tail of the CME.

To find the dates of the Forbush decreases minimum in the NM data four stations with long data availability and high sensitivity to cosmic ray change were selected: South Pole (SOPO), Climax (CLMX), McMurdo (MCMD) and OULU. Each of these NMs have data series of daily barometric corrected data over the whole period of interest (from 1980) and

good track records of stability and reliability.

A Students T-test of two equally sized arrays returns the probability that the two arrays have significantly different means. This test can be used to locate the dates of the FD minimum. For two arrays x and y with means $\bar{x}$ and $\bar{y}$ the T-statistic in the Students T-test is defined as:

$$T = \frac{\bar{x} - \bar{y}}{\sqrt{\frac{\sum_{i=0}^{N-1}(x_i - \bar{x})^2 + \sum_{i=0}^{M-1}(y_i - \bar{y})^2}{(N+M+2)}\left(\frac{1}{N} + \frac{1}{M}\right)}} \tag{3.1}$$

where $x = (x_0, x_1, x_2, ..., x_{N-1})$ and $y = (y_0, y_1, y_2 ..., y_{M-1})$. A t-statistics function of time for each of the Neutron monitor data series is then calculated by displacing two NM array from the same NM data string a width W from each other:

$$T(t) = T(x(t), y(t)) \text{ , for all t} \tag{3.2}$$

where $x(t) = NM_{data}[t, t + W - 1]$ and $y(t) = NM_{data}[t + W, t + 2 * W - 1]$. Each FD minimum now appears as a peak in the students t-statistics function and an event is registered if T(t) exceeds a given threshold. Values of W=5 and T(threshold)=1 were used to locate the FDs.

Figure 3.1 shows an example of such a peak in the T-distribution from a FD event in July 1984. Since we are interested in finding all significant FDs, the threshold is initially put too low which as a result returns too many FD events since random fluctuations will appear as peaks in the T-distribution. However, by comparing events from the 4 stations and making visual inspections a complete list of the dates for the largest FD minima can be constructed.

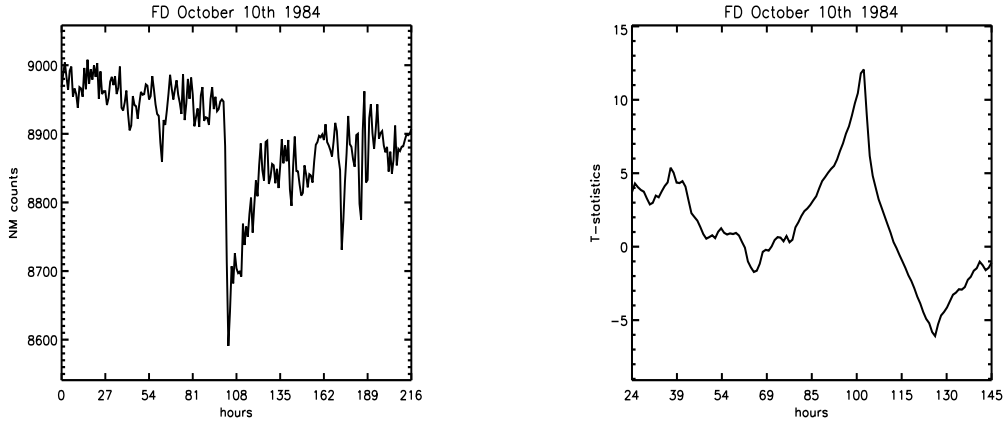

Figure 3.1: Left) Neutron Monitor counts for Forbush decrease event at McMurdo event 10/6/1984 Right) T-statistics from FD event 10/6/1984. A positive peak is observed at the Fd minimum.

The FD minimum in % is now determined by calculating the average NM count in a 14 days window (chosen as the the base level) prior the FD minimum and determining the percentage change of the minimum peak from the average value. Using percentage changes the mean count rate of the Neutron Monitor becomes irrelevant thereby avoiding scaling problems.

The FD minimum dates as well as the FD % response of all stations are listed in table 3.1 for the SOPO station along with standard deviations of the base level as well as the actual count values. We have focused on events that occur later than 1987 enabling an overlap

Order	Date	FD (%)	Stddev base level (%)	FD in count	base level mean count rate
1	31/10/2003	-24.20	6.94	-2224.80	9192.80
2	13/6/1991	-17.98	6.00	-1413.53	7861.53
3	16/7/2000	-15.32	3.35	-1409.87	9202.87
4	15/3/1989	-15.69	2.43	-1509.80	9619.80
5	19/1/2005	-15.21	2.88	-1519.80	9990.80
6	13/9/2005	-14.12	3.36	-556.40	3940.40
7	29/10/1991	-13.19	1.76	-1220.53	9254.53
8	12/4/2001	-12.25	2.60	-1135.27	9265.27
9	27/7/2004	-11.06	2.37	-1127.60	10196.60
10	10/11/2004	-11.70	3.04	-1237.47	10576.47
11	25/3/1991	-11.53	3.56	-1016.40	8812.40
12	9/7/1991	-11.48	4.71	-921.87	8026.87
13	26/9/2001	-9.36	0.81	-901.73	9631.73
14	17/7/2005	-9.72	2.19	-1023.87	10531.87
15	25/9/1998	-9.46	0.98	-1035.73	10947.73
16	2/5/1998	-9.20	0.69	-211.40	4111.40
17	31/5/2003	-9.26	2.39	-867.00	9360.00
18	27/8/1998	-9.02	2.46	-962.53	10675.53
19	10/5/1992	-9.29	0.86	-914.07	9841.07
20	10/9/1992	-8.26	2.93	-862.20	10443.20
21	15/5/2005	-7.91	2.09	-814.93	10308.93
22	29/11/1989	-7.79	2.35	-664.27	8526.27
23	27/2/1992	-7.15	1.26	-673.20	9412.20
24	18/2/1999	-7.45	2.08	-788.40	10577.40
25	28/8/2001	-7.44	1.86	-708.40	9518.40
26	25/11/2001	-7.0	1.51	-655.47	9590.47

Table 3.1: Dates of FD minimum showing larger than 7 percent decline at SOPO in the period 1987-2007. The table shows the FD minimum in percentage from a base level calculated as the mean of the 14 days before the event. All events except one are from the SOPO station (cut-off 0.11GV and altitude 2820m). The 13/9/2005 event is detected from the CLMX station (cut-off 3.03GV and altitude 3400m) since SOPO has no data from that period.

with the availability of ISCCP and SSMI/I data (see next Chapter). Note how after 1988 only 26 FDs of decreases are larger than 7 percent in SOPO. Also note that the standard deviation of the base level is printed to secure that the FD in % is significant compared to the standard deviation of the base level. The major events in table 3.1 all appear in the lists of Kudela and Brenkus (2004); Kristjánsson et al. (2008) but not all minor FDs are the same in the three lists. The reason for this has to do with definition of base levels and where to define the beginning of a FD. As will be clear in section 3.8.2 the major events are the most interesting for the purpose of analyzing FD effects in climate. Table 3.1 is therefore more than adequate.

3.4 Geomagnetic Cut-off Rigidity

The strength of the motion of a charged cosmic ray particles propagating in the geomagnetic field is defined by its rigidity:

$$P = pc/\|q\| \tag{3.3}$$

where c is the speed of light and $p/|q|$ represents the ratio of the particle's momentum to charge. The unit of P, as expressed by the momentum equation above is in GV (Giga Volt) but is often also expressed as a kinetic energy (GeV). Using relativistic mechanics for conversion between energy and momentum the rigidity in GeV is given by:

$$P(GeV) = \sqrt{(M * M_0)^2 + P(GV)^2} - M * M_0 \tag{3.4}$$

where, $M_0 = 931.141$ is the rest mass energy of a proton per atomic mass unit MeV/c^2 and M=1.0081451 is the rest mass of a Proton in MeV/c^2 For example the above equation returns a $P(GeV) = 9.1$ for $P(GV) = 10$, $(GeV) = 14.09$ for $P(GV) = 15$ and $P(GeV) = 19.08$ for $P(GV) = 20$. The rigidities in GeV and GV are thus very close to each other.

Now, it is possible to define the geomagnetic cut-off rigidity, P_c, as the minimum rigidity a particle must have to penetrate the Earth's magnetic field and reach the top of the atmosphere. The cut-off rigidity is not fixed at a single rigidity, but instead is spread over a range of rigidities depending on the angle of incidence. For simplicity this range is approximated by considering only the vertical cut-off rigidities. The geomagnetic vertical cut-off is a function of the geomagnetic latitude Λ and can be estimated as (Usoskin et al., 2004):

$$P_c = 1.9 * M * 1.e^{-22} * \cos\Lambda^4 * (\|\mathbf{r} - \mathbf{r}_{ecc}\|)^{-2}, \tag{3.5}$$

where M is the Earth magnetic dipole moment $[A/m2]$ and $\|\mathbf{r} - \mathbf{r}_{ecc}\|$ the distance in Earth Radii of an eccentric dipole dislocated from the Earth's center. A slightly more detailed version of the geomagnetic cut-off is shown in Figure 3.2 calculated from the IGRF model 2000 eccentric dipole approximation of the geomagnetic field. Here it is observed that at northern latitudes the primary nucleon must have energies $\geq$ 1GeV to generate a muon cascade that reaches the surface. At equator this number is about 15 GeV.

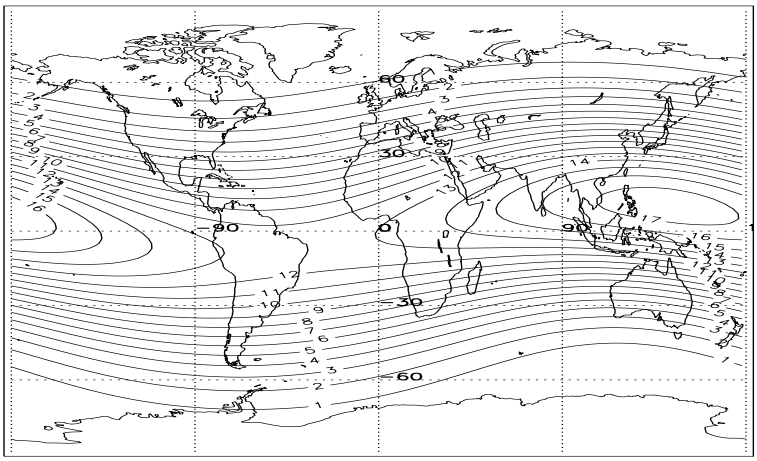

Figure 3.2: Global map of geomagnetic cut-off. P_c in GV. Calculated from the IGRF model 2000 eccentric dipole approximation of the geomagnetic field.

3.5 Response and Yield Function

The primary cosmic ray flux in the top of the atmosphere initiates a shower of sub-atomic particles and ionization that are functions of the primary rigidity/energy of a single cosmic ray particle. The magnitude of a response in a detector measuring one of these cosmic ray governed processes (for instance the ionization or muon flux) is then described by knowledge of two things:

- The flux of particles/ion pairs at altitude h generated by a single cosmic ray particle arriving at the top of the atmosphere with primary rigidity P. This is the yield function $Y(P,h)$.
- Information about the primary cosmic ray spectrum at 1AU, $G(P,\phi_0)$. Here the cosmic ray spectrum is influenced by heliospheric modulation ϕ due to solar activity.

The response actually monitored in the detector at height h is then described as the integral over all rigidities of the convolution of the primary spectrum and the yield function. Since the available energies at a given location is a function of the geomagnetic field the lower limit of the integral is the geomagnetic cut-off of the detector defined by its location. The total detector response is then given by:

$$N(P_c,h,\phi_0) = \int_{P_c}^{\infty} G(P,\phi_0)Y(P,h)dP \tag{3.6}$$

The yield function is naturally also dependent on the atmosphere but in the following a standard atmosphere is assumed[1].

A change in the solar activity expressed by a change in the heliospheric modulation parameter $\phi_0 \rightarrow \phi$ such that $G(P,\phi_0) \rightarrow G(P,\phi)$, gives a response in $N(P_c,h,\phi)$ as:

$$\frac{\delta N(P_c,h,\phi)}{N(P_c,h,\phi_0)} = \frac{\int_{P_c}^{\infty}[G(P,\phi)-G(P,\phi_0)]Y(P,h)dP}{\int_{P_c}^{\infty} G(P,\phi_0)Y(P,h)dP} \tag{3.7}$$

$$= \int_{P_c}^{\infty}\left[\frac{\delta G(P,\phi)}{G(P,\phi_0)}\right] W(P,h,\phi_0)dP \tag{3.8}$$

$$W(P,h,\phi_0) = \frac{G(P,\phi_0)Y(P,h)}{N(P_c,h,\phi_0)} \tag{3.9}$$

here $W(P,h,\phi_0)$ is the response function normalized to the response of a baseline state, $N(P_c,h,\phi_0)$, that could be during solar min or solar max or just before a FD event.

3.5.1 Median Rigidity

The median rigidity can now be introduced. By definition the integral of the normalized response function W sums to 1:

$$\int_{P_c}^{\infty} W(P,h,\phi_0)dP = 1 \tag{3.10}$$

the median rigidity, P_m, is defined as the 50% contribution from the weighted rigidity spectrum:

$$\int_{P_m}^{\infty} W(P,h,\phi_0)dP = \frac{1}{2} \tag{3.11}$$

[1]US Standard Atmosphere 1976 - http://en.wikipedia.org/wiki/U.S._Standard_Atmosphere

P_m therefore expresses the median of the rigidity range of the primary spectrum to which the atmospheric quantity N is sensitive. Two different type of detectors with same P_m will now respond to the same weighted rigidity range of the primary spectrum and hence have same relative responses. This is useful for comparison of responses from different detectors. This in principle means that the relative response of a FD in muon detectors, ion chambers and NMs can be plotted on the same figure. A response in a NM can now be compared with the response in atmospheric ionization in regions where the the two detectors have similar P_m.

3.5.2 Response Function for a Neutron Monitor and Ionization Detector

To be able to estimate the median rigidity, P_m, the response function must be known. For NM's this can be via either parameterization of NM latitudinal survey's, theory, or Monte Carlo simulations of a test particle with energy E triggering a cascade in the atmosphere.

Figure 3.3 shows three different estimates of the response function for a neutron monitor situated at an altitude and a geomagnetic latitude equivalent to that of Climax, i.e., 3200m. The annotated vertical black lines indicate the cut-off rigidity (3GV) and an estimate of median rigidity ($\sim$ 10GV) for the Climax NM (see next section). The grey bar represents the uncertainty in the median rigidity calculation based on the range of different response function estimates and variations over a solar cycle.

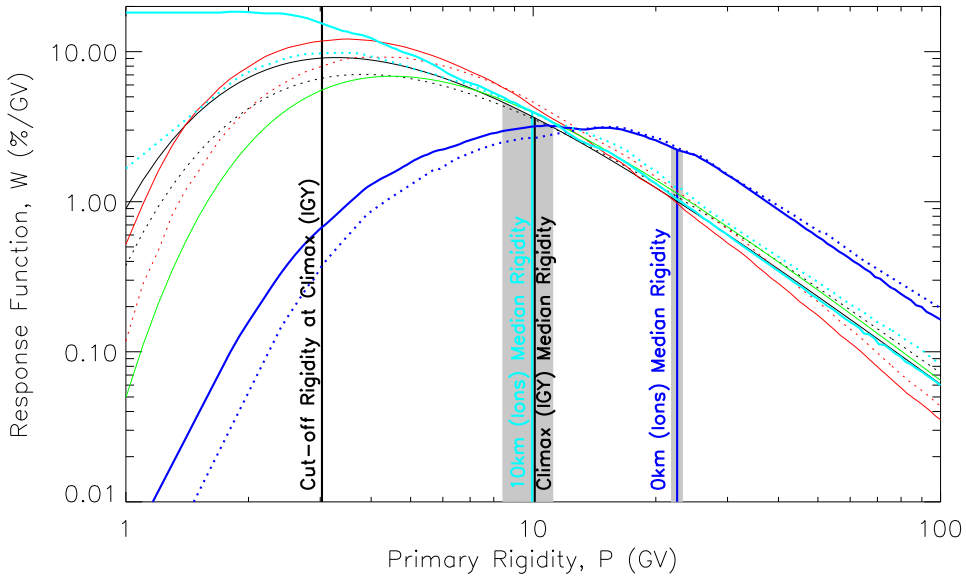

Figure 3.3: Response functions of a NM counter at an altitude of 3200m and those of atmospheric ionization at 0km (blue) and 10km (light blue) during solar min (solid) and solar max (dotted) conditions. Three different estimates for the NM counter are shown based on a combination of parameterizing latitudinal surveys and theory provided by Clem and Dorman (2000)(black), Nagashima, Sakakibara, and Murakami (Nagashima et al.)(red) and Moraal et al. (2000) (green). All curves have been normalized to $N(P_c, h, \phi_0)$, with cut-off rigidity P_c = 3.03GV equivalent to that for the Climax NM. Uncertainties due to variations over a solar cycle are indicated by the grey bars. Courtesy of Nigel Marsh.

Since atmospheric ionization measurements are rare the atmospheric ionization yield function is normally estimated from a Monte Carlo simulation (Usoskin et al., 2004). Here

the response function at 0km and 10km are also shown in figure 3.3. The annotated vertical blue lines give the median rigidity at 0km altitude ($\sim$ 23GV) and 10km ($\sim$ 10GV) for similar geomagnetic location to Climax. Note that at 10km the median rigidity for ionization can be compared to that of the Climax NM. Therefore changes in the NM counts at Climax as expressed by the median rigidity should have the same relative response as changes in the atmospheric ionization at 10km rather than at 0 km.

Figure 3.4 shows how the cut-off rigidity versus median rigidity (in GeV) throughout the troposphere differ between NM and atmospheric ionization. For instance a NM at altitude 2 km with a geomagnetic cut-off of 8 GeV has a median rigidity of approx 20 GeV - a median rigidity found at 4km for the atmospheric ionization for the same geomagnetic cut-off. This indicates, that the relative response for a NM placed at an altitude of 2 km for the geomagnetic location of 8 GeV, would show the same relative response as an ionization detector placed at an altitude of 4 km for the same geomagnetic location.

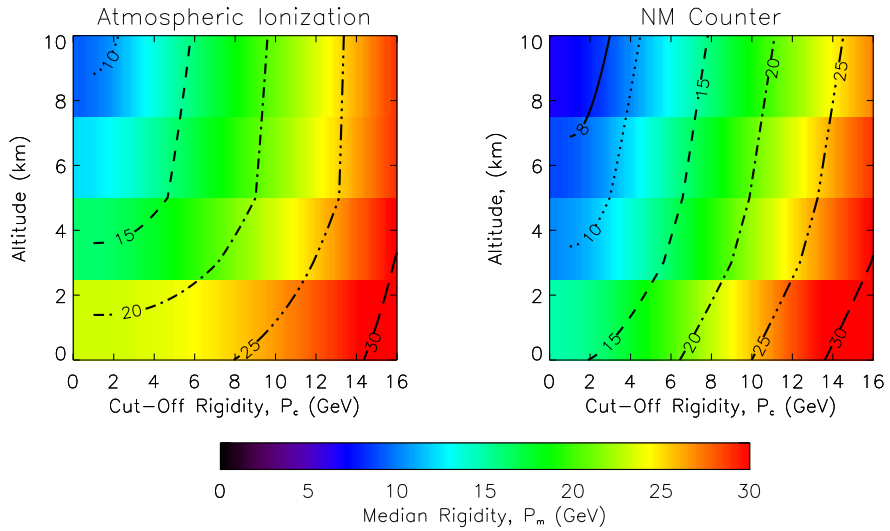

Figure 3.4: Median rigidity, P_m, as a function of cut-off rigidity, P_c, and altitude, under solar max conditions. The left panel is for atmospheric ionization, and the right panel is for a NM counter. The annotated contours and colours represent median rigidity, P_m. Here in GeV. Courtesy of Nigel Marsh.

3.6 Median Rigidities for Muon telescopes and NM data

In order to determine the median rigidity of a detector, information on the response function must be known. We used the response function of (Clem and Dorman, 2000) under solar maximum conditions to determine the NM median rigidities used in this thesis. This gives a median rigidity range of the NM data ranging from $\approx$10 GV (South Pole station) to $\approx$47 GV (Ahmedabad, India) (the rigidity values change during solar max and min). The data are listed in Appendix B table 7.1 and 7.2.

The data from the Multi-Directional Cosmic-Ray Muon Telescope at Nagoya (Altitude 77 m) contains 17 different viewing angles of the Multi-directional Nagoya detectors. This represent 17 different paths of the muons through the atmosphere and therefore 17 different response functions and median rigidities, see 3.2. The median rigidity range of the Muon telescope ranges from 60 to 119 GV which immediately reveals that muon telescopes are more sensitive to the high energy part of the primary spectrum. The median rigidities were

Station	R_c	R_m	Station	R_c	R_m
VERT	11.5	60.0	N49	12.9	83.0
N30	12.9	66.0	S49	10.9	81.0
S30	11.3	64.0	E49	21.0	88.0
E30	16.2	67.0	W49	9.3	80.0
W30	9.4	63.0	N64	11.0	110.0
NE39	17.9	73.0	S64	10.8	104.0
NW39	11.0	68.0	E64	25.1	118.0
SE39	15.0	71.0	W64	8.7	108.0
SW39	9.2	67.0			

Table 3.2: Nagoya muon detector rigidities in GV. Geomagnetic cut off and median rigidities.

kindly provided to us by the Nagoya University [2].

3.7 Forbush Decrease Response as a Function of Median Rigidity

It is now possible to plot each FD events from table 3.1 using the computed median rigidities and the database of NM data and muon telescope data, see Figure 3.5.

Figure 3.5 shows that the FD response follows a power law for increasing P_m (due to

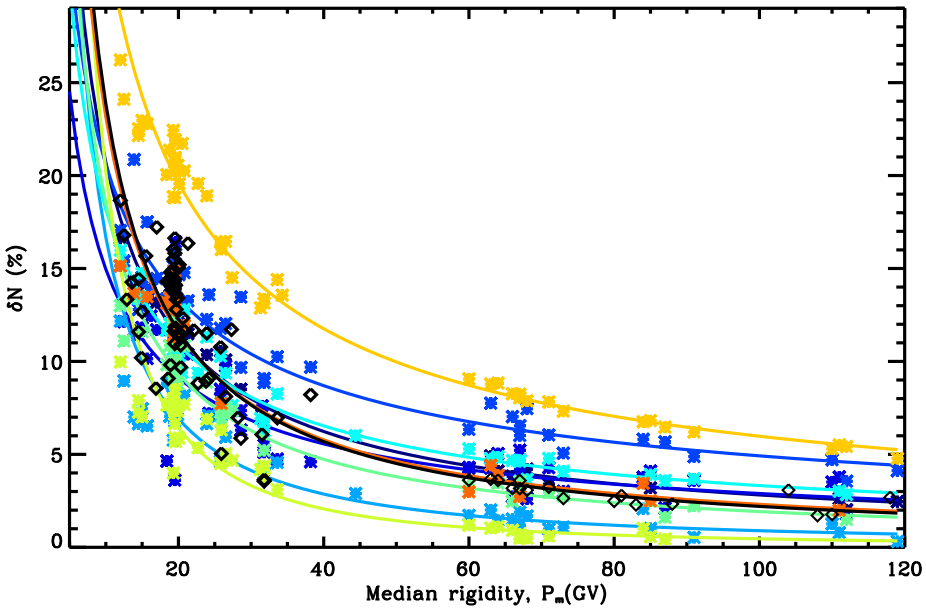

Figure 3.5: FD minimum in % for selected major FDs as a function of the median rigidity of the stations P_m for both neutron monitors and the Nagoya Muon Telescope. Each color represents the major FDs from 3.1 and the solid lines are are the fitted functions of the form of Eq. 3.12. The FD minimum compared to a 10 day base level 15 days prior to the event. The colored curves are the fitted functions of the form of Eq. 3.12 for the major FD events. The black curve and black points are the fit parameters and points related to the solar cycle as derived in Appendix A. See **Paper I**.

the shielding from the geomagnetic field) with an exponent γ as:

[2]NM data can be obtained from ftp://cr0.izmiran.rssi.ru/ and we acknowledge the Cosmic Ray Section, Solar-Terrestrial Environment Laboratory, Nagoya University who provided the muon data and information on muon median rigidities. Data can be obtained from http://www.stelab.nagoya-u.ac.jp/ste-www1/div3/muon/muon1.html

$$\frac{\delta N}{N} = A * P_m^{\gamma}, \tag{3.12}$$

A being the percentage at a fictitious station with $P_m = 0$, and $\frac{\delta N}{N}$ the relative response in the NM. γ is the decay rate of a FD response with median rigidity. By taking the logarithm on each side it becomes a linear equation:

$$\log 10\left(\frac{\delta N}{N}\right) = \log 10(A) + \gamma * \log 10(P_m) \tag{3.13}$$

where $X = \log 10(P_m)$ and $Y = \log 10\left(\frac{\delta N}{N}\right)$. By fitting each FD in table 3.1 to eq. 3.13, the parameters γ, A as well as their respective errors, can be determined. The left panel in Figure 3.6 shows how A, γ for a single FD is derived from the linear fit of the log-log plot.

The dependency of γ on the FD strength is now examined in detail. In Figure 3.6 the SOPO response $R_S = \frac{\delta N}{N}(SOPO)$ for selection of FD events from the whole database[3] are plotted as a function of γ. Here it is shown that the bulk of FDs has very different gamma responses in the range from approx [-0.3,-1.2] (the outlier not shown on the plot is from the very strong FD with $R_S \approx 35\%$ during August 1972 (Rao, 1976)).

This means that each individual FD has a characteristic response characterized by the exponent A, γ. Even though two FD events cause the same response in $\delta N/N$ for a given NM, the ionization response other places in the atmosphere for the two events may be completely different due to different rigidity responses. In section 3.8.2 the A, γ parameters for various FDs are used with the atmospheric ionization yield function to derive how the atmospheric ionization responds to a FD. Here a table of A, γ for the 26 largest FDs is also given, see 3.3.

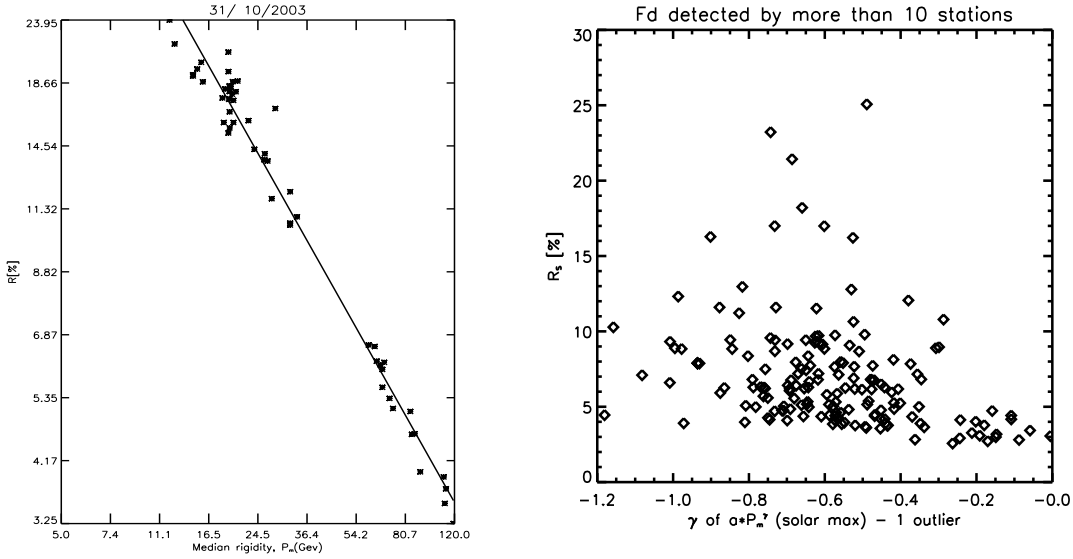

Figure 3.6: Left) FD minimum for the Halloween 2003 event. Used to derive the fit parameters A, γ. Right) The SOPO response in % $R_S = \frac{\delta N}{N_0}(SOPO)$ as a function of the γ factor. FD events detected by more than 10 stations. Solar max values of P_m. The outlier is the August 72 FD event.

[3]The right figure was part of earlier work not restricted to the period where cloud data is available

3.8 Atmospheric Ionization during a Forbush Decrease

Using two different approaches, the change in ionization during a FD in the atmosphere, can now be determined. In this thesis two new methods are introduced:

- **Method 1**: First, an ionization yield function given in (Usoskin et al., 2004) is introduced. This yield function is used to calculate median rigidities for an ionization detector in the whole atmosphere. Then, the ionization response $\frac{\delta N}{N}$ is parameterized according to eq. 3.12 for a FD. Last, a reference NM station is selected, and the ratio between the ionization response and NM response is plotted all over the atmosphere. See section 3.8.1.

- **Method 2**: The response in NM and muon detectors is used to find $A * P_m^{\gamma}$ for all FDs. The results of this is used to determine the primary spectrum modulation during a FD. This is followed by a Monte Carlo Simulation to derive the change in ionization throughout the atmosphere during a FD. Last the ionization changes are compared to the solar cycle ionization changes. This is the method presented in **Paper I**. See section 3.8.2.

An alternative method was introduced by Usoskin et al. (2004) who derived relative primary rigidity spectrum variations $\frac{\delta G}{G_0}$ from observations of N in a neutron monitor from knowledge of a baseline response function W of the neutron monitor. The information on the rigidity spectrum variation was used to reverse the process and calculate the response in the ionization by the use of another yield function. This valid approach was used to analyze solar cycle variations on a monthly scale but has not yet been used to analyze Forbush decreases. Though this method represents an alternative approach it is not pursued any further in this thesis.

3.8.1 Method 1

It is the aim of this section to derive a scaling relationship between atmospheric ionization response and NM response during a FD. First, the median rigidities of an ionization detector in the atmosphere, must be determined.

In Figure 3.4 the altitude and median rigidity P_m was calculated from the ionization yield function (Usoskin et al., 2004) and plotted as a function of geomagnetic cut-off P_c. Since P_c is known for all points at the surface, the median rigidities for an ionization detector, $P_m(I)$, can be determined for all points in the atmosphere.

Using median rigidities are used, it is a good assumption, that the ionization change during a FD can be described by eq. 3.12 as:

$$\frac{\delta N}{N_0}(I) = R(I) = A * P_m(I)^{\gamma}, \tag{3.14}$$

where I represents the ionization. Similarly, the response to a FD in a NM is:

$$\frac{\delta N}{N_0}(NM) = R(NM) = A * P_m(NM)^{\gamma}. \tag{3.15}$$

Now, the SOPO NM is chosen as a reference station such that: $\frac{\delta N}{N_0}(SOPO) = R_S = A * P_m(S)^{\gamma}$, where $P_m(S)$ is the median rigidity for SOPO. By focusing on a single FD event,

with a fixed γ, A, it is now possible to relate a specific FD event in SOPO to the ionization in the atmosphere by a division of eq. 3.14 with 3.15:

$$\frac{R(I)}{R_S} = \left(\frac{P_m(I)}{P_m(S)}\right)^{\gamma} \tag{3.16}$$

Hereby, a scaling relationship between the SOPO response and atmospheric ionization is obtained for all points in the atmosphere.

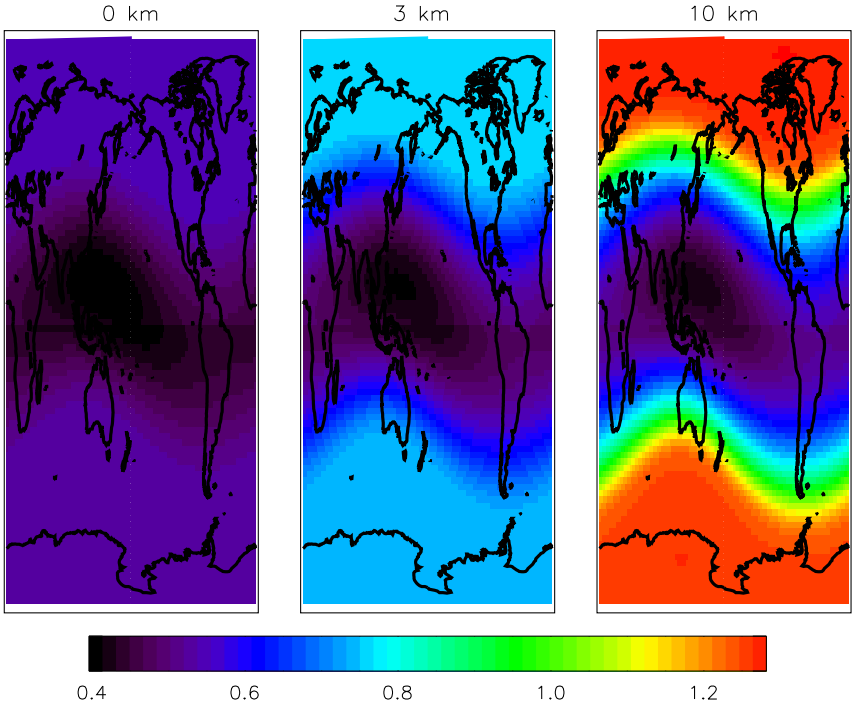

Figure 3.7: Plots of the ratio $\frac{R(I)}{R_S} = (\frac{P_m(I)}{P_m(S)})^{\gamma}$.

In Figure 3.7 the ratio $\frac{R(I)}{R_S} = (\frac{P_m(I)}{P_m(S)})^{\gamma}$ for $\gamma = -0.9$ is plotted for three different altitudes 0, 3 and 10 km. The figure shows that for this particular gamma value at 0 km altitude, the relative ionization response is approximately half of that observed in the SOPO NM (i.e. a 20% FD minimum at SOPO NM would be a 10% decrease in ionization at 0 km). At 10 km altitude the relative ionization response at high latitudes is larger than what is observed at SOPO, although the equatorial regions still have values comparable to that of 0 km altitude. At mid latitudes for 10 km the values are close to 1, meaning that the relative ionization and NM responses are identical. Hence, by determining the γ for each FD (see section 3.7) it is now possible to relate the relative response in ionization at any height and place in the atmosphere to that observed in SOPO (or another reference station).

Method 1 is useful to get a picture of how the relative ionization changes globally at a given altitude for a specific event. The ionization is related to the SOPO NM events and derived from the yield function by Usoskin et al. (2004). Method 2 uses a different approach and relates ionization changes during a FD to the change in ionization over the solar cycle. Here the ionization yield function is determined by a Monte Carlo Simulation using a cosmic ray shower code. Global values of the average ionization decrease at a given altitude with respect to the solar cycle for a given FD are derived. This approach enables comparison with global climatic means for a specific altitude as discussed in the next chapter.

3.8.2 Method 2

This section is a rewrite of the supplementary material of **Paper I** used to derive the relative contributions to atmospheric ionization from a specific FD as compared with the solar cycle induced ionization.

It is the aim of this analysis to use the program CORSIKA (Heck et al., 1998) to determine ionization changes during the atmosphere for different FDs. In order to do this the response in the primary spectrum changes during a FD must be determined. First relation 3.12 is modified to approximate the FD dependency for the rigidity spectrum at 1 AU by:

$$\frac{\delta G}{G} \approx A P^{\gamma}, \tag{3.17}$$

where P_m now is replaced by P.

It must now be estimated how good the approximation in eq. 3.17 is. For a given value of A, γ, dN/N calculated using eq. 3.9 with the yield function from Flückiger et al. (2008) and $\delta G = G A_k P^{\gamma_k}$ should equal dN/N calculated from equation 3.12 with P_m determined from eq. 3.11 and the yield function of Flückiger et al. (2008). By repeating this for different geomagnetic cut-offs and for a value of $\gamma = -0.49$ and $A = 0.8$ Figure 3.8 is obtained. Since the errors of the two ways to determine dN/N are within 10% this shows that eq. 3.17 is a good approximation.

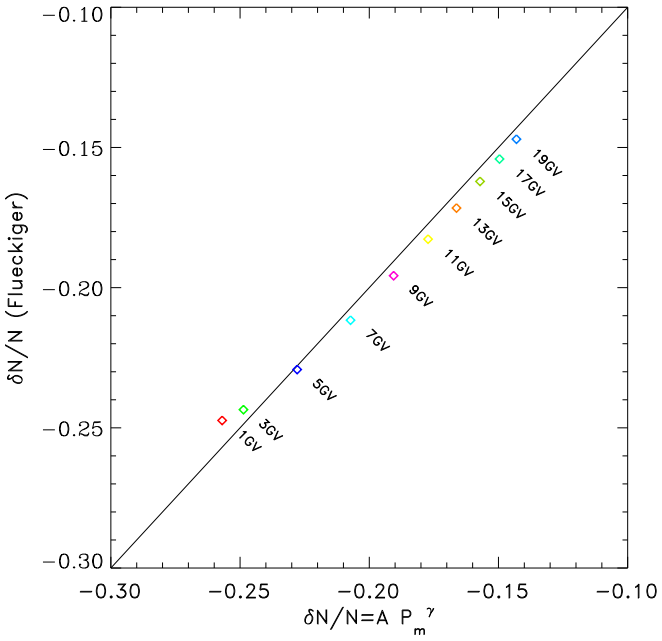

Figure 3.8: Validation of approximation of primary spectrum during FD (eq 3.17 for different cut-offs. $\gamma = -0.49$ and $A = 0.8$. The error is within 10%. See text for details. From **Paper 1**

A Monte Carlo simulation program CORSIKA (Heck et al., 1998) of high energy cosmic ray showers is now used to calculate the ionization throughout the atmosphere (US standard). The primary energy spectrum is from observations close to solar minimum (Sanuki et al., 2000). Primary protons are given an initial energy from 1-1000 GeV, incident angle from $0 \leq \alpha \leq 70$ deg and 10.000 showers are calculated. The output of the program is the deposited ionization loss from muons, electrons and photons in a layered atmosphere. By

assuming that on average $35eV$ are used to produce one ion pair in the air (Porter et al., 1976), it is possible to calculate the number of generated ion pairs down through the atmosphere:

$$q(h) = \int_{P_c}^{\infty} I(P,h)G(P)dP. \tag{3.18}$$

Here $I(P,h)$ is the ionization at height h generated by a particle with rigidity P at the top of the atmosphere. The resulting change in ionization is now given by.

$$\delta q(h) = \int_{P_c}^{\infty} I(P,h)AP^{-\gamma}G(P)dP. \tag{3.19}$$

Figure 3.9 (left panel) presents the results of the Monte Carlo simulation using 3.3 and shows giving the ionization production as a function of the altitude. The calculation is performed at a fixed cut-off rigidity of 6GV representing an average of the global cut-off rigidities. Here it is observed that an ion production of approx. 2-3 ion pairs $/cm^3$ is the average value in the troposphere. This matches well other studies by Carslaw et al. (2002); Usoskin et al. (2004); Bazilevskaya et al. (2008); Usoskin et al. (2008). The black, red curve gives the solar minimum, maximum response, respectively. The strongest reduction in ion production is during the Halloween October 2003 event. The right panel gives the ion production normalized to the solar max to min reduction.

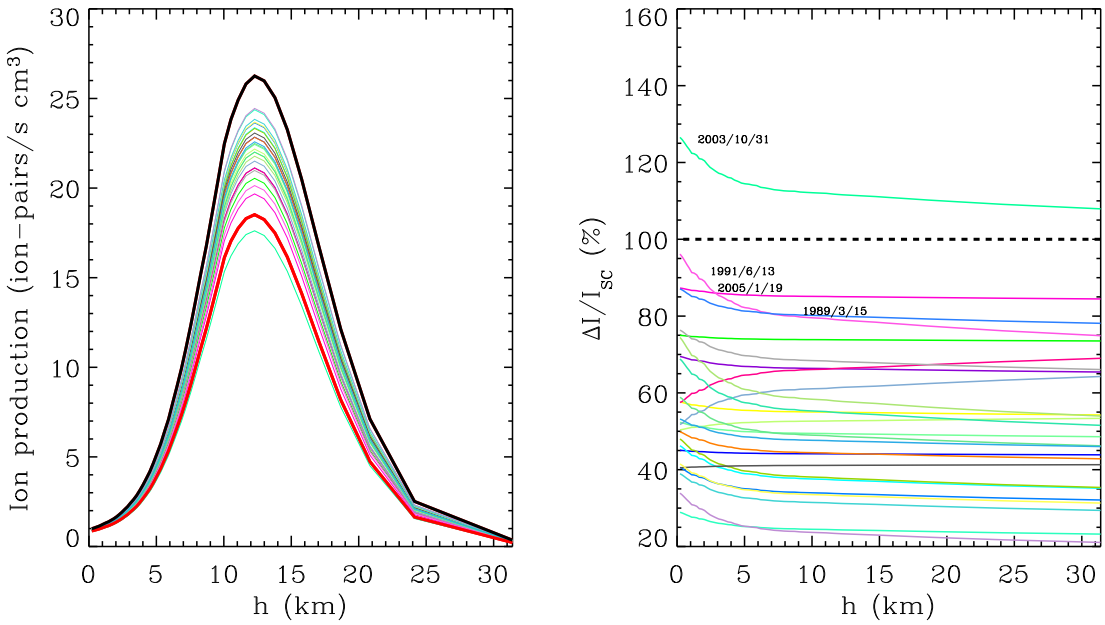

Figure 3.9: Ion production in the atmosphere as a function of altitude for the FDs listed in 3.3. left) The black, red curve gives the solar minimum, maximum response, respectively. right) Ion production normalized to the solar max to min reduction. Dates are annotated for the six strongest events at low altitude. See text for more detail. Figure by Henrik Svensmark. From **Paper 1**

In Appendix A a calculation of the changes in A, γ over the solar cycle is given. Using table 3.1 and the results obtained in Appendix A, it is now possible to calculate the tropospheric change in ionization, as compared to the change in solar cycle ionization for each individual FD. In table 3.3 the decreases in tropospheric ionization in percentage, with respect to the solar cycle event, for all FDs from table 3.1 are listed. The ionization change

is calculated as the mean of the ionization change from 0-3km - altitudes relevant for low cloud creation. It is observed in table 3.3 that only the Halloween 2003 event has a larger

Order	Date	Decrease (%)	A	$\pm\delta A$	γ
0	Solar cycle	100	336	58/50	-1.1 $\pm$ 0.04
1	31/10/2003	119	229	10/9	-0.87 $\pm$ 0.02
2	13/6/1991	87	121	4/4	-0.74 $\pm$ 0.01
3	19/1/2005	83	273	16/15	-1.09 $\pm$ 0.02
4	13/9/2005	75	233	34/33	-1.07 $\pm$ 0.04
5	15/3/1989	70	93	14/12	-0.72 $\pm$ 0.06
6	16/7/2000	70	131	7/7	-0.86 $\pm$ 0.02
7	12/4/2001	64	153	12/11	-0.96 $\pm$ 0.03
8	29/10/1991	56	83	4/4	-0.76 $\pm$ 0.02
9	9/7/1991	54	84	4/4	-0.78 $\pm$ 0.02
10	29/11/1989	54	173	13/12	-1.08 $\pm$ 0.03
11	10/11/2004	53	95	8/8	-0.84 $\pm$ 0.04
12	26/9/2001	50	203	16/15	-1.18 $\pm$ 0.03
13	25/3/1991	48	82	15/13	-0.82 $\pm$ 0.07
14	17/7/2005	47	147	14/13	-1.07 $\pm$ 0.04
15	25/9/1998	45	123	45/33	-1.01 $\pm$ 0.14
16	27/7/2004	45	97	7/7	-0.91 $\pm$ 0.03
17	10/9/1992	44	206	46/38	-1.24 $\pm$ 0.09
18	31/5/2003	44	61	3/3	-0.74 $\pm$ 0.02
19	25/11/2001	39	75	15/13	-0.87 $\pm$ 0.08
20	15/5/2005	38	132	16/14	-1.12 $\pm$ 0.05
21	28/8/2001	37	152	15/14	-1.19 $\pm$ 0.04
22	27/8/1998	36	38	24/15	-0.63 $\pm$ 0.21
23	10/5/1992	35	50	6/5	-0.75 $\pm$ 0.05
24	27/2/1992	33	30	2/2	-0.57 $\pm$ 0.03
25	18/2/1999	33	38	3/3	-0.66 $\pm$ 0.03
26	2/5/1998	28	55	6/5	-0.88 $\pm$ 0.04

Table 3.3: The 26 largest FD events in the period 1987-2007 and the decrease in ionization in percentage with respect to the solar cycle event. The ionization change is the mean value from 0 to 3km height. A and γ are defined in 3.12. The first event lists the fit parameters of the solar cycle as derived in Appendix A. From **Paper I**.

response in ionization over a FD, than the ionization changes over the solar cycle. Also, a number of events (1-6) are only 30% less strong than the solar cycle. If the correlations between low clouds and GCR observed in eg. (Marsh and Svensmark, 2003; Svensmark, 2000) are caused by aerosol growth, table 3.3 shows that a response in clouds above the climatic noise is *indeed* expected, if the FD minimum is large enough.

3.9 Main Conclusions from Variations in Cosmic Ray Induced Ionization during a Forbush Decrase

By focusing on the ionization in the lower troposphere and comparing the FD events to the solar cycle induced ionization change, a reference table has now been derived that is able to test the validity of the GCR-Aerosol-Cloud link for FDs. Comparing table 3.1 with table 3.3 it should be noted that the order of dates are interchanged. Therefore the strength of the FD minimum in a NM (as used in previous work on Forbush decrease effects on climate e.g. (Kristjánsson et al., 2008; Sloan and Wolfendale, 2008)) is not necessarily a good indicator of

the ionization change during a FD. Table 3.3 will now be used to analyze FD effect in cloud and aerosol data in the next chapter.

Chapter 4

Forbush Decrease Effects in Clouds and Aerosol Data

In this chapter analysis of observations of aerosols and clouds during Forbush decreases are presented from four independent sources [1]. The starting point of the analysis is table 3.3 which ranks the FDs according to their induced change in ionization with respect to the change in ionization over the solar cycle. Various means of analyzing the aerosol and cloud data based on this table is given. The results reported indicate that the largest FDs are able to change aerosol as well as cloud properties on a global scale due to changes in ionization.

In order to understand the observational results a brief introduction to the use of remote sensing techniques for aerosols and clouds is given.

4.1 Remote Sensing of Clouds

Since the beginning of the 1980's, satellites have routinely monitored the Earth's cloud clover. The remote sensing measurement principle involves the detection of back scattered radiation to the atmosphere. The back scattered radiation is analyzed by Mie theory (Wolf, 2006) which describes the interaction between light and matter for various wave length regimes. More specifically, a measure of the cloud visibility, the cloud optical thickness τ_c, is given by ((Seinfeld, 2006) p. 1081):

$$\tau_c = b_{ext} h \tag{4.1}$$

where h is the depth of the cloud and

$$b_{ext}(\lambda) = \int_0^{r^{max}} \pi r^2 Q_{ext}(m, \alpha) n(r) dr \tag{4.2}$$

Here $Q_{ext}(m, \alpha)$ is the Mie Scattering coefficient for a given index of refraction m and α the dimensionless size of the particle distribution $\alpha = \pi D_p / \lambda$. D_p being the particle diameter of the droplet number distribution $n(r)$. This equation tells that the optical thickness is linearly dependent on the thickness of the cloud with a size and material dependent coefficient.

[1] A large part of the work behind my thesis has consisted of various analysis of satellite and aerosol data. This includes among other things analysis of long time variation of AOT (Aerosol Optical Thickness) and cloud data. Only the work relevant to FDs is presented here.

The Liquid water content of the cloud is defined as:

$$L = \frac{4}{3}\pi r_e^3 N \rho_w \tag{4.3}$$

where ρ_w is the density of water and r_e the effective radius of the cloud particle distribution. Here the effective radius of the particle distribution is defined as:

$$r_e = \frac{\int n(r) r^3 dr}{\int n(r) r^2 dr} \tag{4.4}$$

Under the assumption of a mono disperse distribution (Seinfeld, 2006) probed at visible wavelengths the optical depth of a cloud can now be approximated as:

$$\tau_c = \frac{3Lh}{2 r_e \rho_w} \tag{4.5}$$

This relation expresses how the optical depth of the cloud is a balance between the cloud liquid water and the effective size of the distribution. For instance removing the smaller particles will increase the overall effective radius but at the same time also reduce N and hereby L. From this equation the cloud albedo can be derived ((Seinfeld, 2006) p. 1081) as:

$$R_c = \frac{\sqrt{3}(1-g)\tau_c}{2 + \sqrt{3}(1-g)\tau_c} \tag{4.6}$$

where g is the Mie scattering asymmetry factor (a factor related to the reflection direction during scattering - typically around 0.85). The changes in droplet concentration is now connected to the cloud optical properties establishing a link between cloud droplet concentration, liquid water content and cloud albedo.

Satellite cloud products are typically derived from information on a number of parameters using all available detection wavelength bands of the satellite instrument and information about the atmospheric profiles of ozone, greenhouse gases, temperature and moisture. Reflection for clouds in the visible region is mostly a function of the cloud optical thickness and for the infrared band mostly a function of the effective radius. Combined with information on clear sky back-scattered radiation it is possible to determine when a Remote Sensing pixel is cloudy or not and what the cloud optical properties are.

4.2 AERONET Aerosols

The AERONET program uses solar photometer to obtain observational data on aerosols in the lower atmosphere from around 400 ground based stations with up to a 10 minute sampling per station (Holben et al., 1998). The stations are well distributed over the globe and have been in continuous operation in the period 1995-2007.

The AERONET photometers work by measuring a Voltage that is proportional to the spectral irradiance (I) at the photometer. Using the Beer-Lambert-Bouguer law (Seinfeld, 2006) the Voltage, V, measured by the photometers is :

$$V(\lambda) = V_o(\lambda) d^2 \exp(\tau(\lambda)_{total} m) \tag{4.7}$$

where V is the digital voltage measured at wavelength λ, Vo is a reference voltage determined at Mauna Loa, Hawaii, d is the ratio of the average to the actual Earth-Sun distance,

τ_{total} is the total optical depth, and m is the optical air mass.

The AOT is a measure of how much light penetrates the atmosphere at a given wavelength, such that at higher AOT less light is penetrating the atmosphere. This number is affected by both the aerosol particle number concentration and effective radius. To calculate the AOT the optical depths related to atmospheric water vapor, Rayleigh scattering, and other wavelength-dependent green house gases must be subtracted from the total optical depth:

$$\tau(\lambda)_{aerosol} = \tau(\lambda)_{total} - \tau(\lambda)_{water} - \tau(\lambda)_{Rayleigh} - \tau(\lambda)_{O_3,NO_2,CO_2,CH_4} \tag{4.8}$$

For the best AERONET stations and for real good measurement days (all day clear sky) approximately 60 measurements of AOT is taken.

The Angstrom Exponent (AE) (Schuster et al., 2006) between two wavelengths is calculated as the slope of $\log(\tau)$ vs $\log\log(\lambda)$:

$$\alpha(\lambda_1, \lambda_2) = -\log \frac{\tau(\lambda_1)}{\tau(\lambda_2)} \Big/ \log \frac{\lambda_1}{\lambda_2}, \tag{4.9}$$

Since the AOT at a given wavelength (λ) is more sensitive to particles that are close to λ in size changes in the AE exponent is a measure of changes in particle distribution. A value of 2 is found in fine mode particle distributions such as smoke particles or sulfates and values close to zero is obtained in coarse mode particle environment such as desert or areas with large sea spray . Typical values of the AE is around 1 to 0.5 over the oceans (Sano, 2004).

In Schuster et al. (2006) a study of mono- and bimodal aerosol distributions by both measurements and model reached a number of conclusions on the Angstrom exponent as a tool to probe aerosol size distribution. Useful for the the present study, it was found that the long-wavelength Angstrom exponent (670,870 nm) has greater sensitivity to the fine mode aerosol fraction than the short wavelength Angstrom exponent (380,440 nm). Similarly, the short-wavelength Angstrom exponent has greater sensitivity to the fine mode effective radius than the long-wavelength Angstrom exponent. See Figure 4.1. A decrease in AE expresses an increase in the effective radius of the aerosol distribution which then may be interpreted either as removal of small mode particles or an increase in the large mode particles. In this chapter, the smallest available wavelength pair in the AERONET database from (340,440 nm) is used and interpreted as changes in the small mode aerosol distribution.

4.3 Satellite and Aerosol Data

Each satellite and ground based measurement is subject to measurement errors and random noise. It is therefore important to use several data sets to exclude statistical biases and data set errors. In this thesis I have focused on four independent data sets.

International Satellite Cloud Climatology Project (ISCCP) (Rossow and Schiffer, 1999) has been running since 1982 and have delivered 3-hourly (D1-data) as well as monthly mean (D2-data) global cloud properties collected from various satellites and weather stations.

For ISCCP we used Low-clouds-D1 3-hourly readings over the oceans below 3.2 km. More specifically we extracted product p28 and p29 (number of IR cloudy pixels from 680-1000mb) and the total number of pixels (p11) and calculated the IR Low clouds over oceans as $(p28 + p29)/(p11)$. The products were extracted using d1read.1var.f downloaded from

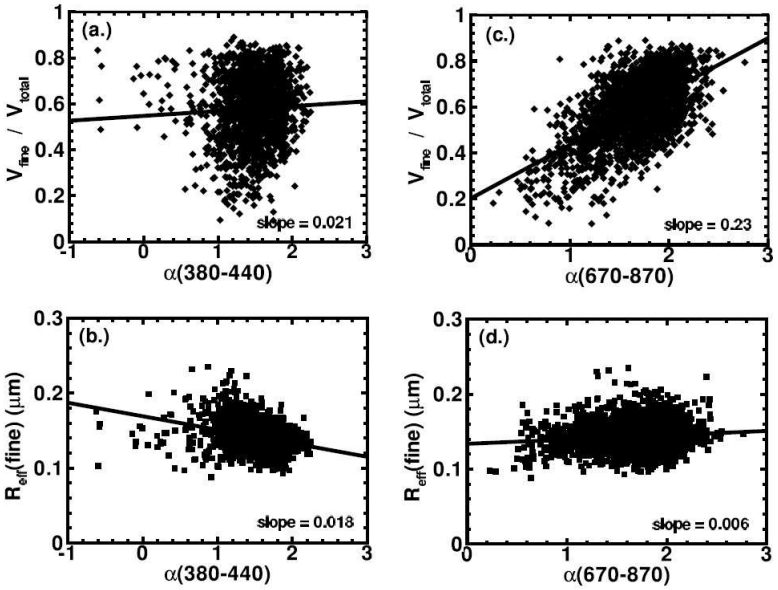

Figure 4.1: Fine mode volume fraction and fine mode effective radius as a function of the (380, 440 nm) Angstrom exponent and (670,870 nm) Angstrom exponent. The long-wavelength Angstrom exponent has greater sensitivity to the fine mode aerosol fraction than the short wavelength Angstrom exponent and the short-wavelength Angstrom exponent has greater sensitivity to the fine mode effective radius than the long-wavelength Angstrom exponent. From Schuster et al. (2006)

ISCCP website. We made daily averages over the subtropical/tropical ocean from 40 degrees N to 40 degrees S of only those pixels where all 8 daily values where present for a particular day. We decided to use ISCCP only over the ocean due to known problems with ISCCP in determining cloud pixels over Land.

Moderate Resolution Imaging Spectroradiometer (MODIS) (Platnick et al., 2003) MODIS is an infrared and visible passive sensor launched aboard two American satellites Terra (operating since 2000) and Aqua (operating since 2002). A multitude of atmospherical data can be achieved from http://modis-atmos.gsfc.nasa.gov. Cloud properties on a 1 degree grid can be obtained in daily level 3 format already preprocessed and error cleaned. Since it has the longest data availability, for the present analysis the *MOD*08*D*3 cloud product from Terra is used. With over 600 geophysical products available form MODIS only the subsets "Cloud_Fraction_Combined´´ and "Cloud_Fraction_Liquid´´ were analyzed. "Liquid´´ is the cloud fraction liquid clouds and "combined´´ the cloud fraction for all cloud phases including ice clouds and liquid clouds. The hdf data was read into an IDL (Interactive Data Language) program and each daily map was averaged to a single daily global value during the FD periods.

Special Sensor Microwave/Imager (SSM/I) (Weng et al., 1997) The cloud observations come from the Special Sensor Microwave/Imager (SSM/I) instruments of the Defense Meteorological Satellite Program. The present analysis used the liquid water product of SSM/I returning pixels from liquid water clouds over the ocean available since 1987. The hdf data was read into an IDL program and each daily map was averaged to a single daily global value during the FD periods

AERONET (Holben et al., 1998) An IDL program was developed to compute global Angstrom exponent (AE) from daily averages over the FD periods. The global mean of the AE is com-

puted by a mean of all daily stations that return more than 20 measurements a day as:

$$AE(\text{daily global mean}) = \sum_i \frac{\sum_k (AE(k,i)/N_k)}{N_i}, \tag{4.10}$$

where N_k must be larger than 20 (N_k is maximum 60 for the best stations) and i is the sum over the stations that have over 20 measurements per day. This limits the list to approx 40 AERONET stations but do ensure continuity/stability in the data series and ensures that the global average is not made from stations that return few measurements with stations that return many measurements since this would create biases in the mean.

4.4 FD Minimum Analysis

Most of the work presented in chapter 3 and in this chapter was initiated by an analysis of SSM/I cloud data for the major FD events. Previous work in the group had failed to see clear signals in ISCCP cloud data and it was believed that cloud noise (see section 4.9) as well as linear trends in the cloud data caused by seasonal variation was the reason for this. However, the analysis of the most recent major FD events (31/10/2003, 19/1/2005 and 13/9/2005) indicated a cosmic ray induced signal in the SSM/I data. This led to the work presented in these two chapters and **Paper I**. Figure 4.2 shows an analysis of the 6 largest FDs for daily globally averaged SSM/I data. A similar analysis to that of Figure 4.2 was performed for all the data mentioned in the previous section. Most of the major FDs seem to have an effect on the cloud and aerosol data but with more or less scatter for each response. The figures also indicate, that the liquid water content in the clouds decreases after 6 to 10 days as compared to the FD minimum. This lag in the cloud data as compared to the FD minimum could represent the time it takes for the aerosols to grow to CCN sizes, a hypothesis that is examined in next section and investigated in a model in next chapter.

4.5 Aerosol Growth Times to CCN

In **Paper I** the apparent lag as compared to the FD profile by 5-6 days and 7-9 days in the change of aerosol and cloud properties, respectively, was explained as a feature related to aerosol growth. The hypothesis is that a decrease in ionization during a FD inhibits aerosol nucleation. The CCN size particles will then respond to this decrease by producing less CCN after a time period related to the growth period of the nucleation mode to CCN size particles. The decrease is expected to appear first in the aerosols and then have its effect on the cloud optical properties. It all boils down to aerosol growth times which remains an open question.

In Kulmala et al. (2004) the growth rate of aerosol particles at a forest site in Finland are observed by ion and aerosol spectrometers. They find an increasing growth rate with the size of the aerosol cluster but find no evidence for ion induced growth for the measured sizes above 3 nm. The growth rates were of the order of 2-14 nm/h indicating that CCN size particles are generated within an order of a day. A later work by the same group (Kulmala et al., 2004) arrives at a growth rate of 1 nm/h for $10^7 mole/cm^3$ sulfuric acid. This would indicate much longer growth times to CCN of the order of 4 days.

In Kuang et al. (2009) both analytical as well as field campaign measurements are used to calculate the growth rate into CCN size(100 nm) of the order of 3-22nm/h. The pre-existing CCN number concentration was found to increase with a factor of approx 4 when new particles are formed. This indicates that on the order of a 1-2 days CCN size particles could

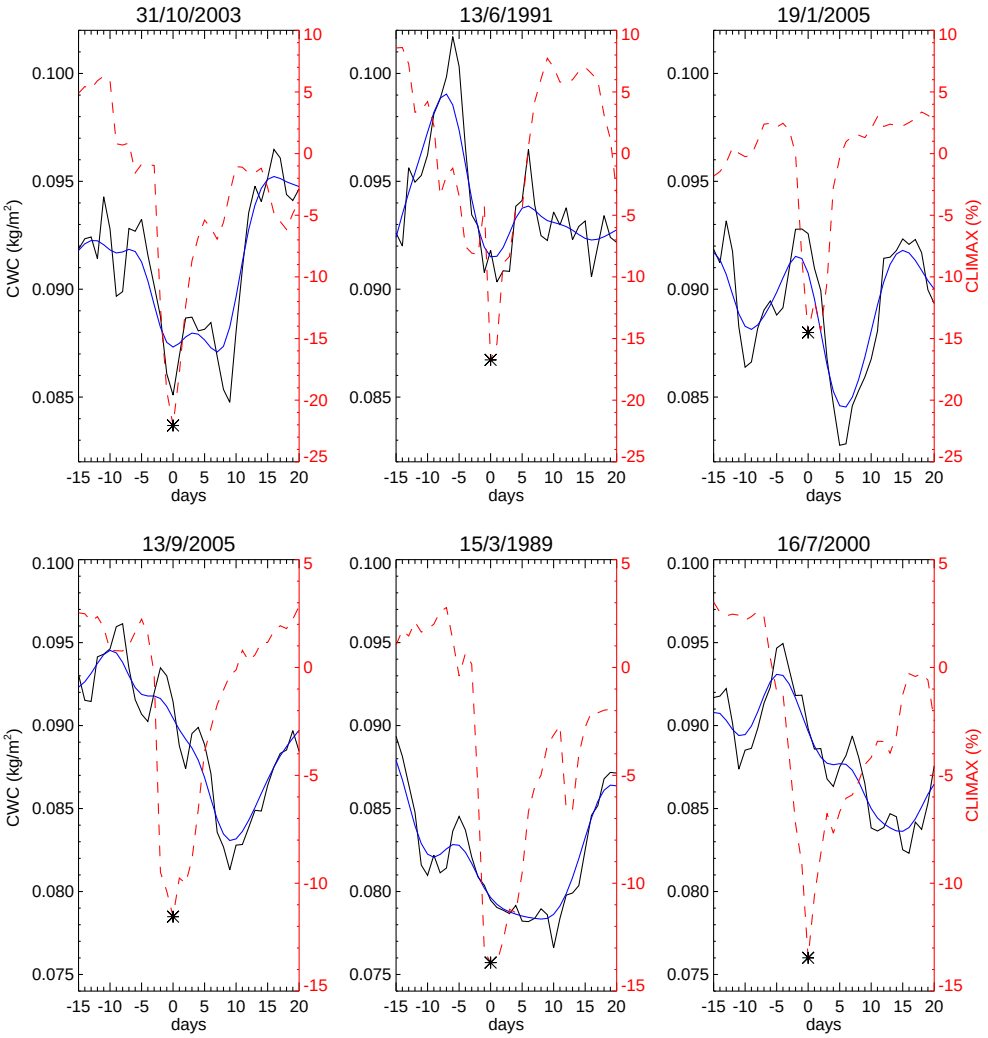

Figure 4.2: Cloud liquid water from SSM/I during the 6 greatest FDs. The blue line is a Gaussian filter applied to the daily data. The red line is the corresponding FD profile as measured by Climax NM. From **Paper I**.

be altered by changes in the nucleation size mode. This is in contrast to other studies by Pierce and Adams (2007, 2009) where the primary aerosols completely inhibit ion induced growth to CCN sizes expecting no impact of a FD on the optical properties at all.

A study by Arnold (2006) arrives at growth times up to CCN size on the order of 4-6 days for a model study of sulfuric acid growth in the troposphere. This is illustrated in Figure 4.3 where CCN size particles (30 nm) first appear after 2 days.

Until more observations and experiments can lay a better scientific foundation, it is only possible to include that the findings could potentially be a results of the aerosol growth. In the next chapter (see section 5.4.7) I try to model the results observed to understand whether it is realistic to expect such a response. To reveal if the signal is indeed caused by the cosmic rays several FDs were averaged as described in next section.

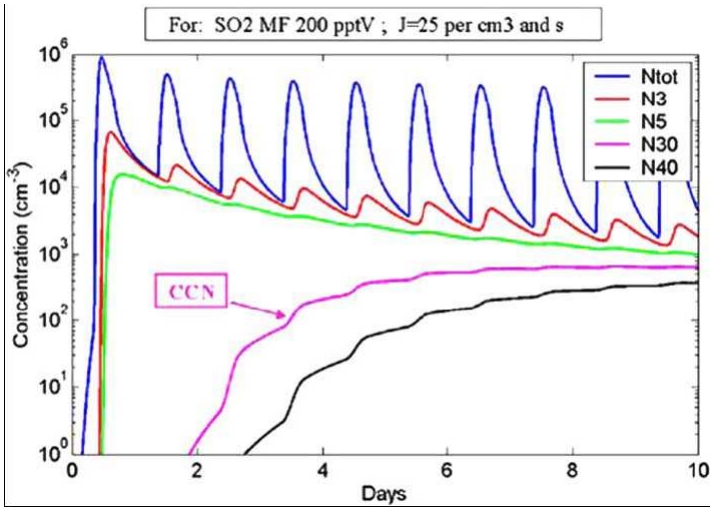

Figure 4.3: Results of a 10-day model simulation of atmospheric gaseous H2SO4, and aerosol particle number concentrations at 10 km altitude. (Arnold, 2006)

4.6 FD Minimum Mean Analysis

All data were subject to the same mean analysis. A number of FDs from 3.3 was selected. For each data set, FD_{data}, of global average values and each day i (15 days prior to the FD minimum and 20 days after), a mean value for k number of FD dates was calculated as

$$\text{mean(i)} = \sum_{k} FD_{data}(k,i)/k \tag{4.11}$$

Both the real physical data and the physical data in percentage change around the mean were analyzed. The first method is good to observe the actual physical values and the other method is good to avoid base level or seasonal behavior affecting the mean. We observed more or less the same patterns for the two methods. Figure 4.4 shows such a mean analysis for the 5 strongest FDs.

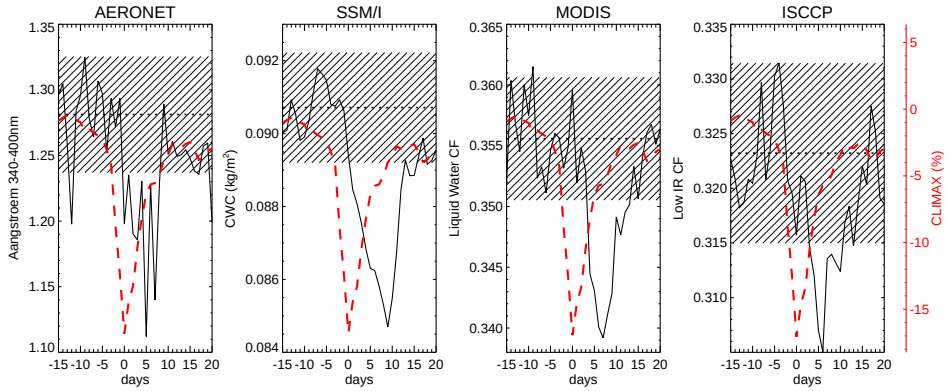

Figure 4.4: Mean analysis of the 5 largest FD events. Here an average number for each day is obtained by calculating the average value from 5 events for a given day compared to the FD minimum. 4 data sets are presented. From **Paper 1**.

With AERONET having the most scatter each data set shows a clear decrease with a lag compared to the FD minimum. A FD signal appears to be present both in aerosols and cloud data. The lag in aerosols seem to be a day or two shorter than for clouds indicating

that the response to the FD happens first in aerosols and then in clouds. The grey error bars are the level of random fluctuation as explained in section 4.9. All signals are well below the error bars. Since the geometrical shape of the FDs are a distinct feature of cosmic rays (see discussion in section 2.5), it strengthens the belief that the decreases in clouds and aerosols after the major FDs are caused by cosmic rays.

For ISCCP subtropical/tropical latitudes (from 40N to 40S) were used in the analysis presented in **Paper I**[2]. Since we require all 8 daily values in each pixel to be present for the daily average, most counts from the northern latitudes areas are not included, and it therefore makes only a small difference on the signal whether or not you have these latitudes with. This is illustrated in Figure 4.5 where the area of interest is extended to 70 degrees.

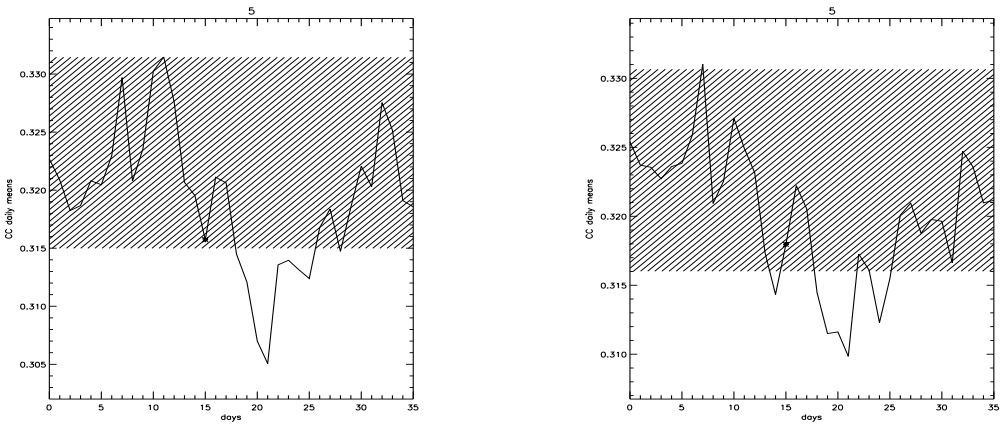

Figure 4.5: Left) Figure 4.4 for ISCCP taken from 40N to 40S. Right) the same analysis but extending the area to 70N to 70S. Note that day 15 is the FD minimum in this plot.

In Figure 4.6 the percentage decreases in MODIS liquid cloud fraction are illustrated for the FDs (since 2000) in 3.3. The FDs are averaged in bundles of 3 where the top left plot is a mean of the three largest events since 2000 (#1,3,4 in 3.3), the top righ plot the mean of (#6,7,11 in 3.3), the bottom left plot the mean of (#12,14,16 in 3.3) and the bottom right the mean of (#18,19,20 in 3.3). Here a decrease is observed after the FD minimum for the three largest FDs that vanishes for the mean of the smaller FDs. However, uncertainty remains whether the observed results in Figure 4.4 are a single randomly large fluctuation that causes the mean to fluctuate thereby creating a random signal. To completely rule this out a statistical analysis for each FD event must be done.

4.7 FD Minimum Statistical Scatter Analysis

Large random fluctuations in the data for a single FD date, could potentially mask out or appear as a signal from cosmic rays. Therefore, the data response for each single FD should be treated similarly. To do this, each FD is smoothed with a Gaussian filter of width 10 days and a sigma of 2 days, producing the blue lines as shown in Figure 4.2. First, a base level is calculated as the mean of a 10 day period, calculated 15 days prior to the FD minimum (day 0): base level $=$ mean(data(day(-15) to day(-5)). Based on the Gaussian filtered data the minimum value in % after the FD (From day 0 to day 20) is now determined. By repeating this for all FD dates and data sets, Figure 4.7 is produced:

[2]When **Paper I** was submitted we used ISCCP data with this mask, since we had data with this mask readily available. Later we extended the analysis to 70 degrees and found little effect from the Northern latitudes.

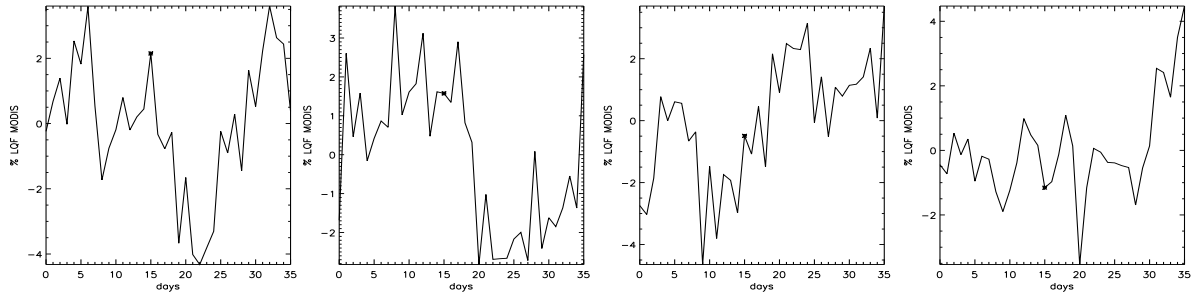

Figure 4.6: MODIS liquid cloud fraction percentage decrease during FDs in bundles of 3 according to table 3.3. From left FD 1-3, FD 4-6, FD 7-9, FD 10-12. Note that day 15 is the FD minimum in this plot. See text for details.

Figure 4.7 shows data from MODIS Cloud fraction (CF), MODIS Liquid Cloud Fraction (LCF), AERONET Angstrom exponent (340-440 nm), SSM/I Cloud liquid Water, ISCCP all clouds infra red (IR) and ISCCP low clouds IR. The solid line is the regression line. Above each plot the regression coefficients of the solid line $Y = A + B * X$ is given (first number A, second number B). Below each plot the uncertainties of A, B are listed. By comparing the sigma coefficients of B to the value of B and the number of data points for each data set it is possible to determine if the slope of the line is significantly different from zero and hence representing a signal and not noise. All regression coefficients are significantly different from zero with a significance above the 95% level (in the case of MODIS only above the 92% level).

The liquid cloud fraction and cloud liquid water decrease in Figure 4.7 is on the order of 5-10% for the largest FDs. For aerosols the scatter is larger and this number is more difficult to determine but is on the same order of magnitude as in clouds , i.e from 5-10%. The results indicate that the FD induced signal in clouds and aerosols scale with the changes in ionization. This supports the existence of the GCR-Aerosol-Cloud link.

4.8 Spatial Correlation Analysis

It is important to analyze where the global signal from the FDs observed in the previous sections come from. Is it a result of equatorial or polar changes or a combination? This question might be answered by a spatial correlation analysis using epoch analysis and the information on the lag in cloud data as compared to the FD minimum. Using Climax data as a proxy for the cosmic ray signal in the troposphere the spatial correlation analysis is first done by averaging the cloud data for 5 events for all pixels. This map consists of latitude vs longitude pixels for each 36 days. By correlating each lat-lon pixel from SSM/I and MODIS LQF throughout the 36 days with the Climax signal the map in 4.8 appears. Notice that the correlation is performed with a lag in the cloud data on 10 days to be able to test the lag as observed in Figure 4.4. Other lag analysis reveal slightly different patterns but no clear picture emerges whether the signal stabilizes when the lag is 8-10 days compared to other values.

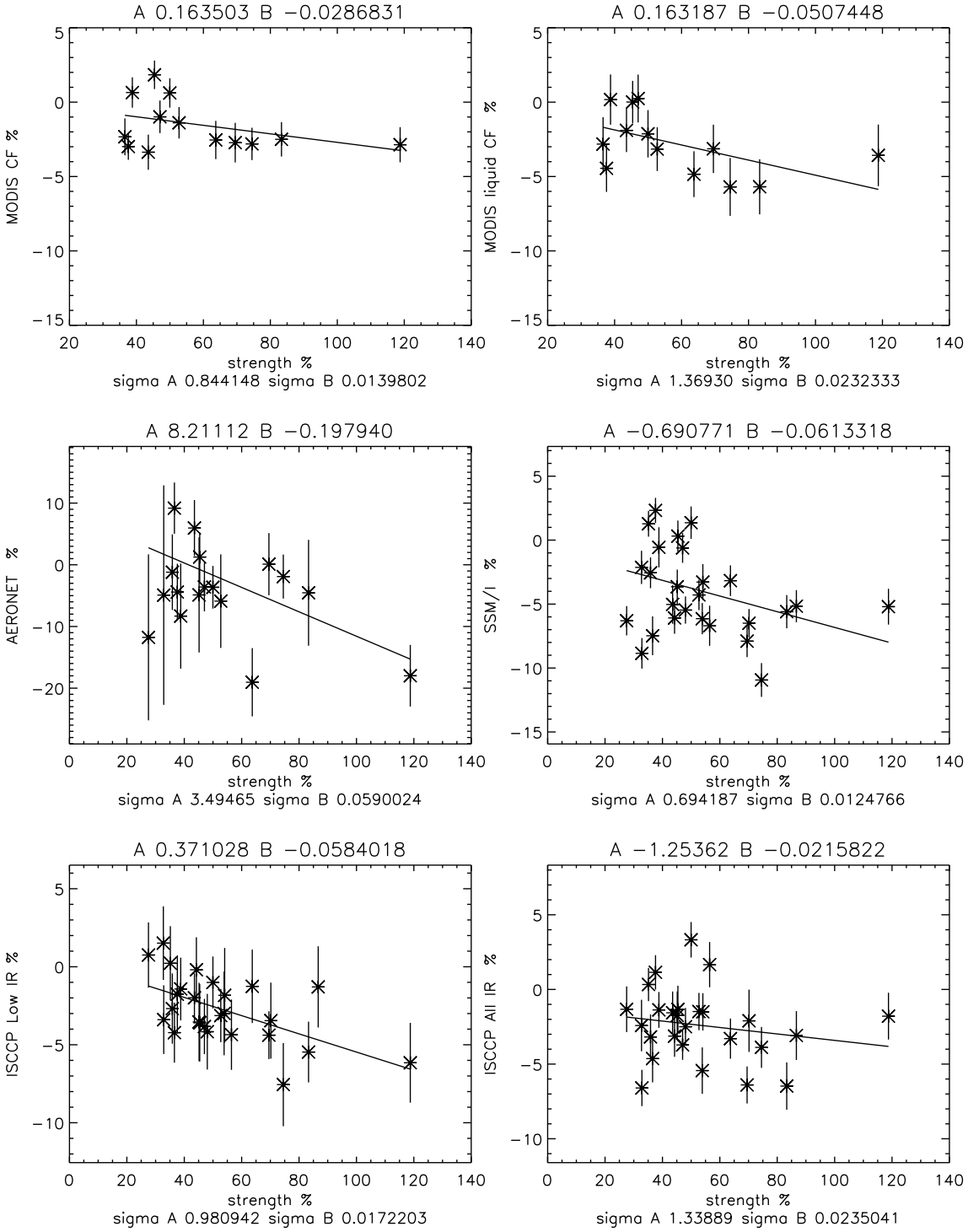

Figure 4.7: Minimum of Gaussian filtered data curves (width 10 days, sigma of 2 days) after each FD as a function of FD % strength in ionization as compared to the solar cycle, see 3.3. The minimum is compared to a 10 days long base level defined 15 days prior to the FD minimum. The solid line is the regression line and above each plot the regression coefficients of the solid line $Y = A + B * X$ is given (first number A, second number B). Below each plot the uncertainties of A, B are listed. Six data sets are analyzed: MODIS Cloud Fraction, MODIS Liquid Cloud Fraction, AERONET Angstrom exponent (340-440 nm), SSM/I Cloud liquid Water, ISCCP all clouds Infra red (IR) and ISCCP low clouds IR.

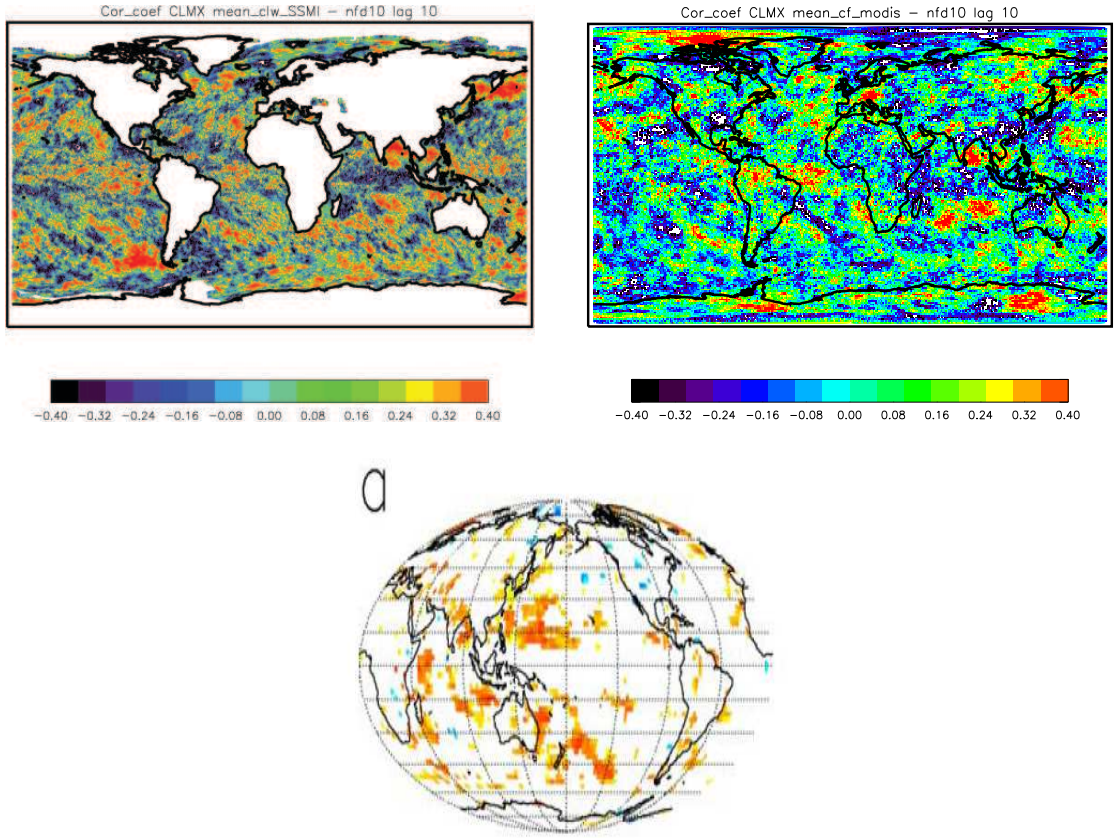

Figure 4.8: Top left) Spatial correlation of SSM/I daily data with Climax NM data over the whole 36 days FD period (15 days before and 20 days after). A mean of 10 FD events with a lag of 10 is presented. Top right) The same analysis repeated for Modis LQF data. Bottom) Low clouds and GCR spatial correlation from 1983-1994. Figure 3a from Marsh and Svensmark (2003)

The spatial correlation map for MODIS LQF and SSM/I during a FD should be compared to the correlation map in Figure 3a for low clouds and GCR in Marsh and Svensmark (2003). For MODIS some overlap seem to appear in the areas of the Indian ocean and off the coast of Chile but SSM/I seem not have the same areas. More careful analysis of the spatial correlations is needed in order to get a clearer picture of where FDs affect clouds, but within the time frame of this thesis this was not possible. See section 6.0.2.

4.9 Data Noise

All data have both fluctuations and measurements noise that can make signal processing difficult. It is therefore important to use statistical tools to analyze if a cosmic ray induced signal is present. To illustrate this all FD data above were subject to a random test determining the noise level of a particular FD analysis. For the work presented in **Paper I** generally two kinds of noise tests were done:

For section 4.6 it was needed to determine if the signal observed could be caused by random fluctuations. Therefore, a large file of random dates for the particular data set was generated and the corresponding data extracted. The random data sets were then subject to an epoch analysis as described by section 4.6 generating one random realization containing the mean of 5 random events. Finally, the standard variation over the whole period was calculated for a set of hundred realizations. These standard variations are the grey bars in

Figure 4.4 and Figure 4.5 and are used to check if the signal is above or below a true random signal. Table 4.1 lists the different standard deviations and mean based on the random realizations for different numbers of FDs for MODIS LQF, ISCCP, SSMI/I and AERONET. As expected the standard variations decreases with more FDs. Furthermore, the standard deviation vary from data set to data set with AERONET having the largest deviation and SSMI/I the least.

MODIS	Mean(mean)	Mean(σ)	Mean(σ) %	AERONET	Mean(mean)	Mean(σ)	Mean(σ) %
1	0.344	0.0109	3.1	1	1.278	0.126	9.8
3	0.349	0.0063	1.8	3	1.290	0.0710	5.4
5	0.350	0.0050	1.4	5	1.297	0.0550	4.2
10	0.350	0.0034	0.9	10	1.302	0.0381	2.9
13	0.350	0.0030	0.8	15	1.299	0.0307	2.4
ISCCP	Mean(mean)	Mean(σ)	Mean(σ) %	SSM/I	Mean(mean)	Mean(σ)	Mean(σ) %
1	0.321	0.0162	5.1	1	0.0812	0.00267	3.3
3	0.320	0.0097	3.0	3	0.0879	0.00174	2.0
5	0.321	0.0082	2.6	5	0.0879	0.00135	1.5
10	0.320	0.0066	2.1	10	0.0879	0.00095	1.1
15	0.321	0.0060	1.9	15	0.0878	0.00073	0.8
20	0.321	0.0057	1.8	20	0.0878	0.00064	0.7
26	0.320	0.0054	1.7	26	0.0878	0.00055	0.6

Table 4.1: Observational standard deviations for FD minimum mean analysis by random realizations. The number below each FD is the number of random FDs used. See section 4.6 for details.

For section 4.7 a different approach was needed. Here the variations for each day for a particular FD during an event was calculated by subtracting the Gaussian smoothed curve from the original data set. This created 36 residues that was used to calculate the overall standard variation for this particular FD event. This standard variation is represented by the errors on each data point.

To visualize the noise fluctuations an additional noise test was performed on a year data set for ISCCP. Left in Figure 4.9 a smooth curve is applied to the ISCCP time series and the standard deviation is calculated for a varying size of the smooth filter. This leads to a 1.6% standard deviation for the daily resolution images and shows as expected that applying a smooth filter significantly reduces the noise in data. It is possible to calculate this slightly differently by dividing the data of a year into segments of different sizes (say 1 day segments). By calculating the mean of the standard deviation of all these segments and varying the segment size a similar result for the standard deviation of ISCCP data appears. This is shown in the right of Figure 4.9.

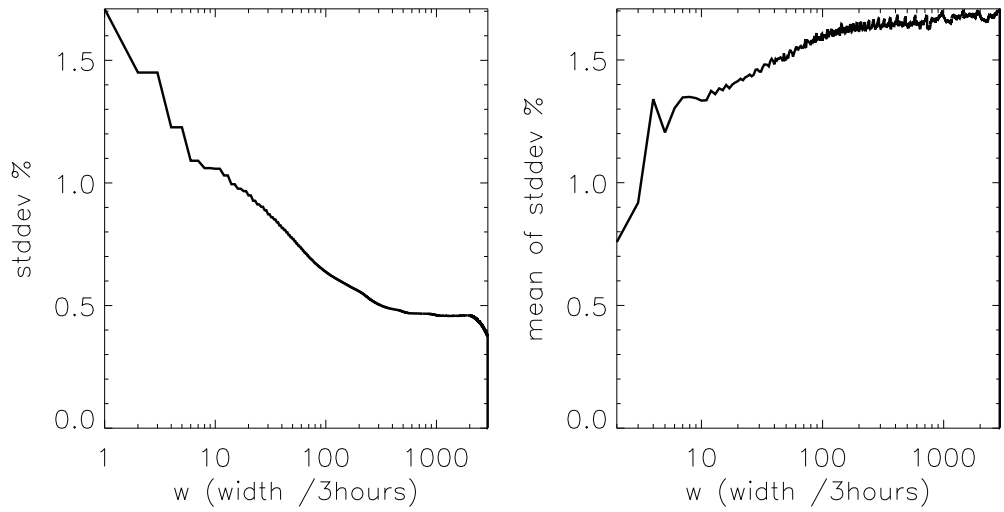

Figure 4.9: left) Standard deviation of ISCCP low IR cloud data. 1 year array smoothed with width w. right) Mean of standard deviation of ISCCP low IR cloud data. All arrays with width w. 1 year data.

4.10 Main Conclusions from Forbush Decrease Effects in Clouds and Aerosol Data

The results obtained in this chapter indicate that cosmic ray induced ionization affects aerosol and cloud data on time periods related to aerosol growth. Section 4.6 showed that significant decreases in the short wavelength Angstrom exponent AE(340-440) nm from AERONET appear approximately 5 days after the largest FDs. Similar significant decreases in the cloud liquid water and liquid cloud fraction were observed after approx 8 days after the FD minimum in MODIS, ISCCP and SSM/I data. The results point to a mechanism involving aerosol growth to CCN sizes that in turn affect liquid clouds.

The analysis of global averaged data in Figure 4.7 showed the response in each data set to each FD from table 3.3. By deriving the statistical scatter for each point and calculating the slope of all points, it was shown that the the observed decrease in aerosols and liquid clouds is significant, and scales with the size of the FD induced ionization change in the troposphere.

Chapter 5

The Aerosol Growth Model

The previous work in this thesis has focused on the description on how ionization may change aerosol formation on short time scales and has presented evidence of this from laboratories and theory (see section 2.4 and Chapter 3 and from observational data (see Chapter 4). Focus will now be on modeling the observed changes in the laboratory as well as in the observational data.

This chapter describes an aerosol growth model for neutral sulfuric acid particles assuming an initial distribution of stable nucleated clusters. The model takes condensation and coagulation into account and include wall and particle losses but neglects evaporation.

It will be shown, that the production of CCN size particles is sensitive to changes in stable cluster production rates and sulfuric acid gas concentration. Furthermore, laboratory experiments of aerosol growth using ion source are examined with the model. Last, the observational changes in the angstrom exponent during a FD is examined under realistic marine aerosol growth conditions influenced by ionization changes.

5.1 Description of the Model

In (Svensmark et al., 2007) an experiment is described that links the growth of sulfuric acid particles ($>$ 3nm) under atmospheric conditions to an increase in tropospheric ionization generated by cosmic rays. The nucleation rate of stable sulfuric acid in this experiment proved to be faster than expected from classical nucleation theory and hence an ion induced particle nucleation mechanism was proposed where the creation of ions by cosmic rays leads to the formation of ultra fine cloud condensation nuclei. It was speculated that the charge produced by the ionization in cosmic ray showers initially nucleates a cluster before it detaches due to excitation by photons or the release of chemical energy within the initial cluster. This process could repeat itself many times until the electron is lost by recombination or aerosol attachment. The initial nucleated particles will then grow via classical growth mechanisms including condensation, evaporation, recombination, coagulation and additional losses. The model presented here was first developed to model the growth of the initial nucleated particles and link the nucleation model for the stable clusters to the particle growth model in order to describe the findings in Svensmark et al. (2007). Later it was extended to also describe particle growth in remote marine environments to be able to model the observations presented in the preceding chapter.

Three cases will be presented based on the same particle growth model:

- Model of aerosol growth in a large atmospheric chamber. See section 5.2. Here it is

- Model of aerosol growth in a small atmospheric chamber. See **Paper II** and section 5.3.

- Model of aerosol growth in a Marine environment during a FD. See **Paper III** and section 5.4. This case is fundamental for the thesis.

First, the model itself is described.

5.1.1 The General Dynamic Equation

The growth model is described by the general dynamic equation (GDE) which is a partial differential equation for aerosol particle growth. Many methods can be used to solve the equation but here a sectional method is used where bins of variable sizes represent different sizes *nc* of the molecular clusters expressed as the number of sulfuric acid molecules in the cluster. The GDE is then solved to determine the number distribution n that describes the number of aerosol particles in the different bins. The choice of the sizes of these bins is arbitrary but can limit the integration accuracy. In this work the initial clusters are sampled with a step size of 1 molecule up to 70 molecules (approx 3.5 nm) where the step size is then increased with a factor of 1.2 (1.1 is used in section 5.4). Letting i represent bin number i and *ncluster* a limit to the maximum number of clusters in the simulation, the cluster sizes are defined by:

$$\begin{aligned} nc(i) &= [0, 1, 2, .i., 69, 70, 75, 85, 100, 120, 145, 175, 210, 250, 250 * 1.2^{i+1}], \\ & i \in [0, ncluster] \end{aligned} \tag{5.1}$$

Adopting equivalent notation to that of (Lovejoy et al., 2004) the discrete partial derivative of the neutral sulfuric acid cluster distribution function for bin i, n(i) is given by:

$$\begin{aligned} \frac{\partial n(i)}{\partial t} &= \frac{k^c_{i-1}[H_2SO_4]n(i-1)}{(nc_i - nc_{i-2})/2.} - \frac{k^c_i[H_2SO_4]n(i)}{(nc_{i+1} - nc_{i-1})/2.} + \\ & 0.5 \sum_l \sum_j k^e_{j,l} n(j) n(l) \frac{(nc_l + nc_j) - nc_{i-1}}{(nc_i - nc_{i-1})} \delta_{(n_l+n_j),[nc_{i-1},nc_i]} + \\ & 0.5 \sum_l \sum_j k^e_{j,l} n(j) n(l) \frac{nc_{i+1} - (nc_l + nc_j)}{(nc_{i+1} - nc_i)} \delta_{(n_l+n_j),[nc_{i+1},nc_i]} - \\ & \lambda_{par} n(i) - n(i) * \sum_l (k^e_{i,l} * n(l)) \end{aligned} \tag{5.2}$$

The first term in the first line is the production of n(i) onto the previous bin by condensation of a sulfuric acid molecule. Hence the second term in the first line is the loss in bin i due to creation of a molecule in bin i+1. The next two terms represent the coagulation of the individual clusters. Here the delta functions and the fractions take the increasing sizes of the bins into account and make sure to fractionalize the coagulated particles into the correct bins. The sums makes sure that particles of all sizes are accounted for. The last term is a loss term used to account for losses of particles to the wall and loss of particles due to coagulation.

5.1.2 Condensation

When the sulfuric acid concentration is sufficiently high compared to the number of stable nucleated clusters condensation is by far the most important process.

As can be seen from 5.2 condensation is controlled by the individual condensation coefficient for the condensation of a sulfuric acid molecule onto a cluster i. Following the approach of (Laakso et al., 2002) these coefficients $[cm^3/s]$ are expressed by the cluster diameters d_i and diffusion coefficients D of the i-th molecule and first molecule:

$$k_i^c = 2\pi 100(d_i + d_1)(D_1 + D_i)\frac{(Kn + 1.)}{(0.377Kn + 1. + 4.(Kn^2 + Kn)/(3.\alpha))} \tag{5.3}$$

Here $Kn = 2.\lambda/(d_i + d_1)$ is the dimension less Knudsen number expressing the viscosity of the cluster in the gas and α is the mass acommodation coefficient. A value of α below 1 will slow the droplet growth but is set to 1 in our program according to Laaksonen et al. (2005). The mean free path $\lambda = 3(D_1 + D_i)/sqrt(v_i^2 + v_1^2)$ (Lehtinen and Kulmala, 2002) is a function of the cluster velocity for a cluster with $nc(i)$ amount of sulfuric acid particles :

$$v_i = \sqrt{8RT/(\pi nc(i)(m_{H_2SO_4} + (1/x - 1)m_{H_2O}))} \tag{5.4}$$

Here RT is the gas constant R times the Temperature T and $m_{H_2SO_4}$ and water m_{H_2O} are the molecular weights of sulfuric acid and water, respectively.

Determining the cluster diameter d_i is not trivial since the water content to the sulfuric acid particle (the mole fraction x) will change with cluster growth. To determine the cluster diameter d_i and mole fraction x as a function of number of sulfuric acid molecules $nc(i)$ the following equation system must be solved.

$$\begin{aligned} d &= 2\left(\frac{(nc(i)/x)(98x + 18(1 - x))}{4\pi Na(1.8x + (1 - x))/3}\right)^{1/3} \\ x &= co_1 * d^{co_2} + co_3 \end{aligned} \tag{5.5}$$

Here co_1, co_2, co_3 are parameters that changes with the relative humidity used in the simulation and Na is the Avogadros number. It is hence assumed that an initial sulfuric acid particle is wet and contains water molecules according to (Seinfeld, 2006).

Having determined the particle diameter the diffusion coefficient $[cm^2/s]$ is given by (Bruce et al., 2001):

$$D_i = 0.001T^{1.75}\sqrt{\frac{1/m_{air} + 1/m_{H_2SO_4}}{p * (v_{air}^{0.33} + v_{H_2SO_4}^{0.33})^2}} \tag{5.6}$$

where p is the pressure in atmospheres and $v_{H_2SO_4}, v_{air}$ the diffusive volumes of sulfuric acid and air, respectively (Bruce et al., 2001).

5.1.3 Coagulation

The coagulation coefficients are determined from (Laakso et al., 2002). These coefficients can be used for all Knudsen numbers and hence in all growth regimes from diameters of

few Ångströms to sizes up to > 1 microns. The coagulation coefficients are determined from:

$$k_{i,j}^{e} = \frac{k_c^b}{\frac{R_{ij}}{R_{ij}+\sigma_{ij}} + \frac{4D_{ij}}{v_{ij}R_{ij}}} \tag{5.7}$$

where

$$k_c^b(i,j) = 4\pi(r_i + r_j)(D_i + D_j) \tag{5.8}$$

Here $R_{ij} = R_i + R_j$, $v_{i,j} = \sqrt{v_i^2 + v_j^2}$ and $\sigma_{ij} = \sqrt{\omega_{ij}^2 + \omega_{ji}^2}$ where

$$\omega_{ij} = \frac{(R_{ij} + \gamma_i)^3 - (R_{ij}^2 + \gamma_i^2)^{1.5}}{3R_{ij}\gamma_{ij}} - R_{ij} \tag{5.9}$$

with $\gamma_i = 8D_i/(\pi v_i)$.

The diffusion coefficients are similar to those defined in 5.6 but now include the Cunningham correction factor C_c:

$$D_i = \frac{kTC_c}{6\pi\mu R_i} \tag{5.10}$$

where $C_c = 1 + Kn(a1 + a2\exp(-a3/Kn)))$ (with $a1 = 1.142, a2 = 0.558$ and $a3 = 0.999$). The Knudsen number Kn is calculated in a similar way as with the condensation coefficients. In this approach the diffusion coefficient appear in the Knudsen number (in λ) and therefore the diffusion coefficient for condensation must be used to calculate the coagulation diffusion coefficient with correction factor.

5.1.4 Nucleation

This model does not go into the chemistry of the nucleation but assumes that nucleated particles are placed into a bin *cunit* at a given rate representing particle formation by nucleation. Typically these particles are 5 molecules big and are thus placed in bin 5 with a rate s, ie. $cunit = 5$. The value of 5 sulfuric acid molecules was chosen from an estimation of the critical cluster size in Svensmark et al. (2007). See "Program input".

Ion production, Q, in the troposphere is approx. $3 - 5\frac{\text{pair}}{cm^3 s^1}$ as shown by Figure 3.9. This production is related to the ion concentration, I, (Raes and Janssens, 1985) as:

$$\frac{dI}{dt} = Q - \alpha I^2 \tag{5.11}$$

which in the steady reduces to

$$I = \sqrt{Q/\alpha} \tag{5.12}$$

where $\alpha = 1.6 * 10^{-}6cm^{-3}s^{-1}$ is the ion-ion recombination loss term.

Nucleation experiments by (Svensmark et al., 2007) seem to point towards a square root dependency between cluster production, s, and ion production Q. Using eq. 5.12 the relation between s and Q becomes:

$$s = s_0\sqrt{Q} = s_0 I \tag{5.13}$$

Input parameter	Value	Explanation
conden flag	1/0	Condensation on/off
coagul flag	1/0	Coagulation on/off
lambda flag	1/0	Wall loss on/off
PH_2SO_4peak	double $[/cm^3/s]$	Start sulfuric acid production term
nH_2SO_4	double $[/cm^3]$	Start sulfuric acid concentration
s	double $[/cm^3/s]$	Cluster production term
nouts	integer [#]	# of outputs
destime	double $[hours]$	Desired run time
ncluster	integer [#]	# to define cluster size
tstart	double $[s]$	Start time
ts H_2SO_4	double $[s]$	Start time for sulfuric acid production
te H_2SO_4	double $[s]$	End time for sulfuric acid production
cunit	integer [#]	Cluster number for initial concentration
ini conc	double $[/cm^3]$	Initial concentration
lambda t gas	double $[min]$	Time constant in wall loss for gas
lambda t par	double $[min]$	Time constant in Wall loss for gas

Table 5.1: Input parameters

In Svensmark et al. (2007) a value of $s_0 = 2.4 * 10^{-4} \pm 0.4 * 10^{-4}$ was derived. Now eq. (5.13) can be used to set boundaries for the nucleation rate s and will be used throughout this chapter. However, this is only used as a guideline since each set up may have different values of s_0 and the square root dependency determined in (Svensmark et al., 2007) is related with many uncertainties.

5.1.5 Sulfuric Acid Concentration

In each time step the sulfuric acid concentration is found by solving the following rate equation:

$$\frac{dH_2SO_4}{dt} = P_{H_2SO_4} - \lambda_{gas}[H_2SO_4] - [H_2SO_4]\sum_i n_i * k_i^c \tag{5.14}$$

The first term $P_{H_2SO_4}$ is the production term of sulfuric acid in cm^3/s and the second term is a loss term used to account for losses of gas molecules to the wall or other sinks. The last term is a loss of gas molecules to the condensing particles.

5.1.6 Program Input

Table 5.1 lists an example of the most important input parameters to the program.

Note that the initial concentration of stable cluster is placed in the bin *cunit*. Temperature as well as relative humidity are hard coded in the program and set according to the actual case considered. Most often a temperature of 30 degrees °C

5.1.7 The Integration Routine

The integration routine is an adaptive Adams-Bashford-Moulton method of variable order developed by Craig B. Markwardt (NASA/GSFC Code 662) and is used to integrate 3.1 through the desired timestep. A loop is created in the program where the incremental time step for each integration is determined from the desired number of outputs and the desired run time. In each incremental step dt the line :

DDEABM, 'cluster diff', tstart, n, tend, status= status

calls the integration routine and performs an integration of $'clusterdiff' =$ eq. 5.2 from $tstart$ to $tstart + dt$. The keyword status makes sure that integration has converged and is used as an error control in the program.

5.2 Model of Aerosol Growth in a Large Atmospheric Chamber

The idea behind this work was to investigate what future research could be conducted in larger atmospheric chambers. This could for example be a chamber like the atmospheric chamber AIDA chamber in Karslruhe (http://imk-aida.fzk.de/facility/aidatech.html). This chamber is an 84 m^3 large atmospheric chamber based in Karlsruhe and used for various atmospheric research purposes. Using the particle growth model described in the previous section this section illustrates how large atmospheric chambers can be used to probe sulfuric acid particle growth under atmospheric conditions.

Cosmic rays are speculated to affect the initial nucleation rate of sulfuric acid particles in the atmosphere. The main idea of this model run is hence to vary the cluster production term s and see how this affect particle creation and thereby limit the parameters needed for a real experiment. The run is set to last 24 hours which under the right conditions will provide enough time for the particles to grow since the half life wrt. the walls of an AIDA size chamber is as high as 24 hours (approximate information provided by Henrik Svensmark from a visit to the chamber).

It is interesting to simulate the sulfuric acid production profile initiated by the photochemical reactions during daylight that begins at 6 am, peaks around midday and ends at sunset around 6 pm. In the program we model this production profile with a sinusoidal function that peaks with the production rate P H_2SO_4 peak.

5.2.1 Input

The program is run with 30 equidistant s-values from $[0.03, 1]/s/cm^3$ and 9 equidistant values from $[2, 10]/s/cm^3$. According to eq. 5.13 this corresponds to an ion concentration of 150-15000 cm^3 which could be created experimentally with an ion source (in (Enghoff and Svensmark, 2008) 3700 ion pairs $/cm^3$ were created with a 35 MBq CS-137 source) .

For 12 hours (43200s) the production is following the sinusoidal profile peaking at $10000/cm^3/s$ as illustrated in the left plot of figure 5.1. The desired run time is $destime = 24h$ which determines the incremental time for the 100 output points ($nouts$) as $dt = 4h * 3600s/h/100 = 144s$. The wall and particle losses are set to 1 day (in minutes) which defines the loss constant as $\lambda_{par} = \ln 2/(\lambda_{par-t} * 60)$.

5.2.2 Discussion of Outputs

Figure 5.1 gives the temporal evolution of the production of sulfuric acid ($P_{H_2SO_4}$) and the changes in the concentration of sulfuric acid gas with the 3 different peak $P_{H_2SO_4}$. For all three peak production rates the sulfuric acid concentration peaks for the lowest s value. This is of course due to the last term in 5.15 which accounts for losses of sulfuric acid gas to the particles. Increasing the particle production rate will cause more sulfuric acid gas losses to the particles. In the left picture where the peak production rate is the fairly low 1000 $/s/cm^3$ the build up of sulfuric acid is relatively slow. Increasing the production rate causes a shift of the peak to the right.

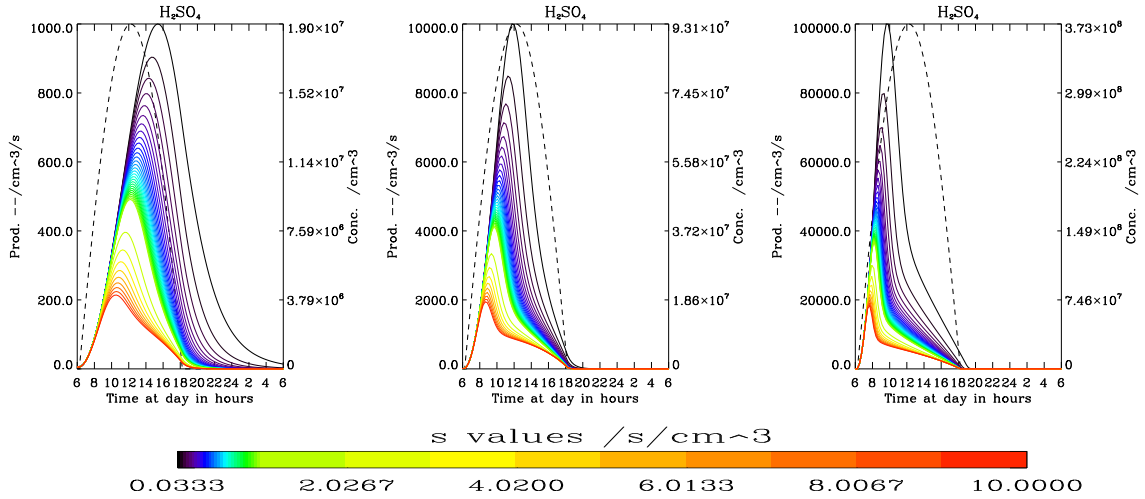

Figure 5.1: Sulfuric acid concentration as a function of s and time. left: $P_{H_2SO_4}$ Peak production of 1000 $/s/cm^3$ mid: $P_{H_2SO_4}$ Peak production of 10000 $/s/cm^3$ right: $P_{H_2SO_4}$ Peak production of 100000 $/s/cm^3$. See text for discussion

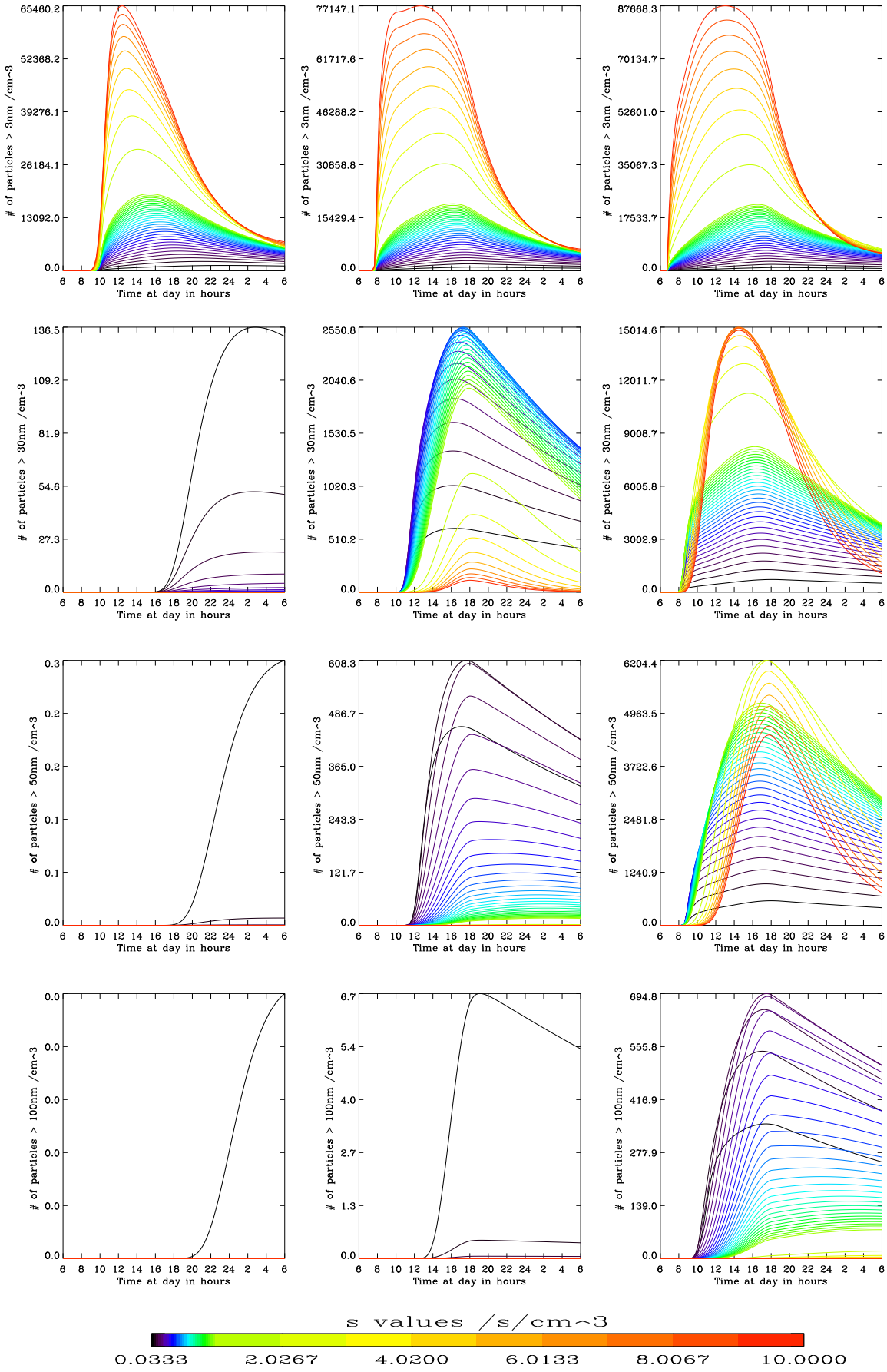

Figure 5.2: Large chamber aerosol growth for 3 production rates and various sizes as a function of s. left : $P_{H_2SO_4}$ Peak production of 1000 $/s/cm^3$ mid : $P_{H_2SO_4}$ Peak production of 10000 $/s/cm^3$ right : $P_{H_2SO_4}$ Peak production of 100000 $/s/cm^3$. See text for discussion

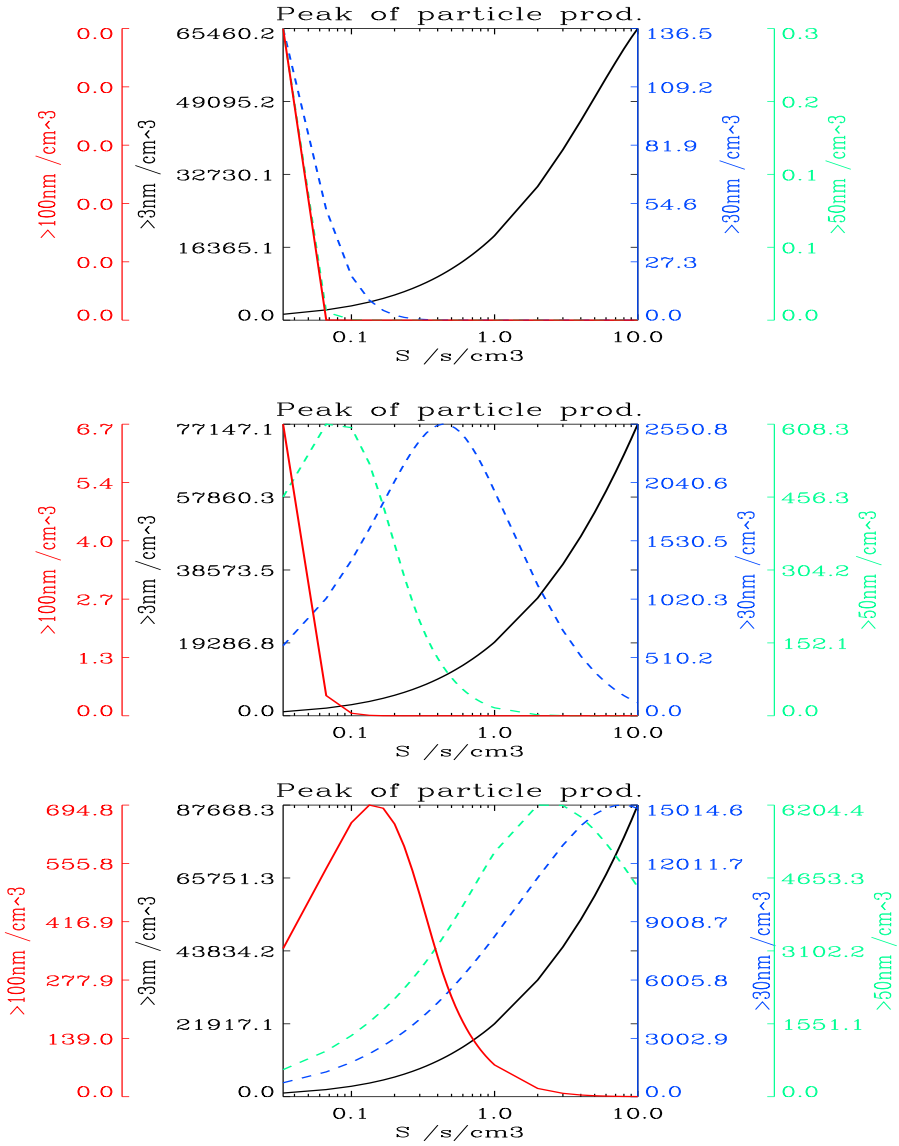

Figure 5.3: Peak of particle production. top: $P_{H_2SO_4}$ production of 1000 $/s/cm^3$ mid: $P_{H_2SO_4}$ Peak production of 10000 $/s/cm^3$ bottom: $P_{H_2SO_4}$ Peak concentration of 100000 $/s/cm^3$. See text for discussion

Figure 5.2 gives the temporal evolution of the formation of particles greater than 3, 30,50 and 100nm particles as a function of s and the 3 different peak $P_{H_2SO_4}$. The left, middle and right columns represent a peak $P_{H_2SO_4}$ of 1000, 10000 and 100000 $/s/cm^3$, respectively. The temporal evolution is obtained by solving equation 5.2 and 5.14. These equations describes the creation of sulfuric acid gas and how stable nucleated particles grow by condensation or coagulation. The optimal growth of particles is a balance of having sufficient nucleation rates and sufficient gas to enhance condensation. For instance if the nucleation rates become too high the particles will not grow very large since there will be very little sulfuric acid for each particle: the Twomey effect. The whole growth process is a nonlinear process and the results are therefore more or less difficult to foresee or project except for obvious features.

Figure 5.2 shows that the formation of 3 nm particles always occur for the highest s-value and maintains more or less the same shape for all three peak $P_{H_2SO_4}$. Increasing the peak

$P_{H_2SO_4}$ will lead to the formation of more particles $> 3nm$. The peak of the particle production is more or less midday for all three peak $P_{H_2SO_4}$. This picture changes for the particles $> 30nm$. Here the lowest $P_{H_2SO_4}$ peak value will only lead to particle creation over 30 nm for s values less than approx 0.3. For the middle $P_{H_2SO_4}$ peak value a s-value of approx 0.5 will lead to the creation of most particles above 30 nm. For the highest $P_{H_2SO_4}$ peak value an s-value of approx 9 will lead to the creation of most particles. The peak of the particle creation also occurs at different times depending on the s-values.

Very few particles are created above 50nm and 100nm for the smallest $P_{H_2SO_4}$ peak value. However both for the middle and high $P_{H_2SO_4}$ value numerous particles are created above 50nm and 100nm. This has to do with the high sulfuric acid gas concentration which enables more gas phase condensation onto the particles. CCN size particles are thus expected for these concentrations which are similar to atmospheric concentrations.

Figure 5.3 summarizes the findings of Figure 5.2 where the peaks of the particle productions are shown for the three different $P_{H_2SO_4}$ values.

5.2.3 Conclusions for Model of Aerosol Growth in a Large Atmospheric Chamber

For the present model sulfuric acid particle growth is shown to be sensitive to the sulfuric acid gas concentration and particle production rates. This also holds true for CCN size particles and therefore large variations in CCN size particle concentrations are expected if experiments similar to the ones presented here were to take place in a similar size chamber under atmospheric conditions.

5.3 Model of Aerosol Growth in a Small Atmospheric Chamber

In **Paper II** the role of ions in nucleating small sulfuric acid clusters as investigated in a laboratory in Svensmark et al. (2007) is repeated by using a different setup. The following is a summary of **Paper II** with a rewrite of the experimental setup and conclusions and using parts directly written by me (the parts in **Paper II** from beginning of section 3 page 2 to the end of page 3).

5.3.1 Experimental setup, model and results

In the experimental setup a cylindrical chamber of 50 L (length 100 cm and diameter 25 cm) with a UV source coupled to the one end was used to probe aerosol formation under ion intensities ranging from 770 ion pairs/cm3 (background) to 3700 ion pairs/cm3 (created by using a 35 MBq Cs-137 radioactive source). The chamber contained a mixture of ozone, SO2, and water vapor and atmospheric air. Two measurement series were done:

- Series A: $\sim$ 4 ppb SO_2 and $\sim$ 23 ppb O_3 with 11 min of UV and 110 min between each measurement
- Series B: $\sim$ 30 ppb SO_2 and $\sim$ 68 ppb O_3 with 4 min of exposure to UV at 10 times lower intensity than in the first series and 90 min between each measurement

The precise experimental details is given in **Paper II**. Figure 5.4 presents the experimental results of Series A and B. Here it seen how an increase in ion production increases the

overall aerosol concentration by a factor of approx 3. To model the results of Figure 5.4

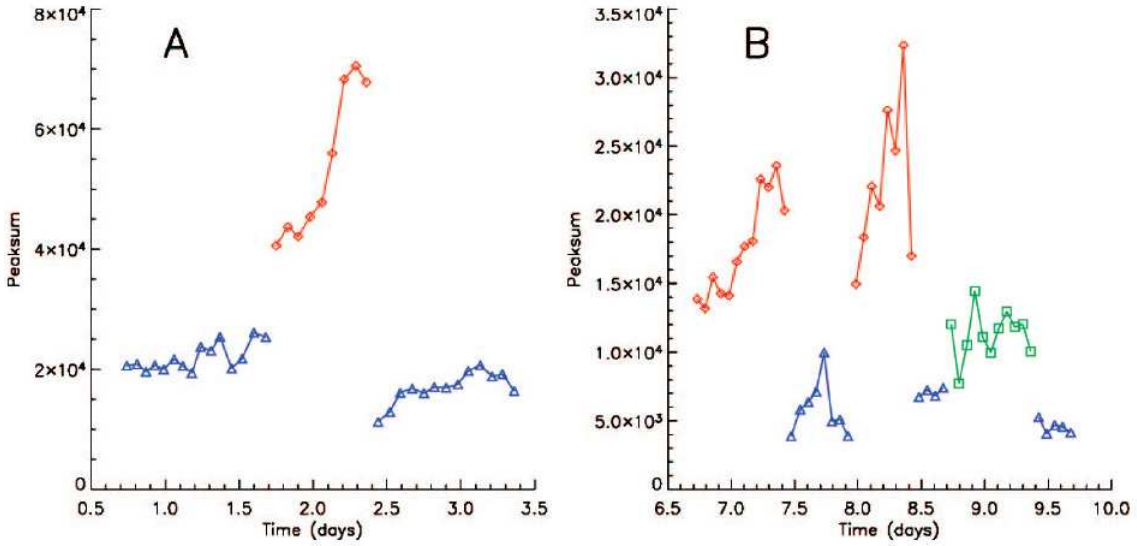

Figure 5.4: Results from the two measurements series in the integrated peak is shown as a function of time. Blue triangles correspond to measurements without the gamma source (ion production $\sim 3.7cm^{-3}s^{-1}$), red diamonds are with the source open (ion production $\sim 35cm-3s-1$), and green squares are with 1 cm of lead in front of the source (intermediate ion production). RH was $\sim$ 50% and $T \sim 23C$ for both series. (A) $\sim$ 4 ppb SO2 and $\sim$ 23 ppb O3 with 11 min of UV and 110 min between each measurement. (B) $\sim$ 30 ppb SO_2 and $\sim$ 68 ppb O_3 with 4 min of exposure to UV at 10 times lower intensity than in the first series and 90 min between each measurement.Figure by Martin Enghoff. From Paper II.

the aerosol growth model has been configured to initially run with a constant stable-cluster production s. This ensures that steady state conditions are obtained before turning on the sulfuric gas production $P_{H_2SO_4}$. The experimental data in Series I and II are then modeled by turning on the production rate of sulfuric acid $P_{H_2SO_4}$ (for 11 and 4 min, respectively). An example is shown in Figure 5.5, where the the model curve has been fitted to the experimental data for a set value of s and $P_{H_2SO_4}$.

The values of $P_{H_2SO_4}$ will lead to different sulfuric acid gas concentrations. By running the model it was observed that the sulfuric acid gas concentration is independent of s for the range of values used. This means that the peak sulfuric acid concentration obtained for a particular production rate is also independent of s.

The sulfuric acid and particle losses (to walls and dilution) are set to 3.26 min for Series I and 2.71 min for Series II (determined experimentally from the decay of the aerosol peaks). The relative humidity was fixed at 50 % for both series.

The output of each model run is a time series of the particle population adjusted for the counting efficiency of the particle counter. Unique values, comparable with the experimental results, are obtained for each set of parameters by integrating the peaks over time.

For series I the model was run with equidistant $ds = 0.05$ cm^{-3}s^{-1} with $s = [0.05, 7.35]$ cm^{-3}s^{-1} and equidistant $dP_{H_2SO_4} = 45000$ cm^{-3}s^{-1} with $P_{H_2SO_4} = [6.5 * 10^4, 2 * 10^6]$ cm^{-3}s^{-1}. For Series II $ds = 0.05$ cm^{-3}s^{-1} with $s = [0.05, 5]$ cm^{-3}s^{-1} and $dP_{H_2SO_4} = 90000$ cm^{-3}s^{-1} with $P_{H_2SO_4} = [4 * 10^4, 4 * 10^6]$ cm^{-3}s^{-1}.

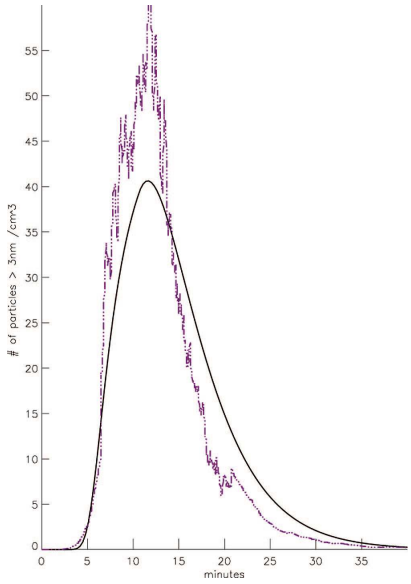

Figure 5.5: Fit of model to an experimental run. By choosing a set value of s and $P_{H_2SO_4}$ it is possible to model the experimental results. From **Paper II**.

Figure 5.6 shows these values for the two Series I (left) and II (right).

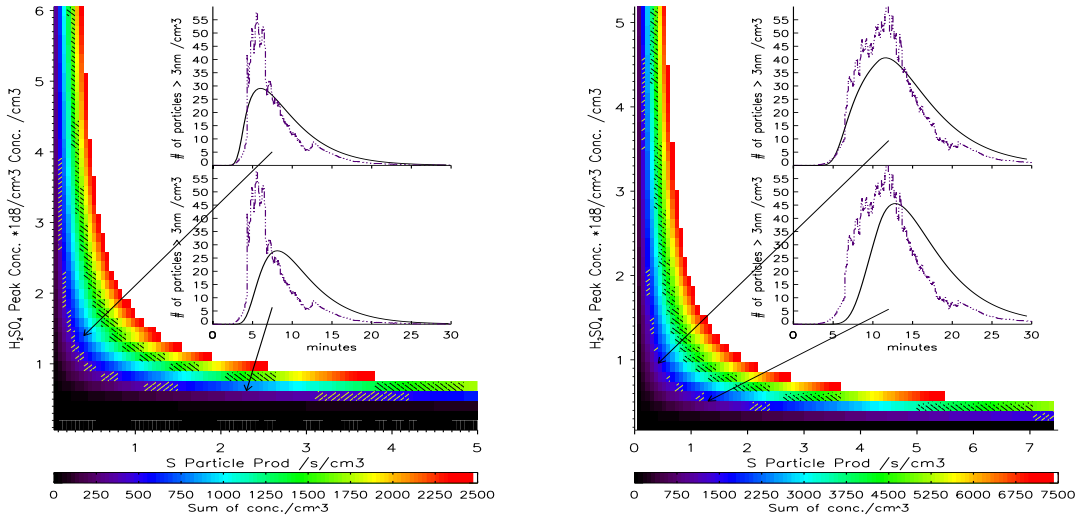

Figure 5.6: Integrated value of the temporal evolution of the formation of aerosols adjusted for the counting effiency of the particle counter as a function of s and sulfuric acid concentration. Left: Series I. Right: Series II. Hatched with / are the experimental data without sources and hatched with \ are the experimental data with fully open sources. The experimental data used in this figure are obtained by computing the average of the values in figure 2 with and without sources and including the 95% confidence interval. The inserts shows model results compared to experimental data for selected values of s and peak sulfuric acid gas concentrations. From **Paper II**.

The inserts in Figure 5.6 show model results compared to experimental data for selected values of s and peak sulfuric acid gas concentrations and thus show the effect on the experimental signal of changes in these two parameters. The model fits the experimental data in Series I rather well, whereas the actual shape of the model results in Series II differs more

from the shape of the experimentally obtained peaks. A more detailed model including evaporation might improve this. However, for the purpose of determining approximate values of particle and gas concentrations the model is sufficient.

5.3.2 Conclusions for Model of Aerosol Growth in a Small Atmospheric Chamber

The aerosol growth delay time compared to the UV time and the general shape of the model solution can be used to constrain the experimental values of s and the sulfuric acid concentration. Using this information for both series I and II the sulfuric acid concentration is constrained to the range of $C_{H_2SO_4} \approx [0.5 - 2.5] * 10^8 cm^{-3}$ which is below the homogeneous nucleation domain (Seinfeld, 2006, p. 523, fig 11.11).

For both series, the model estimates an increase in stable cluster production by a factor of ~ 3 to explain the difference between full and no exposure to the gamma source. This factor of 3, from no to full exposure, is the same order of magnitude as the factor of 4.78 found in Svensmark et al. (2007). In the small atmospheric chamber the ion production rate increases by a factor of 10 (from ~ 4 to ~ 40 cm^{-3} s^{-1}). Referring to 5.13 and using an ion concentration of (770-3700) ion pairs $/cm^3$ for this chamber, s should go from 0.19 $cm^{-3}s^{-1}$ without exposure to the source to 0.89 $cm^{-3}s^{-1}$ with full exposure. These limits are within those shown in Figure 5.6.

The results reconfirm the findings of (Svensmark et al., 2007) that ions do play a role in a chamber having similar conditions to that of the atmosphere.

5.4 Model of Aerosol Growth in a Marine Environment During a FD

This section is aiming to model the observational changes of the AERONET aerosol Angstrom exponent during a FD as presented in chapter 4. The idea is to use the size distribution from an aerosol growth model to calculate the aerosol optical thickness and Angstrom exponent, for the wavelength pairs 350, 450 nm and 550, 900 nm. This is done by a combination of methods using a Mie scattering code and an optical properties program. A FD is modeled by altering the nucleation rate over time so that it follows an ionization profile from a Forbush decrease.

The work in this section is presented in **Paper III** and the following is meant to be a summary of this paper. For details I refer to **Paper III**. Most subsections are excerpts directly taken from **Paper III** fitted into the thesis to ensure continuity. [1]

5.4.1 Theoretical model

To investigate the changes in the optical properties of a cloud-free marine environment consisting of sulphur gases and sea salt during a Forbush decrease an approach is taken based on 4 steps:

- **Aerosol growth model**: Neutral sulphuric acid aerosol growth is simulated in a marine environment where the cluster production is modulated during a FD. In this part

[1] Section 5.4.1 through 5.4.6, 5.4.9 and 5.4.10 are written by me. Section 5.4.7 and 5.4.8 by Martin Enghoff and I.

three parameters are varied: the gas phase sulphuric acid production rate, the particle loss rate, and the production rate of stable sulphuric acid clusters.

- **Miex part**: The particle distribution as a function of time is input to a Mie Scattering program (Miex), along with the relevant refractive indices, and used to calculate the extinction coefficients and optical depths.

- **OPAC part**: Simultaneously, an optical properties program (OPAC) is used to calculate the optical depth of a fixed sea salt distribution representative for the marine troposphere.

- **Optical properties**: Finally, the total optical depth and Angstrom exponent is calculated as a function of time for the combined sea salt distribution and sulphuric acid particles.

5.4.2 The Aerosol Growth Model

The numerical model is based on the model of section 5.1.1 but with a bin size increase factor of 1.1 per bin see eq. 5.1. Stable particle formation by nucleation are assumed to be 5 molecules big and are thus placed in bin 5 with a cluster formation rate s.

The rate of change of the sulphuric acid concentration is solved by the following equation :

$$\frac{dH_2SO_4}{dt} = P_{H_2SO_4} - [H_2SO_4] \sum_i n_i \cdot k_i^c \tag{5.15}$$

Here, the first term, $P_{H_2SO_4}$, is the production of gaseous sulphuric acid and the second term the gas losses to the aerosols by condensation. Compared with eq. 5.14 in the present setup there are no wall losses. Instead losses to primary particles are included in the condensation equations.

5.4.3 Miex part

Miex is a Mie Scattering program originally developed to model interstellar dust scattering (Wolf, 2006). However, the code works equally well on an ensemble of aerosol particles over a large wavelength range providing that the size distribution of the aerosols and their refractive index is known. We have modified the code to calculate the extinction coefficient σ_{ext} from an ensemble of wet sulphuric acid particles (SAP) with relative humidity 0.5 and with a size distribution given by the aerosol growth model. The database of index of refraction for sulphuric acid particles as a function of wavelength is given by Hess et al. (1998).

Assuming that the concentration of sulphuric acid particles is exponentially decaying with height (h) in the troposphere (extending from 0-10 km) the optical thickness for wavelength λ can now be calculated from the extinction coefficient:

$$\tau_{SAP}(\lambda) = \sigma_{ext}(\lambda) N_{SAP} \int_0^{10} \exp^{\frac{-h}{Z}} dh, \tag{5.16}$$

where Z is the scale height and N_{SAP} is the concentration of sulphuric acid particles calculated by the aerosol model.

5.4.4 OPAC part

OPAC is software tool designed to calculate optical properties for various atmospheric scenarios including changing cloud cover and aerosol distributions (Hess et al., 1998). The sizes and width of aerosol distributions are changed according to their log-normal distributions. Here, the program is used to calculate extinction coefficients and optical thicknesses τ_{SS} for a clean atmosphere with only a marine boundary layer of sea salt particles. The sea salt distribution remains constant throughout each individual run and only serves as a background. The distribution of sea salt particles has both a coarse and accumulation mode given by:

$$\frac{dN(r)}{dr} = \frac{N}{\sqrt{2\pi}r \log\sigma \ln 10} \exp\left[-0.5(\frac{\log r - \log r_{mod}}{\log\sigma})^2\right], \tag{5.17}$$

where $\sigma(\text{coarse/accu}) = [2.03/2.03]$ and $r_{mod}(\text{coarse/accu})$ =[1.75/0.209] μm and Ncoarse/accu = $[3.2 \cdot 10^{-3}, 20]$ cm^{-3}, respectively. These two modes are assumed to be generated by a wind speed of 8.9 m/s (Hess et al., 1998). As will be described later, the contribution from sea salt is varied by systematically changing the concentration of the accumulation and coarse mode.

5.4.5 Optical properties

The time dependent optical thickness for the sulphuric acid particles at different wavelengths is added to the constant optical depth from sea salt and the Angstrom exponent between two wavelengths is calculated as the slope of $\log(\tau)$ vs $\log\log(\lambda)$ for the two wavelengths:

$$\alpha(\lambda_1, \lambda_2, t) = -\log\frac{\tau(\lambda_1, t)}{\tau(\lambda_2, t)} \Big/ \log\frac{\lambda_1}{\lambda_2}, \tag{5.18}$$

where $\tau(\lambda, t) = \tau_{SAP}(t) + \tau_{SS}$. In this study we focus on the wavelengths λ= 350 and 450 nm. These wavelengths detect CCN size particles and can be compared to the Angstrom exponents as measured by AERONET (Holben et al., 1998). Furthermore the wavelength pair 550 and 900 nm is used to compare with observations from MODIS (Platnick et al., 2003).

5.4.6 Running the model

To establish a steady state of background sulphuric acid particles, initially, the sulphuric acid model is run for a month for various constant cluster formation rates (s), constant sulphuric acid production rates ($P_{H_2SO_4}$), and half lives (κ) of nucleated particles against primary particles. These runs provide steady state solutions for the aerosol distribution in a parameter space containing values of $s_0 = [0.0001, 0.0005, 0.001, 0.005, 0.01]$ cm^{-3}s^{-1}, $P_{H_2SO_4} = [1 \cdot 10^3, 5 \cdot 10^3, 1 \cdot 10^4, 2 \cdot 10^4]$ cm^{-3}s^{-1}, and $\kappa = [0.5, 1, 1.5, 2, 1000]$days. The loss values κ represent the time scale losses of sulphuric acid particles to sea salt and other primary particles (see **Paper III** for details on this). The production values of sulphuric acid were chosen such that the sulphuric acid gas concentration reached peak values of about $1 \cdot 10^7$cm^{-3} comparable to the values of Kazil et al. (2006) and Weber et al. (2001). Note that this may be at the high end of the sulfuric acid concentration range. The steady state stable cluster production s_0 is more uncertain. The span of values (two orders of magnitude) represents this uncertainty and is within the range mentioned in Pierce and Adams (2007) and Weber et al. (2001). Using 5.13 this corresponds to ion concentrations of 0.5 to 50 ion pairs $/cm^3$, which is a realistic albeit slightly high range.

The cluster production rate s is modulated by a Forbush decrease. At $t = 0$ the Forbush

decrease is turned on and the aerosol growth is changed over a period of 36 days with a FD minimum after 15 days. The Forbush decrease profile change in ionization *dQ(t)* is created by a mean of five major Forbush decreases (31. October 2003, 13. September 2005, 13. June 1991, 19. January 2005, 15. March 1989) from the Climax Neutron monitor including 15 days before and 20 days after the minimum. This gives a profile, F(t), with a 15% FD decrease minimum (the dotted line in Fig. 5.7). To create the corresponding relative change in ionization *dQ(t)* it is assumed that a major Forbush decrease is on the same scale as variations in ionization over the solar cycle, ie. $\approx$ 10% (Usoskin et al., 2004) and $F(t)$ is scaled such that the base level is at zero and the minimum is at 10%:

$$dQ(t)(t) = (1. + 0.1 \cdot \frac{F(t) - F(0)}{max(F(t)) - min(F(t))}) \tag{5.19}$$

Using 5.13 it is possible to determine the temporal evolution of the cluster production during the FD $s(t)$ by multiplying the steady state value s_0 with the functional form $\sqrt{dQ(t)}$.

$$s(t) = s_0\sqrt{dQ(t)} \tag{5.20}$$

5.4.7 Results for Model of Aerosol Growth in a Marine Environment During a FD

In Fig. 5.7 the upper plot is the output from a single run with $\kappa = 1.5$ days, $P_{H_2SO_4} = 20000$ $cm^{-3}s^{-1}$, $s = 0.001$ $cm^{-3}s^{-1}$ and shows the Angstrom exponent (black line) as a function of the 36 days representing the FD (black dashed). The effective radius (red) as well as the number of H_2SO_4 particles: N_{total} (blue solid), $N > 3$ nm (blue dashed) and $N > 100$nm (blue point-dashed) is also shown. The two lower plots gives the optical depths at λ=350 and 450 nm used to calculate the upper plot.

For this choice of parameters it is observed how the Angstrom exponent decreases by $\approx$ 2% to a minimum approximately 3 days after the FD minimum. The explanation is that at the onset of the FD the cluster production, s, and hence the number of small particles decreases. Since the loss rate remains constant this causes the total particle number to decrease and a subsequent minimum in τ_{350} is observed around the time of the FD minimum. A couple of days after the FD minimum the optical depth for $\lambda = 350$ nm returns to its initial value. Note that this happens several days before the particle number returns to its original value. The reason being that as the number of particles go down, the remaining ones increase in size, due to reduced competition for the sulphuric acid. As the particle radius increases, so does the optical thickness. The same pattern is observed for $\lambda = 450$ nm, however the optical depth increases above its original value, before it relaxes back. This is due to a higher sensitivity to the particle radius, since this wavelength is further away from the effective radius of the particle population (174 nm). The difference in behaviour for the optical thickness at the two wavelengths show the complex dependence of the AOT on particle number and radius. Furthermore this is the reason for the observed lag of 3 days in the dip of the AE compared to the dip in the FD. An obvious interpretation of this lag would be to attribute it to the time it takes from the decrease in production of small particles to propagate up to sizes detectable at the employed wavelengths. Our analysis, however, shows that this is not the only possible explanation, but that the increase in radius of the remaining population must also be considered.

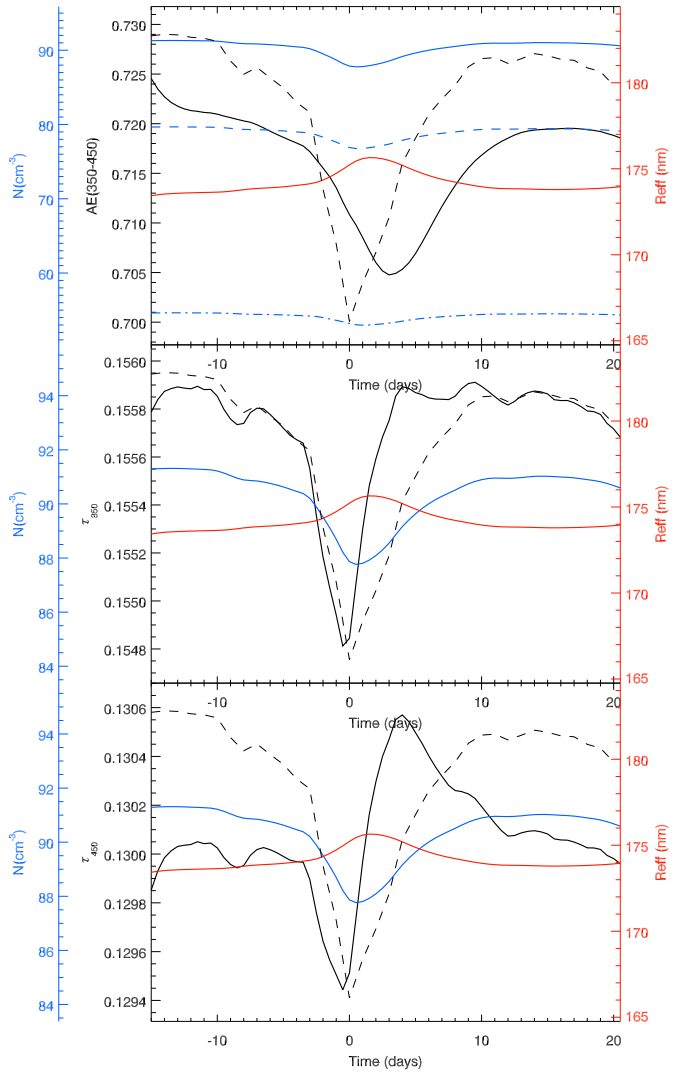

Figure 5.7: The upper plot is model output from a single run with $\kappa = 1.5$ days, $p = 20000$ cm^{-3}s^{-1}, $s = 0.001$ cm^{-3}s^{-1} and shows the Angstrom exponent (black line) over 36 days for the FD (black dashed). The effective radius (red) and the number of H_2SO_4 particles: N_{total} (blue solid), $N > 3$ nm (blue dashed) and $N > 100$nm (blue point-dashed) are also shown. The two lower plots show the optical depths at λ=350 nm and 450 nm. From **Paper III**.

In Fig. 5.8 the whole parameter space is explored. Each box represents a value of s and $P_{H_2SO_4}$. In each box the colors represent the loss values of $\kappa = 0.5, 1, 1.5, 2, 1000$ days increasing from a value of 0.5 days (bottom) to 1000 days (top). For each loss value the first number gives the base level of the Angstrom exponent defined as the mean of the first 10 days of Angstrom exponent output (t=-15 to -5 in Fig. 5.8). The second number is then the per mille deviation of the largest extremum of day -5-20 from the base level, with positive numbers meaning an increase in AE and vice versa. The two following numbers are the mean of the 10 first days of the effective radius in nm and sulphuric acid concentration in cm^{-3} (divided by 10^7), respectively.

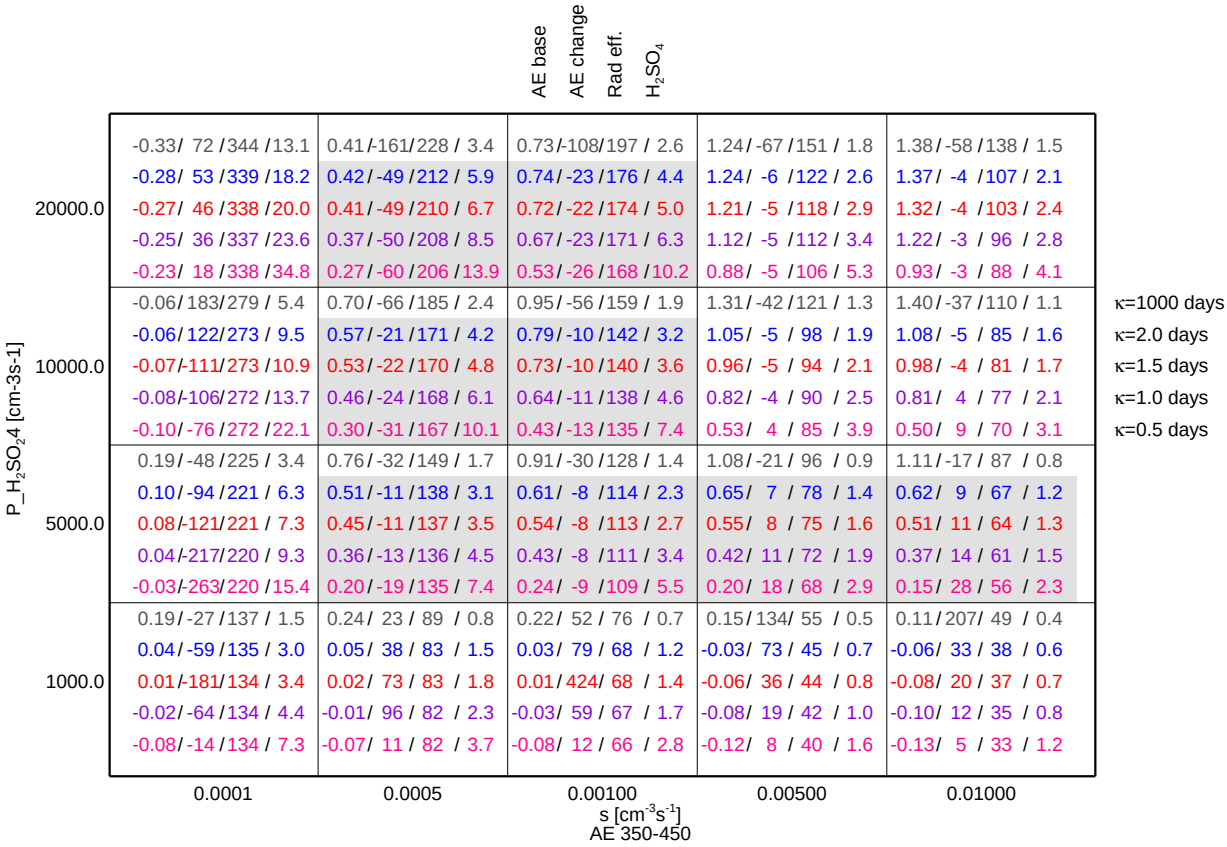

Figure 5.8: Model overview of the sensitivity study of various optical parameters and sulphuric acid concentrations as function of loss rates, sulfuric acid production rates and cluster production rates. Each box represents a value of s and $P_{H_2SO_4}$. In each box the colors represent the loss values of $\kappa = 0.5, 1, 1.5, 2, 1000$ days increasing from a value of 0.5 days (bottom) to 1000 days (top). For each loss value the first number gives the base level of the Angstrom exponent defined as the mean of the first 10 days of Angstrom exponent output (t=-15 to -5 days). The second number is the per mille deviation of the largest extremum of days -5 to 20 from the base level. Positive numbers mean an increase in AE and vice versa. The two following numbers are the mean of the 10 first days of the effective radius in nm and sulphuric acid concentration in cm^{-3} (divided by 10^7), respectively. From **Paper III**.

Three types of responses are behind the different percentage responses. The standard case is where a small dip appears in the Angstrom exponent. However, in a few cases the choice of input parameters gives a peak in the Angstrom exponent indicating that a decrease in small particle population may also lead to increases in AE. This happens when the effective radius gets below a certain point around 80 nm (depending somewhat on s and $P_{H_2SO_4}$), far away from the probing wavelengths of 350 and 450 nm. A switch in sensitivity then seems to happen causing the low wavelength to be more sensitive to the change in effective radius than the high wavelength, as opposed to what was seen in the case of the single run in Figure 5.7. Since the AOT at 350 nm then increases the most as the radius of the particle population grows, this causes an increase in the AE. The third response is the case where no mixing occurs ($\kappa = 1000$ days). Here very large changes in the AE is typically observed. These rather large percentage changes are more a result of an unstable initial precondition run than a real decrease in Angstrom exponent caused by the modulation of cluster production. When there is no loss for the particles, steady state is never reached and therefore the effective radius continues to grow, causing a decrease of the AE, throughout these runs. Since the AE is then much lower after the FD, simply because of this overall growth of the population, artificially high changes appear. The runs with $\kappa = 1000$ days should generally be regarded with care.

As can be observed, the baseline values vary from small negative numbers to a maximum around 1.4 in Angstrom exponent. In Sano (2004) the average Angstrom exponent over the ocean is about 0.5. In Kazil et al. (2006) and Weber et al. (2001) the sulphuric acid concentration over the oceans was found based on both modelling and measurements. Here values of sulphuric acid concentration in the lower troposphere over the ocean was about 10^7 cm^{-3}. If these values are compared with our results this can be used to restrict the solution space of sulphuric acid production and cluster production to the region 0.0005 cm^{-3}s^{-1} $\leq$ s $\leq$ 0.001 cm^{-3}s^{-1} and $P_{H_2SO_4} \geq 5000$ cm^{-3}s^{-1} and the region 0.005 cm^{-3}s^{-1} $\leq$ s $\leq$ 0.01 cm^{-3}s^{-1} with $P_{H_2SO_4} = 5000$ cm^{-3}s^{-1}. This region is shaded in grey in the figure and indicates the most probable optical response in the marine troposphere to Forbush decreases under the assumption of a square root dependency of the cluster formation rate to the ion production. As can be observed the expected average change in percentage of the Angstrom exponent is of the order of -6 to 3% in the shaded region, compared to the initial 10% modulation in ionization.

For more discussion of Fig. 5.8 see **Paper III**

5.4.8 Comparison with Observations

In Svensmark et al. (2009) an epoch analysis of AERONET data from 5 major FD events was made and presented in Chapter 4. Angstrom exponent data (340-440nm) from approximately 40 stations (stations with more than 20 measurements a day) were superposed and averaged over the 5 events (31. October 2003, 13. September 2005, 19. January 2005, 16. July 2000, 12. April 4 2001). In this section we compare those results with the model runs. Additionally we investigate the wavelength pair 550, 900 nm which can be compared with both AERONET and MODIS data.

The left of Figure 5.9 shows a comparison of Angstrom exponents for the short wavelength pair from the model (350, 450 nm) and from the average of the 5 FDs from AERONET (340, 440 nm). The right of Figure 5.9 shows the wavelength pairs AERONET (500, 870 nm), MODIS (550, 865 nm), and Model (550, 900 nm). The dashed line is the average of the FD

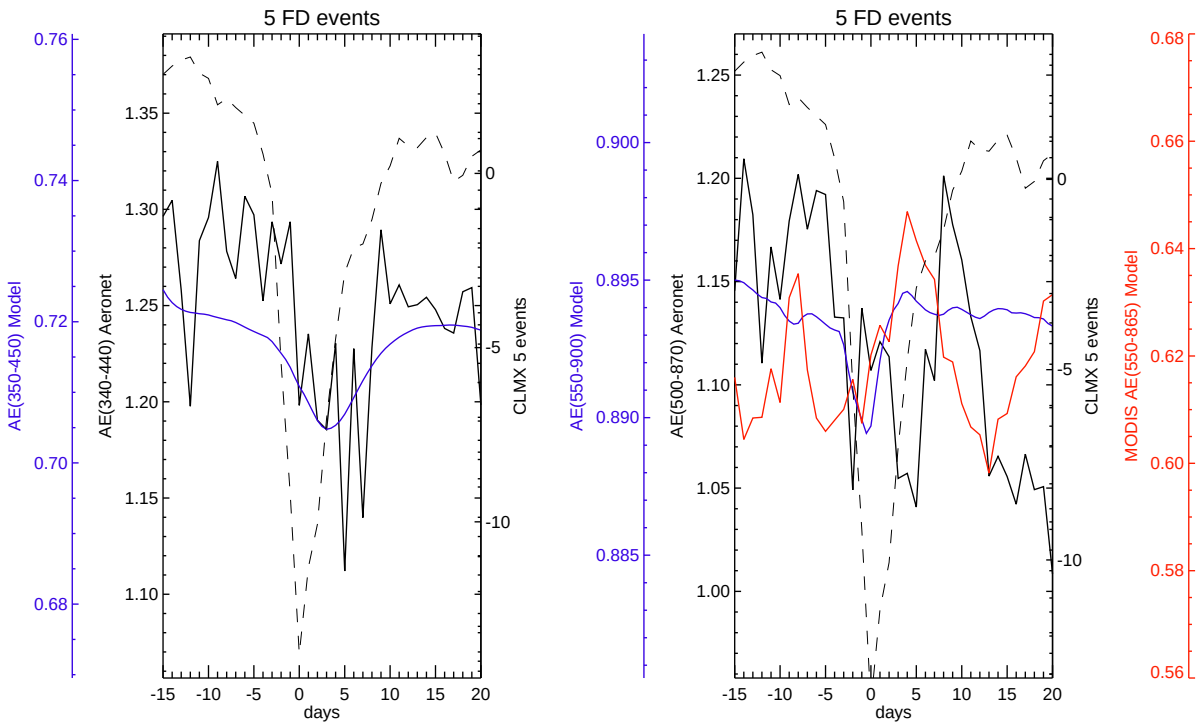

Figure 5.9: Angstrom exponents from model and observations (MODIS and AERONET) for short wavelength pairs and long wavelength pairs. The observations are based on an epoch analysis where the signal from 5 FD events are superposed and averaged for each day. From **Paper III**.

signal over the events listed above.[2] First, it is observed that the values for AERONET are higher than the values for both the model and MODIS. This is because the land based AERONET stations have more small mode fraction particles due to aerosols from e.g. pollution, dust, and biomass burnings.

The left figure shows a slight significant signal for the short wavelength pair for AERONET where a decrease in the Angstrom exponent is observed a couple of days after the FD minimum for the 5 events. However, for the longer wavelength pairs in the right figure both for MODIS and AERONET no significant signal seem to be present. Since we are comparing an ocean based model with land based observations, no direct comparison can be made but we can however point to some trends. There is a systematic decrease of a factor of approximately 2-4 in signal for going from the small wavelength pair to the larger in our model. Assuming that the weak signal observed in Svensmark et al. (2009) is real then the signal from the long wavelength pairs could be lowered into the climatic noise of the Angstrom exponent observations. If a linear dependency of the cluster formation rate instead of a square root dependency is assumed this effect would even be more pronounced. This seems to be confirmed by the left of figure 5.9 although more observations would be needed to examine this in more detail. Therefore if an ion induced mechanism is working as in our model, it is expected that observations based on the shorter wavelength pair would be the most favourable for seeing the FD effect.

[2]Note that the FD events are not identical to the ones used in the model but that the average of the peak is more or less the same. For the purpose of this exercise this is more than adequate.

5.4.9 Additional results

In order not to reproduce the whole paper only the most important parts results have been included. But we also studied :

- Nucleation rate changes. Here it is shown that the decrease in Angstrom exponent depends on how the nucleation rate scales with ionization. In the standard case s is proportional to the ion concentration, but s could also be scaling as the square root of ion production as indicated in Svensmark et al. (2007). These two different schemes are examined and it is shown that the square root dependency diminishes the Angstrom exponent response with almost a factor of 2. Also, if the nucleation rate is assumed to be half dependent on ionization and half dependent on other nucleation mechanism (e.g. homogeneous nucleation) the Angstrom exponent change is similarly decreased with a factor 2.

- Sea salt changes. Here we changed the sea salt distribution by changing the relative content of sea salt particles in the accumulation mode and coarse mode. The strongest response in the AE comes from changes in the accumulation mode, which is to be expected since the median size of this mode (209 nm) is much closer to the wavelengths used to find the AE (350nm and 450 nm) compared with the coarse mode (1.75 μm). Changing the accumulation mode of sea salt by 50%in either direction shifts the baseline of the AE by about 20%. Similar changes in the coarse mode only yields very small changes in the AE

See **Paper III** for a more thorough analysis of this.

5.4.10 Conclusions for Model of Aerosol Growth in a Marine Environment During a FD

Under the assumption that ion induced nucleation play a role in the marine troposphere, a simple aerosol growth model in combination with a Mie scattering code and an optical properties program was used to model Angstrom exponents over the tropospheric ocean for two wavelength pairs (350, 450 nm and 550, 900 nm) during a Forbush decrease by modulating the nucleation rate over time by the ionization profile from the Forbush decrease. The marine environment was modeled by a fixed-in-time bimodal sea salt distribution and a variable sulphuric acid aerosol distribution. A large parameter space was explored by altering nucleation mode cluster production rates, sulphuric acid production, loss rates, as well as exploring alternative nucleation mechanism. Distinct but highly varying responses in the optical properties were found by changing the initial 5 parameter settings. For the short wavelength pair (350, 450 nm) changes in the Angstrom exponent of about -6 to 3% was found for realistic settings of the Angstrom exponent base level values and sulfuric acid concentration as compared to the marine troposphere. For the longer wavelength pair (550, 900 nm) the changes were generally a factor of 2 to 4 lower. This seems to match with observations from AERONET and MODIS were an epoch analysis of 5 major FD event reveal a slight significant signal in the wavelength pair (340, 440 nm) and not in the longer wavelength pair (550, 900 nm). The study encourages more global observations of Angstrom exponents at smaller wavelength pairs and improving the signal to noise ratio further. This may help to improve the understanding of the importance of ion induced nucleation and of how secondary aerosol distributions affect the marine optical properties. Future work related to the model should focus on implementing a dynamic sea salt distribution and investigating other nucleation schemes and growth rates further.

5.5 Main Conclusion for the Aerosol Growth Model

An aerosol growth model was developed and used to probe aerosol formation in three different cases. Of most importance to this thesis was the third case reported in section 5.4 and in **Paper III**. Here the aerosol growth model was used to model the observational changes in the Angstrom exponent during a FD of $\sim$ 15% in Climax. By means of a Mie Scattering program and assumptions on primary sinks, particle growth, sulphuric acid production and nucleation rates, the optical response in Angstrom exponents to a FD was explored for a large parameter space. It was found that the Angstrom exponent for the short wavelength pair AE(350, 450 nm) changes of about -6 to 3% for sulfuric acid concentrations similar to the marine atmosphere during a FD. For the longer wavelength pair AE(550, 900 nm) the changes were a factor of 2 to 4 lower. These results can to some extent explain the observations reported in Figure 4.4, 4.7 and 5.9.

Chapter 6

Discussion and Future work

This chapter discusses some of the assumptions made in the different chapters and suggests ways of improving the work presented in the thesis.

6.0.1 Discussion of Ionization Model

The ionization model for FDs outlined in chapter 3 provided a way to list the ionization change during a FD relative to the Solar cycle changes in ionization. The calculation was done assuming a fixed atmosphere (US Standard Atmosphere) and assuming particles penetrating the magnetic field at a fixed geographical point. These assumptions was for our data analysis purpose correct since we needed a coarse listing of the ionization strength of the various FDs in the troposphere. An interesting study would be to calculate a global map of the cosmic ray induced ionization assuming the correct geomagnetic field and atmosphere for each grid point. This would allow for a more correct spatial correlation study correlating ionization changes with various parameters.

The time evolution of γ and A and their influence on the ordering of the list of FDs Table 3.3 is based on the minimum value of the FD. This is a good proxy for the size of the ionization induced changes under the FDs but some FDs occur over 8-10 hours and some occur over a couple of days. A different and maybe more precise indicator could maybe be obtained by calculating the integrated value of the ionization change caused by the FD over the duration of decrease.

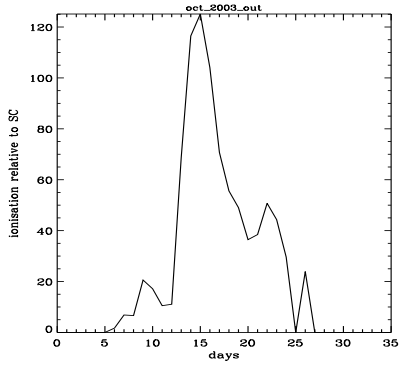

Figure 6.1: FD response for Halloween 2003 event over time. Evolution of A, γ over time for the October 2003 Halloween event. Own work.

To do this A, γ should be determined in each time step as is done in 6.1. For each time

step a ionization value can now be calculated. The integral of all this would represent the "true" ionization change in FD over time. By repeating this exercise for all 26 FD a different ordering of the FDs would be obtained. This might turn out to be a more precise indicator but it can course then be discussed on which day to start and end the integration. For practical and time consuming reasons this integral method has not been possible and table 3.3 is used instead. Future work could look into issues related to this.

6.0.2 Discussion of Data Results

The data analysis in chapter 4 was the first of its kind making a FD analysis of both cloud liquid water and aerosol data. The results indicated that cosmic rays induced a significant signal on short time scale in clouds and aerosols. This is among the first studies to indicate this. However, there are a number of studies that should be done in a natural extension to the work presented in chapter 4:

- Inclusion of other microphysical parameters. MODIS provides a number of geophysical parameters of interest to the field of aerosol formation, where the Effective radius and Cloud Optical Thickness should be analyzed similar to what was done with the cloud liquid water. As explained in **Paper III** the effective radius, Cloud Optical Thickness is suspected to increase/decrease, respectively under a FD. Similarly Ozone could also be checked to investigate if we observe Ozone changes during a FD, that could play a role in sulfuric acid formation. These parameters was partly studied in the regional case of Kristjánsson et al. (2008) but should be extended to global variations with the list of FDs compiled in this thesis.

- The studies on spatial correlation should be extended. It is vital for the understanding of the link between clouds and GCR where the process takes place. However, in order to do this better understanding of the spatial ionization profile should be reached. Simple point correlation map with GCR data from a single station no longer suffices, see also previous section.

- AERONET is an interesting database and many possible studies could be imagined. **Paper III** gave a better understanding of how Angstrom Exponents change during a FD. An extension of this study to investigate not only AERONET Angstrom exponents but also AOT (Aerosol Optical Thickness) values would be interesting.

- It could be useful to have information on the different sites to be able to distinguish AERONET sites coming from remote, biomass burning, marine or city areas. This would make an analysis of the data easier and make as spatial correlation map analysis much more interesting.

- The aerosol growth model results of section 5.4 encourages more global observations of Angstrom exponents at smaller wavelength pairs and improving the signal to noise ratio by further analysis of FD events in aerosol data.

- New cloud satellite data has become available. From the so called A-train, CloudSat returns high resolution cloud data. Flying in constellation with CALIPSO, that provides aerosol data with an altitudinal distribution, these 2 new satellites are interesting for this field and at some point should be studied. The problem with CALIPSO and CloudSat data is that the global revisit time due to the very focused footprint is large (over 10 days for both satellites) making global average studies difficult. Meteosat is another interesting data provider. It is a geostationary satellite with a Zenith point in West Africa that with a 15 min resolution returns quality cloud measurements. This high time resolution would be very relevant to FD studies.

See also Appendix C for some ideas on data analysis of FD that could be repeated using table 3.3.

6.0.3 Discussion of Model Results

The model results presented in chapter 5 and the work of **Paper II** and **Paper III** show that the production of CCN size particles and cloud optical properties is sensitive to changes in production rates and sulfuric acid gas concentration. The model has proved itself efficient to describe many features related to aerosol growth under certain constraints. However, the development of a model is always subject to improvement. A number of extensions to the model could improve the overall understanding of the link between aerosol formation and cosmic rays:

- The aerosol growth model includes neutral growth from stable clusters. A natural extension of this program would be to include evaporation of particles and ion-ion recombination. This would be a larger rewrite of the code and give a slower code since both charged as well as neutral growth must be calculated in each time step. Right now the relative humidity is hardwired to 50%. It would be an improvement to be able to run the model for several relative humidities which would require updating the growth rates due to the changes in the sulfuric acid water uptake.

- An idea to circumvent rewriting the code could be to implement other ion mediated nucleation schemes as described by Yu (2009). Here a table together with linear extrapolation method is used to calculate the number of sulfuric acid molecules in the critical cluster, the mole fraction (between H_2SO_4 and H_2O), and diameter of the critical cluster. The table is a function of ion production rates, relative humidity, sulfuric acid gas concentration and temperature. This extrapolation could with some modifications be inserted in our program. Yu's experience in modeling Ion mediated nucleation is larger than our's and is based among other things on thermodynamical experiments of rate constants. It would be an improvement over our model although part of our code would be a black box depending on Yu's model.

- In **Paper III** the primary emissions are examined using a constant contribution to the optical depth from sea salt. A more realistic model should focus on implementing a dynamic sea salt distribution to improve the representation of losses to primary sinks.

These are the suggested immediate improvements the aerosol code could benefit from. With time it is needed to study global scale simulations of the GCR-Aerosol-Cloud link similar to the work of Kazil et al. (2006); Pierce and Adams (2009). With a continuously increasing insight into the underlying nucleation mechanisms, global sulfuric acid concentrations and primary sinks new results may appear.

Chapter 7

Conclusion

The causal link between cosmic rays and clouds was suggested over 10 years ago now and has been the cause of numerous (often emotional) discussions and debate both in the media and in the science community. The reason for this heated debate has been manyfold but is largely due to a lack of understanding of the underlying mechanism combined with its potential large impact on climate. Though the discussion on cosmic rays and clouds still gives rise to heated discussion things have turned from not acknowledging the effect to acknowledging the causal effect but debating its size. Over the years the field of ion induced nucleation, despite reaching diverging conclusions, has been widely accepted as a serious branch of aerosol nucleation.

At this point, more work on ion induced nucleation mechanisms and aerosol growth to CCN sizes is needed before an actual parametrization of the GCR-Aerosol-Cloud link can be proposed and used for cloud modeling on global scales. Since the atmospheric sulphuric acid content and sea salt concentration are limiting factors for ion induced aerosol growth, it is also vital to improve evaluations of these parameters and needed to fully evaluate the effect of cosmic rays on Earth's climate.

The work presented in this thesis has reached a number of conclusions on the relationship between cosmic rays and aerosol formation on short time scales which can assist the scientific community in understanding the role and impact of cosmic rays on clouds. The most important of these conclusions are:

- A list of the ionization change in the troposphere of the strongest Forbush decreases as compared to the ionization change over the solar cycle was calculated. The list indicated that only a few events induce ionization changes comparable to the solar cycle with the October 2003 Halloween event being the strongest.
- Forbush decreases appear to have an effect on clouds and aerosols once the changes of the FD induced ionization reaches a size comparable with the cosmic ray induced ionization during a solar cycle. For the large events significant decreases in Angstrom exponent from AERONET aerosols approx 5 days after the FD minimum were observed on a global scale. Significant decreases in the cloud liquid water on a global scale were observed after approx 8 days after the FD minimum. This indicates that the FD induced decrease in ionization diminishes the aerosol nucleation rate and over time propagates to influence first CCN size aerosols and then clouds.
- A model was developed of the changes in aerosol optical properties in a marine environment during a FD using a neutral aerosol growth model in combination with a Mie Scattering code. The model assumes the creation of stable ion induced nucleated

clusters and has a fixed primary distribution of sea salt particles. A large parameter space was explored and for some parameters the results confirm the existence of decreases in Angstrom exponents during a FD.

These conclusions substantiates the causal mechanism between cosmic rays, aerosols and clouds. The effect seems to take place on a global scale on the timescale of aerosol formation and the largest Forbush decreases can induce changes in the cloud cover comparable to the changes reported in (Svensmark, 2000; Marsh and Svensmark, 2000b,a) over the 11 year solar cycle. Forbush decreases albeit the difficulties in analyzing the events have proved to be a good natural phenomena for the investigation of the GCR-Ion-Aerosol-Cloud link.

Bibliography

Arnold, F. (2006, August). Atmospheric Aerosol and Cloud Condensation Nuclei Formation: A Possible Influence of Cosmic Rays? *Space Science Reviews 125*, 169–186.

Bazilevskaya, G. A., I. G. Usoskin, E. O. Flückiger, R. G. Harrison, L. Desorgher, R. Bütikofer, M. B. Krainev, V. S. Makhmutov, Y. I. Stozhkov, A. K. Svirzhevskaya, N. S. Svirzhevsky, and G. A. Kovaltsov (2008, June). Cosmic Ray Induced Ion Production in the Atmosphere. *Space Science Reviews 137*, 149–173.

Berndt, T., O. Böge, F. Stratmann, J. Heintzenberg, and M. Kulmala (2005, February). Rapid Formation of Sulfuric Acid Particles at Near-Atmospheric Conditions. *Science 307*, 698–700.

Bieber, J. W., J. Clem, D. Desilets, P. Evenson, D. Lal, C. Lopate, and R. Pyle (2007, December). Long-term decline of South Pole neutron rates. *Journal of Geophysical Research (Space Physics) 112*, 12102–+.

Birmili, W., H. Berresheim, C. Plass-Dülmer, T. Elste, S. Gilge, A. Wiedensohler, and U. Uhrner (2003, April). The Hohenpeissenberg aerosol formation experiment (HAFEX): a long-term study including size-resolved aerosol, Sulfuric acid, OH, and monoterpenes measurements. *Atmospheric Chemistry & Physics 3*, 361–376.

Bond, G., B. Kromer, J. Beer, R. Muscheler, M. N. Evans, W. Showers, S. Hoffmann, R. Lotti-Bond, I. Hajdas, and G. Bonani (2001). Persistent Solar Influence on North Atlantic Climate During the Holocene. *Science 294*(5549), 2130–2136.

Bondo, T., M. Enghoff, and H. Svensmark (2009). Model of optical response of marine aerosols to forbush decreases. *Atmospheric Chemistry & Physics Discussions 9*, 22833–22863.

Bruce, E. P., J. Rausnitz, and J. Connell (2001). *Properties of gases and liquids* (5 ed.). McGraw-Hill.

Carslaw, K. S., R. G. Harrison, and J. Kirkby (2002, November). Cosmic Rays, Clouds, and Climate. *Science 298*, 1732–1737.

Christiansen, F., J. Haigh, and H. Lundstedt (2007). Influence of solar activity on climate. *NSI-Scientific Report 2*.

Clarke, A. D., D. Davis, V. N. Kapustin, F. Eisele, G. Chen, I. Paluch, D. Lenschow, A. R. Bandy, D. Thornton, K. Moore, L. Mauldin, D. Tanner, M. Litchy, M. A. Carroll, J. Collins, and G. Albercook (1998). Particle nucleation in the tropical boundary layer and its coupling to marine sulfur sources. *Science 282*, 89–92.

Clem, J. M. and L. I. Dorman (2000, July). Neutron Monitor Response Functions. *Space Science Reviews 93*, 335–359.

Cuffey, K. M. and S. J. Marshall (2000, April). Substantial contribution to sea-level rise during the last interglacial from the Greenland ice sheet. *Nature 404*, 591–594.

Dickinson, R. E. (1975). Solar variability and the lower atmosphere. *Bulletin American Meteorological Society 56*(12), 1240–1248.

Duldig, M. L. (2000). Muon observations. *Space Science Reviews 93*, 207–226.

Duplissy, J. e. a. (2009). Results from the cern pilot cloud experiment. *Atmospheric Chemistry & Physics Discussions 9*, C5845–C5847.

Eichkorn, S., S. Wilhelm, H. Aufmhoff, K. H. Wohlfrom, and F. Arnold (2002, July). Cosmic ray-induced aerosol-formation: First observational evidence from aircraft-based ion mass spectrometer measurements in the upper troposphere. *Geophysical Research Letters 29*, 43–1.

Eisele, F. L., E. R. Lovejoy, E. Kosciuch, K. F. Moore, R. L. Mauldin, J. N. Smith, P. H. McMurry, and K. Iida (2006, February). Negative atmospheric ions and their potential role in ion-induced nucleation. *Journal of Geophysical Research (Atmospheres) 111*, 4305–+.

Enghoff, M. B., J. O. P. Pedersen, T. Bondo, M. S. Johnson, S. Paling, and H. Svensmark (2008, OCT 16). Evidence for the Role of Ions in Aerosol Nucleation. *Journal of Physical Chemistry A 112*(41), 10305–10309.

Enghoff, M. B. and H. Svensmark (2008, August). The role of atmospheric ions in aerosol nucleation a review. *Atmospheric Chemistry & Physics 8*, 4911–4923.

Ferek, R. J., T. Garrett, P. V. Hobbs, S. Strader, D. Johnson, J. P. Taylor, K. Nielsen, A. S. Ackerman, Y. Kogan, Q. Liu, B. A. Albrecht, and D. Babb (2000, August). Drizzle Suppression in Ship Tracks. *Journal of Atmospheric Sciences 57*, 2707–2728.

Flückiger, E. O., M. R. Moser, B. Pirard, and et al. (2008). A parameterized neutron monitor yield function for space weather applications. In *International Cosmic Ray Conference*, Volume 1 of *International Cosmic Ray Conference*, pp. 289–292.

Forbush, S. (1937a). On diurnal variation in cosmic-ray intensity. *Terra Magn. 42*, 1–16.

Forbush, S. (1937b). On the effects in cosmic-ray intensity observed during the recent magnetic storm. *Physical Review 51*, 1108–09.

Forster, P., V. Ramaswamy, P. Artaxo, T. Berntsen, R. Betts, D. W. Fahey, J. Haywood, J. Lean, D. C. Lowe, G. Myhre, J. Nganga, R. Prinn, G. Raga, M. Schulz, and R. Van Dorland (2007). *Changes in Atmospheric Constituents and in Radiative Forcing. In: Climate Change 2007: The Physical Science Basis. Contribution of Working Group 1 to the Fourth Assessment Report of the Intergovenrmental Panel on Climate Change [Solomon, S., D. Qin, M. Manning, Z. Chen, M. Marquis, K.B. Averyt, M. Tignor and H.L. Miller (eds.)].* Cambridge University Press.

Foukal, P., C. Fröhlich, H. Spruit, and T. M. L. Wigley (2006, September). Variations in solar luminosity and their effect on the Earth's climate. *Nature 443*, 161–166.

Gray, L. J., J. D. Haigh, and R. G. Harrison (2005). The influence of solar changes on the earth's climate. *Hadley Centre technical note 62*, 1–81.

Haigh, J. D. (1994, August). The Role of Stratospheric Ozone in Modulating the Solar Radiative Forcing of Climate. *Nature 370*, 544–+.

Haigh, J. D. (2007, October). The Sun and the Earth's Climate. *Living Reviews in Solar Physics 4*, 2–+.

Harrison, R. G. and K. S. Carslaw (2003, September). Ion-aerosol-cloud processes in the lower atmosphere. *Reviews of Geophysics 41*, 1012–+.

Harrison, R. G. and D. B. Stephenson (2006). Empirical evidence for a nonlinear effect of galactic cosmic rays on clouds. *Proceedings of the Royal Society A 462*, 1221–1233.

Heck, D., J. Knapp, J. N. Capdevielle, G. Schatz, and T. Thouw (1998, February). *CORSIKA: a Monte Carlo code to simulate extensive air showers.* CORSIKA: a Monte Carlo code to simulate extensive air showers., by Heck, D.; Knapp, J.; Capdevielle, J. N.; Schatz, G.; Thouw, T.. Forschungszentrum Karlsruhe GmbH, Karlsruhe (Germany)., Feb 1998, V + 90 p., TIB Hannover, D-30167 Hannover (Germany).

Hess, M., P. Koepke, and I. Schult (1998, May). Optical Properties of Aerosols and Clouds: The Software Package OPAC. *Bulletin of the American Meteorological Society 79*, 831–844.

Hilary, C. V. (2000). Coronal mass ejections and forbush decreases. *Space Science Reviews 93*, 55–77.

Hirsikko, A., T. Yli-Juuti, T. Neiminen, E. Vartiainen, L. Laakso, T. Hussein, and M. Kulmala (2007). Indoor and outdoor air ions and aerosol particles in the urban atmosphere of helsinki: characteristics, sources and formation. *Boreal Environment Research 12*, 295–310.

Holben, B., T. Eck, I. Slutsker, D. Tanre, J. Buis, A. Setzer, E. Vermote, J. Reagan, Y. Kaufman, T. Nakajima, F. Lavenu, I. Jankowiak, and A. Smirnov (1998). AERONET - A federated instrument network and data archive for aerosol characterization. *Remote Sensing Environment 66*, 1–16.

Hoppel, W. A. (1985, June). Ion-aerosol attachment coefficients, ion depletion, and the charge distribution on aerosols. *journal Geophysical Research 90*, 5917–5923.

Hoppel, W. A., G. M. Frick, and J. W. Fitzgerald (1994). Marine boundeary layer measurements of new particle formation and the effects nonprecipitating clouds have.

Johnsen, S. and B. Vinther (2007). Stable Isotope Records from Greenland Ice Cores. *Nature*.

Kazil, J., E. R. Lovejoy, M. C. Barth, and K. O'Brien (2006, October). Aerosol nucleation over oceans and the role of galactic cosmic rays. *Atmospheric Chemistry & Physics 6*, 4905–4924.

Kernthaler, S. C., R. Toumi, and J. D. Haigh (1999, April). Some doubts concerning a link between cosmic ray fluxes and global cloudiness. *Geophysical Research Letters 26*, 863–866.

Kim, T. O., M. Adachi, K. Okuyama, and J. H. Seinfeld (1997). Experimental measurement of competitive ion-induced and binary homogeneous nucelation in $so_2/h_2o/n_2$ mixtures. *Aerosol Science and Technology 26*, 527–543.

Kirkby, J. (2007, November). Cosmic Rays and Climate. *Surveys in Geophysics 28*, 333–375.

Kniveton, D. R. (2004). Precipitation, cloud cover and forbush decreases in galactic cosmic rays. *Journal of Atmospheric and Terrestrial Physics 66*, 1135–1142.

Kristjánsson, J. E., A. Staple, J. Kristiansen, and E. Kaas (2002, December). A new look at possible connections between solar activity, clouds and climate. *Geophysical Research Letters 29*(23), 230000–1.

Kristjánsson, J. E., C. W. Stjern, F. Stordal, A. M. Fjæraa, G. Myhre, and K. Jónasson (2008, December). Cosmic rays, cloud condensation nuclei and clouds a reassessment using MODIS data. *Atmospheric Chemistry & Physics 8*, 7373–7387.

Kuang, C., P. H. McMurry, and A. V. McCormick (2009, MAY 14). Determination of cloud condensation nuclei production from measured new particle formation events. *Geophysical Research Letters 36*.

Kudela, K. and R. Brenkus (2004, September). Cosmic ray decreases and geomagnetic activity: list of events 1982-2002. *Journal of Atmospheric and Solar-Terrestrial Physics 66*, 1121–1126.

Kulmala, M., L. Laakso, K. E. J. Lehtinen, I. Riipinen, M. Dal Maso, T. Anttila, V.-M. Kerminen, U. Hõrrak, M. Vana, and H. Tammet (2004). Initial steps of aerosol growth. *Atmospheric Chemistry and Physics 4*, 2553–2560.

Kulmala, M., I. Riipinen, M. Sipilä, H. E. Manninen, T. Petäjä, H. Junninen, M. Dal Maso, G. Mordas, A. Mirme, M. Vana, A. Hirsikko, L. Laakso, R. M. Harrison, I. Hanson, C. Leung, K. E. J. Lehtinen, and V.-M. Kerminen (2007, October). Toward Direct Measurement of Atmospheric Nucleation. *Science 318*, 89–.

Laakso, L., S. Gagné, T. Petäjä, A. Hirsikko, P. P. Aalto, M. Kulmala, and V.-M. Kerminen (2007). Detecting charging state of ultra-fine particles: instrumental development and ambient measurements. *Atmospheric Chemistry and Physics 7*, 1333–1345.

Laakso, L., J. M. Mäkelä, L. Pirjola, and M. Kulmala (2002, October). Model studies on ion-induced nucleation in the atmosphere. *Journal of Geophysical Research (Atmospheres) 107*(D20), 4427–4445.

Laakso, L., T. Petäjä, K. E. J. Lehtinen, M. Kulmala, J. Paatero, U. Hõrrak, H. Tammet, and J. Joutsensaari (2004, July). Ion production rate in a boreal forest based on ion, particle and radiation measurements. *Atmospheric Chemistry & Physics Discussions 4*, 3947–3973.

Laaksonen, A., T. Vesala, M. Kulmala, P. Winkler, and P. Wagner (2005). Commentary on cloud modelling and the mass accomodation coefficient of water. *Atmospheric Chemistry and Physics 5*.

Labitzke, K. (1987, May). Sunspots, the QBO, and the stratospheric temperature in the north polar region. *Geophysical Research Letters 14*, 535–537.

Labitzke, K. (2005, January). On the solar cycle QBO relationship: a summary. *Journal of Atmospheric and Solar-Terrestrial Physics 67*, 45–54.

Larsen, S. H. (2005, November). Solar variability, dimethyl sulphide, clouds and climate. *Global Biogeochemical Cycles 19*.

Lee, S.-H., J. M. Reeves, J. C. Wilson, D. E. Hunton, A. A. Viggiano, T. M. Miller, J. O. Ballenthin, and L. R. Lait (2003, September). Particle Formation by Ion Nucleation in the Upper Troposphere and Lower Stratosphere. *Science 301*, 1886–1889.

Lehtinen, K. E. J. and M. Kulmala (2002). A model for particle formation and growth in the atmosphere with molecular resolution in size. *Atmospheric Chemistry and Physics 2*.

Lohmann, U. and J. Feichter (2005). Global indirect aerosol effects: a review. *Atmos. Chem. Phys. 5*, 715–737.

Lovejoy, E. R., J. Curtius, and K. D. Froyd (2004, apr). Atmospheric ion-induced nucleation of sulfuric acid and water. *Journal of Geophysical Research (Atmospheres) 109*(D08204), 1–11.

Marsh, N. and H. Svensmark (2000a, November). Cosmic Rays, Clouds, and Climate. *Space Science Reviews 94*(D6), 215–230.

Marsh, N. and H. Svensmark (2003, March). Galactic cosmic ray and El Niño-Southern Oscillation trends in International Satellite Cloud Climatology Project D2 low-cloud properties. *Journal of Geophysical Research (Atmospheres) 108*(D6), 4195–4205.

Marsh, N. D. and H. Svensmark (2000b, December). Low Cloud Properties Influenced by Cosmic Rays. *Physical Review Letters 85*, 5004–5007.

McCracken, K. G. and J. Beer (2007, October). Long-term changes in the cosmic ray intensity at Earth, 1428-2005. *Journal of Geophysical Research (Space Physics) 112*, 10101–+.

Meehl, G., J. Arblaster, K. Matthes, F. Sassi, , and H. van Loon (1976). Amplifying the pacific climate system response to a small 11 year solar cycle forcing. *Science 325*, 1114–1118.

Moraal, H., A. Belov, and M. Clem (2000). Design and co-ordination of multi-station international neutron monitor networks. *Space Science Reviews 93*, 285.

Muscheler, R., F. Joos, J. Beer, S. A. Müller, M. Vonmoos, and I. Snowball (2007, January). Solar activity during the last 1000 yr inferred from radionuclide records. *Quaternary Science Reviews 26*, 82–97.

Nagashima, K., S. Sakakibara, and K. Murakami. Response and yield functions of neutron monitor, galactic cosmic ray spectrum and its solarmodulation, derived from all the available world-wide surveys. *Nuovo Cimento*.

Neff, U., S. Burns, A. Mangini, M. Mudelsee, D. Fleitmann, and A. Matter (2001, May). Strong coherence between solar variability and the monsoon in Oman between 9 and 6kyr ago. *Nature 411*, 290–293.

Ney, E. P. (1959). Cosmic radiation and the weather. *Nature 183*, 151–452.

Pallé, E. (2005, February). Possible satellite perspective effects on the reported correlations between solar activity and clouds. *Geophysical Research Letters 32*, 3802–+.

Pallé, E. and C. J. Butler (2001, May). Sunshine records from Ireland: cloud factors and possible links to solar activity and cosmic rays. *International Journal of Climatology 21*, 709–729.

Pierce, J. R. and P. J. Adams (2007, FEB 27). Efficiency of cloud condensation nuclei formation from ultrafine particles. *Atmopsheric Chemistry and Physics 7*, 1367–1379.

Pierce, J. R. and P. J. Adams (2009, May). Can cosmic rays affect cloud condensation nuclei by altering new particle formation rates? *Geophysical Research Letters 36*(9), L09820+.

Platnick, S., M. D. King, S. A. Ackerman, W. P. Menzel, B. A. Baum, J. C. Riedi, and R. A. Frey (2003, February). The MODIS cloud products: algorithms and examples from terra. *IEEE Transactions on Geoscience and Remote Sensing 41*, 459–473.

Porter, H. S., C. H. Jackman, and A. E. S. Green (1976, July). Efficiencies for production of atomic nitrogen and oxygen by relativistic proton impact in air. *Journal of Chemistry and Physics 65*, 154–167.

Pudovkin, M. I. and S. V. Veretenenko (1995, September). Cloudiness decreases associated with Forbush decreases of galactic cosmic rays. *Journal of Atmospheric and Terrestrial Physics 57*, 1349–1355.

Raes, F. and A. Janssens (1985). Ion-induced aerosol formation in a $h_2o - h_2so_4$ system–1. extension of the classical theory and search for experimental evidence. *Journal of Aerosol Science 16*(3), 217–227.

Raes, F., A. Janssens, and G. Eggermont (1985). A synergism between ultraviolet and gamma radiation in producing aerosol particles from $so_2 - h_2so_4$ laden atmospheres. *Atmospheric Environment 19*(7), 1069–1073.

Ramanathan, V., R. D. Cess, E. F. Harrison, P. Minnis, B. R. Barkstrom, E. Ahmad, and D. Hartmann (1989, January). Cloud-Radiative Forcing and Climate: Results from the Earth Radiation Budget Experiment. *Science 243*, 57–63.

Rao, U. R. (1976). High energy cosmic ray observations during august 1972. *Space Science Reviews 19*.

Reid, G. C. (1987). Influence of solar variability on global sea surface temperatures. *Nature 329*, 142–143.

Ringer, M. A. and K. P. Shine (1997). Sensitivity of the Earth's radiation budget to interannual variations in cloud amount. *Climate Dynamics 13*, 213–222.

Rosenfeld, D., Y. J. Kaufman, and I. Koren (2006, June). Switching cloud cover and dynamical regimes from open to closed Benard cells in response to the suppression of precipitation by aerosols. *Atmospheric Chemistry & Physics 6*, 2503–2511.

Rossow, W. and R. Schiffer (1999, July). ISCCP Cloud Data Products: Advances in Understanding Clouds from ISCCP. *Bull. Amer. Meteor. Soc. 80*, 2261–2288.

Rycroft, M. J., S. Israelsson, and C. Price (2000, November). The global atmospheric electric circuit, solar activity and climate change. *Journal of Atmospheric and Solar-Terrestrial Physics 62*, 1563–1576.

S., T. (1974). Pollution and the planetary albedo. *Atmos. Environ 8*, 1251–1256.

Sano, I. (2004). Optical thickness and Angstrom exponent of aerosols over the land and ocean from space-borne polarimetric data. *Advances in Space reseearch 34*.

Sanuki, T., M. Motoki, H. Matsumoto, E. S. Seo, J. Z. Wang, K. Abe, K. Anraku, Y. Asaoka, M. Fujikawa, M. Imori, T. Maeno, Y. Makida, N. Matsui, H. Matsunaga, J. Mitchell, T. Mitsui, A. Moiseev, J. Nishimura, M. Nozaki, S. Orito, J. Ormes, T. Saeki, M. Sasaki, Y. Shikaze, T. Sonoda, R. Streitmatter, J. Suzuki, K. Tanaka, I. Ueda, N. Yajima, T. Yamagami, A. Yamamoto, T. Yoshida, and K. Yoshimura (2000, December). Precise Measurement of Cosmic-Ray Proton and Helium Spectra with the BESS Spectrometer. *Astro. Phys. J. 545*, 1135–1142.

Schuster, G. L., O. Dubovik, and B. N. Holben (2006, April). Angstrom exponent and bimodal aerosol size distributions. *Journal of Geophysical Research (Atmospheres) 111*, 7207–+.

Seinfeld, J.H.; Pandis, S. (2006). *Atmospheric Chemsitry and Physics : From Air Pollution to Climate Change* (2 ed.). Wiley.

Shaviv, N. and J. Veizer (2003). Celestial driver of Phanerozoic climate. *Geological Society of America Today*, 13401–+.

Shaviv, N. J. (2008, November). Using the oceans as a calorimeter to quantify the solar radiative forcing. *Journal of Geophysical Research - Space Physics 113*(A11), A11101+.

Sloan, T. and A. W. Wolfendale (2008, April). Testing the proposed causal link between cosmic rays and cloud cover. *Environmental Research Letters 3*(4), 044001–+.

Smart, D. F. and M. A. Shea (2005). A review of geomagnetic cutoff rigidities for earth-orbiting spacecraft. *Advances in Space Research 36*, 2012–2020.

Solanki, S.K. snd N.A., K. (2003, May). Can solar variability explain global warming since 1970? *Journal of Geophysical Research 108*, 1200.

Svensmark, H. (2000, July). Cosmic Rays and Earth's Climate. *Space Science Reviews 93*, 175–185.

Svensmark, H. (2007, February). Cosmoclimatology: a new theory emerges. *Astronomy and Geophysics 48*(1), 010000–1.

Svensmark, H., T. Bondo, and J. Svensmark (2009, August). Cosmic ray decreases affect atmospheric aerosols and clouds. *Geophysical Research Letters 36*(15), L15101+.

Svensmark, H. and E. Friis-Christensen (1997, July). Variation of cosmic ray flux and global cloud coverage - a missing link in solar-climate relationships. *Journal of Atmospheric and Solar-Terrestrial Physics 59*(11), 1225–1232.

Svensmark, H., J. O. P. Pedersen, N. D. Marsh, M. B. Enghoff, and U. I. Uggerhøj (2007, February). Experimental evidence for the role of ions in particle nucleation under atmospheric conditions. *Royal Society of London Proceedings Series A 463*, 385–396.

Tinsley, B. A. (2000). Influence of solar wind on the global electric circuit, and inferred effects on cloud microphysics, temperature, and dynamics in the troposphere. *Space Science Reviews 94*, 231–258.

Todd, M. C. and D. R. Kniveton (2001, December). Changes in cloud cover associated with Forbush decreases of galactic cosmic rays. *Journal of Geophysical Research 106*, 32031–32042.

Todd, M. C. and D. R. Kniveton (2004). Short-term variability in satellite-derived cloud cover and galactic cosmic rays: an update. *Journal of Atmospheric and Terrestrial Physics 66*, 1205–1211.

Troshichev, O. A. and I. P. Gabis (1998, September). Variations of solar UV irradiance related to short-term and medium-term changes of solar activity. *Journal of Geophysical Research 103*, 20659–20668.

Turco, R. P., J.-X. Zhao, and F. Yu (1998). A new source of tropospheric aerosols: Ion-ion recombination. *Geophysical Research Letters 25*(5), 635–638.

Usoskin, I. G., L. Desorgher, P. Velinov, M. Storini, E. O. Flückiger, R. Bütikofer, and G. A. Kovaltsov (2008, September). Ionization of the earth's atmosphere by solar and galactic cosmic rays. *Acta Geophysica*, 40–+.

Usoskin, I. G., O. G. Gladysheva, and G. A. Kovaltsov (2004, December). Cosmic ray-induced ionization in the atmosphere: spatial and temporal changes. *Journal of Atmospheric and Solar-Terrestrial Physics 66*, 1791–1796.

Usoskin, I. G. and G. A. Kovaltsov (2008, July). Cosmic rays and climate of the Earth: Possible connection. *Comptes Rendus Geoscience, v. 340, iss. 7, p. 441-450. 340*, 441–450.

Weber, R. J., G. Chen, D. D. Davis, R. L. Mauldin III, D. J. Tanner, F. L. Eisele, A. D. Clarke, D. C. Thornton, and A. R. Bandy (2001). Measurements of enhanced H_2SO_4 and 3-4 nm particles near a frontal cloud during the First Aerosol Characterization Experiment (ACE 1). *Journal of Geophysical Research 106*(D20), 24107–24117.

Weber, R. J., J. J. Marti, P. H. McMurry, F. L. Eisele, D. J. Tanner, and A. Jefferson (1996). Measured atmospheric new particle formation rates: Implications for nucleation mechanisms. *Chemical Engineering Communications 151*(1), 53–64.

Weng, F., N. Grody, A. Ferraro, A. Basist, and D. Forsyth (1997, September). Cloud liquid water climatology from the special sensor microwave imager. *Journal of Climate*, 1086–1096.

Wolf, S. (2006, October). Mie Scattering by Ensembles of Particles with Very Large Size Parameters. *Astrophysics Software Database*, 6–+.

Yu, F. (2006, November). From molecular clusters to nanoparticles: second-generation ion-mediated nucleation model. *Atmospheric Chemistry & Physics 6*, 5193–5211.

Yu, F. (2009). Ion-mediated nucleation in the atmosphere: Key controlling parameters, implications, and look-up table. *Journal of Geophysical Research*.

Yu, F. and R. P. Turco (2000). Ultrafine aerosol formation via ion-mediated nucleation. *Geophysical Research Letters 27*, 883–886.

Yu, F. and R. P. Turco (2001). From molecular clusters to nanoparticles: Role of ambient ionization in tropospheric aerosol formation. *Journal of Geophysical Research 106*(D5), 4797–4814.

Acknowledgements

This thesis would never have been made, if I had not received great help from a number of people:

- Henrik Svensmark: You gave me the opportunity to work on these exciting topics. I am very grateful to you for this. It has been a good time for me and a big challenge suddenly working on something which has the World's attention. The constant focus on our work has sharpened and toughened me in a good way. You have given me support and trusted me to do my job. Thanks so much.
- Martin Enghoff: This thesis would be seriously worse, if it had not been for your constant help, knowledge and support. Thanks for putting up with my babbling and always being ready for discussions. The last paper we did together was one of the best team performances I have been involved in.
- Nigel Marsh: You got me interested in Forbush decreases and was a constant help during the first year of the PhD. It was a shame you had to leave. Thanks for reading my thesis and for giving most valuable input.
- Freddy Christiansen and Jens Olaf Pepke Pedersen: You two are constant sources of strange knowledge and it has been fun to learn from you. Freddy, thanks for reading my thesis, help in developing the aerosol code and for all the liquorice I have eaten.
- Special thanks to Kim, Birte, Ulla, Lars, Olivier and Birthe for helping with issues related to my thesis.

Appendix A: NM and Muon telescope Response to Solar cycles

In order to relate the changes in ionization during a FD to those observed over a solar cycle monthly data from both NM and the Nagoya station over the last 3 solar cycles is used to compute the relative changes in counts over a solar cycle as expressed by eq. 3.12.

Figure 7.1 give the percentage decrease in NM and Muon telescopes over different solar cycles as a function of median rigidity, P_m. By comparing with Figure 3.4, it becomes clear that at the surface close to equator, where $P_m \sim$ 20-40GV, the solar cycle is larger than $\gtrsim 3\%$ and therefore should be visible in cloud data above the noise level of $\sim 2\%$ as described in section 4.9.

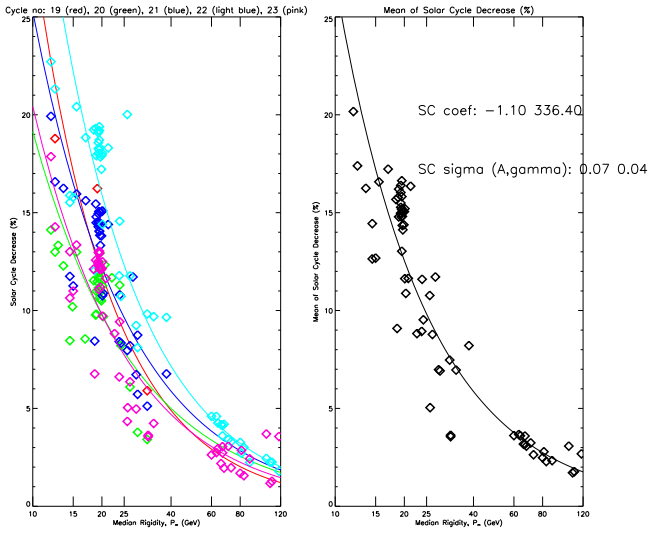

Figure 7.1: Left) Percentage decrease in NM and Muon telescope counts over different solar cycles as a function of median rigidity, P_m. Each stations data was smoothed with a 13 month running mean. This was done to reduce the local fluctuations before the decrease from solar min to solar max was found for each cycle. Colours indicate the solar cycle number with start dates of: cycle 19 (red) April 1954, cycle 20 (green) October 1964, cycle 21 (blue) June 1976, cycle 22 (light blue) September 1986, cycle 23 (pink) May 1996. Left Figure courtesy of Nigel Marsh. Right) Mean of the above plots for the last 3 solar cycles relevant to this thesis. Here the fit to eq. 3.12 is given. Right figure is a rerun by me of Nigel Marsh' code averaging over the last 3 solar cycles (where cloud data is available).

By fitting to Eq. (3.12) the parameters determining the change over the solar cycle is now given by $A_{SC} = 336 \pm 46$ and $\gamma_{SC} = -1.10 \pm 0.04$. The uncertainty of the fit in A is given in table the column $\pm\delta A$ is 3.3.

Appendix B: Table of Rigidities

Stat	Alt	R_c	R_m^{min}	R_m^{max}	R_m M	Stat	Alt	R_c	R_m^{min}	R_m^{max}	R_m M
AATA	806	6.66	21.8	24.2	20.9	ERVN	2000	7.60	20.8	22.7	20.4
AATB	3340	6.69	17.0	18.6	17.2	ERV3	3200	7.60	18.9	20.5	18.9
AATC	1670	6.67	19.7	21.7	19.3	ESOI	2025	10.00	25.5	27.4	24.6
AATH	3340	6.69	17.0	18.6	17.2	FSMT	0	0.30	15.9	19.5	16.9
AHMD	50	15.94	45.5	48.1	40.8	FRBG	0	3.41	18.4	21.5	18.1
ALGR	300	14.67	41.2	43.8	37.4	FUSH	66	10.55	33.1	35.7	30.0
ALRT	57	0.10	15.7	19.3	16.7	GFSY	0	3.50	18.5	21.6	18.2
ALBQ	1567	4.47	15.7	17.9	16.1	GOTT	273	3.00	16.7	19.8	17.0
APTY	177	0.65	15.2	18.8	16.4	GSBY	46	0.52	15.7	19.3	16.8
ATHN	40	8.72	29.1	31.8	26.5	GLMG	2743	11.58	27.2	29.0	26.4
BERK	70	4.54	20.1	23.0	19.3	HAIF	2300	10.75	26.4	28.3	25.6
BGNR	550	5.00	19.3	21.9	18.8	HALL	100	3.07	17.4	20.6	17.5
BJNG	48	9.56	31.0	33.6	28.1	HBRT	0	1.88	16.3	19.8	17.0
BRSB	0	7.21	26.0	28.7	23.9	HEIS	20	0.10	15.8	19.5	16.8
BRUT	15	10.42	33.1	35.7	29.9	HFLK	2290	4.37	14.3	16.2	14.9
BUEN	0	10.63	33.6	36.2	30.3	HLE1	3052	13.30	30.0	31.8	29.2
CALG	1128	1.08	12.6	15.5	14.4	HLEA	3052	13.30	30.0	31.8	29.2
CAPS	0	0.45	15.9	19.5	16.9	HRMS	26	4.90	21.0	23.9	19.9
CASY	0	0.01	15.9	19.5	16.9	HRST	23	2.93	17.5	20.7	17.5
CDBA	434	11.45	33.4	35.9	30.7	HUAN	3400	13.45	29.7	31.5	29.0
CHCL	5200	13.10	26.8	28.3	26.6	INVK	21	0.18	15.8	19.5	16.8
CHGO	200	1.72	15.5	18.9	16.4	INVC	0	1.86	16.3	19.8	17.0
CHUR	39	0.21	15.7	19.4	16.8	IRK2	2000	3.66	13.6	15.7	14.4
CLMX	3400	3.03	10.8	12.5	12.1	IRK3	3000	3.66	12.1	13.9	13.2
COLL	91	0.54	15.5	19.1	16.7	IRKT	433	3.66	17.2	20.1	17.2
DALS	208	4.35	19.2	22.1	18.7	JUN1	3550	4.48	12.9	14.5	13.7
DENV	1600	2.91	13.2	15.5	14.2	JUNG	3550	4.48	12.9	14.5	13.7
DPRV	145	1.02	15.4	18.9	16.5	KAMP	1196	14.98	38.1	40.4	35.6
DRBS	225	3.24	17.2	20.3	17.3	KERG	0	1.19	15.9	19.6	16.9
DRHM	0	1.41	16.0	19.6	16.9	KHAB	0	5.54	22.4	25.3	21.0
DRWN	0	14.19	41.7	44.4	37.4	KIEL	54	2.29	16.5	19.9	17.0
ELSW	0	0.79	15.9	19.5	16.9	KIEV	120	3.62	18.3	21.3	18.0

Table 7.1: List of altitude, geomagnetic cut off (R_c) and median rigidities. R_m^{min} and R_m^{max} are median rigidities calculated from Clem and Dorman (2000) under solar minimum and solar maximum. R_m M is median rigidity calculated using (Moraal et al., 2000). For the thesis R_m^{max} is used. Units of GV.

Stat	Alt	R_c	R_m^{min}	R_m^{max}	R_m M	Stat	Alt	R_c	R_m^{min}	R_m^{max}	R_m M
KLNG	70	2.43	16.6	20.0	17.1	PTFM	1351	7.30	21.6	23.8	20.9
KODI	2343	17.47	39.8	41.9	38.0	PWNK	0	0.50	15.9	19.5	16.9
KRNA	400	0.54	14.5	17.9	15.9	PRAG	215	3.53	17.8	20.7	17.6
KULA	915	13.30	35.5	37.9	33.0	PRED	1614	4.29	15.3	17.5	15.8
LAE	0	15.52	44.8	47.5	40.1	REWA	100	15.89	45.1	47.7	40.5
LARC	40	3.00	17.6	20.8	17.6	RIOD	0	11.73	36.1	38.7	32.5
LDVL	3094	3.03	11.1	12.9	12.4	ROME	60	6.32	23.8	26.5	22.1
LEED	72	2.20	16.4	19.7	16.9	RSLT	17	0.10	15.8	19.5	16.9
LINC	350	2.22	15.4	18.6	16.2	SACR	3000	4.98	14.3	16.1	14.9
LMKS	2634	4.00	13.2	15.0	14.0	SDNY	43	4.69	20.5	23.4	19.6
LNDH	140	3.00	17.2	20.3	17.3	SEOL	45	10.79	33.7	36.4	30.5
LNDN	45	2.73	17.1	20.4	17.3	SLMA	2283	1.14	10.5	12.9	12.6
LCRS	540	11.00	32.0	34.4	29.5	SMRD	750	7.65	24.1	26.4	22.8
MCMD	48	0.01	15.7	19.3	16.8	SNAE	52	1.06	15.7	19.3	16.8
MGDN	0	2.10	16.5	20.0	17.1	SNA8	52	1.06	15.7	19.3	16.8
MINA	4000	12.51	27.1	28.7	26.7	SMFR	570	5.51	20.3	22.8	19.5
MKPU	100	13.23	39.0	41.6	35.1	SOPO	2820	0.11	9.7	12.0	11.9
MNCH	500	4.14	17.9	20.6	17.7	SPBN	0	0.20	15.9	19.5	16.9
MOSC	200	2.46	16.2	19.4	16.7	SVER	300	2.30	15.7	18.9	16.4
MOS5	200	2.46	16.2	19.4	16.7	SWTH	80	1.92	16.1	19.5	16.8
MRCH	0	0.06	15.9	19.5	16.9	SYWA	15	0.42	15.8	19.5	16.9
MRKA	135	10.16	31.9	34.5	29.0	TASH	565	8.34	26.1	28.6	24.4
MRNY	30	0.04	15.8	19.4	16.8	TBLS	510	6.91	23.3	25.8	22.0
MTNR	2770	11.39	26.8	28.6	26.1	TERA	45	0.01	15.7	19.3	16.8
MTWL	725	1.89	14.0	17.0	15.3	THUL	260	0.10	14.9	18.4	16.2
MTWS	1900	1.24	11.1	13.6	13.1	TIBT	4300	14.10	29.7	31.3	29.2
MURM	0	0.65	15.9	19.5	16.9	TKYO	40	11.61	35.6	38.2	32.1
MWSN	0	0.22	15.9	19.5	16.9	TSMB	1240	9.29	26.0	28.2	24.7
MXCO	2274	9.53	24.1	25.9	23.4	TURK	32	1.36	15.9	19.5	16.8
NAIN	0	0.40	15.9	19.5	16.9	TXBY	0	0.53	15.9	19.5	16.9
NDRH	0	2.76	17.4	20.6	17.5	UPPS	0	1.43	16.0	19.6	16.9
NLCH	550	7.70	24.8	27.3	23.3	USHU	0	5.68	22.7	25.5	21.2
NLC2	1850	7.70	21.3	23.3	20.8	UTRT	0	2.76	17.4	20.6	17.5
NLC3	3150	7.70	19.1	20.8	19.1	VICT	71	1.86	16.0	19.5	16.8
NRLK	0	0.63	15.9	19.5	16.9	VSTK	3488	0.10	9.0	11.0	11.2
NTHF	287	1.43	15.0	18.4	16.2	WEIS	427	4.16	18.1	20.9	17.9
NVBK	163	2.91	17.0	20.1	17.2	WELL	0	3.42	18.4	21.5	18.1
NWRK	50	1.97	16.2	19.7	16.9	WLKS	0	0.01	15.9	19.5	16.9
OTWA	101	1.08	15.5	19.1	16.6	YKTK	105	1.70	15.8	19.3	16.7
OULU	0	0.81	15.9	19.5	16.9	ZUGS	2960	4.24	13.1	14.9	13.9
PICD	2860	5.36	15.2	16.9	15.6						

Table 7.2: List of altitude, geomagnetic cut off (R_c) and median rigidities. R_m^{min} and R_m^{max} are median rigidities calculated from Clem and Dorman (2000) under solar minimum and solar maximum. R_m M is median rigidity calculated using (Moraal et al., 2000). For the thesis R_m^{max} is used. Units of GV.

Appendix C: Additional work on FDs

Prior to the work presented in the thesis, I made a number of initial studies of FD effects on clouds. Without having table 3.3 ranking the strengths of the FDs, it was however difficult to know what response to expect. Some of the analysis, though unfinished, was still relevant for the thesis, and I have decided to include two fragments of analysis in this appendix. Later this work could be extended using table 3.3.

According to the GCR-cloud hypothesis the cloud contents should be significantly lower

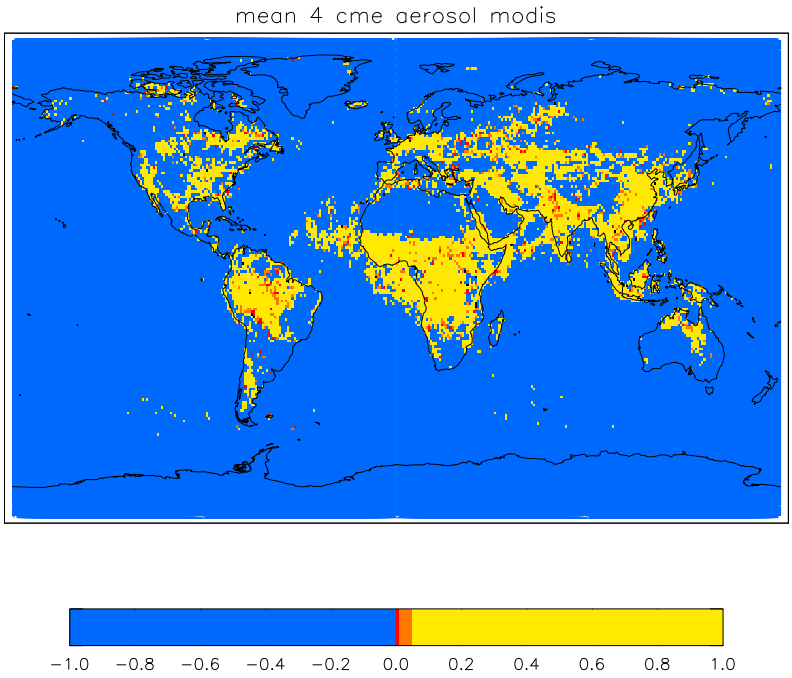

Figure 7.2: .

Map of students T test of two aerosol optical thickness arrays calculated before and after a FD minimum. Mean of 4 FDs. The blue areas are where the amount of data points are insufficient to calculate a Students T test. The yellow area is areas where the calculation could be performed but where no significant change in mean occurs. The orange/red areas are where the mean is significantly (over the 95% level) different before and after the FD. No effect of FDs on aerosol optical thickness is seen.

after the FD than before. The idea behind Figure 7.2 is to see if epoch superposed arrays (see section 4.6) have significantly different means before and after a FD. Here an analysis is presented of MODIS aerosol optical thickness data from an epoch analysis of 4 FDs (2003/10/24,2004/01/17,2004/07/21,2005/09/06). Only 5 days before and after the FD minimum is analyzed. For this plot no significant results were obtained and no effect of overlaying 4 FDs were seen. It could be interesting to create the mean of the spatial plot and then repeat the same analysis by moving the 5 by 5 window over the whole FD period

similar to what was done in section 3.3. In this way a T-statistics profile resembling a FD similar to that observed in the NM could appear in the climate data.

As an appetizer a single FD event (11 September 2005) was analyzed using Meteosat data. The Meteosat delivers 15 minutes data in bufr format. This rather tedious format can be extracted to txt files using a Fortran program (developed by European Centre for Medium Range Weather Forecasts (ECMWF)) containing information about low, mid and high clouds over the Meteosat geostationary footprint area that covers the most of Europe and Africa. I developed a program to extract daily global means from the 15 minutes data text files. A plot of a FD data from Meteosat low clouds is shown in Figure 7.3. No effect of cosmic rays on the low clouds can be seen for this event. It would be very interesting to repeat many of the analysis presented in the thesis using Meteosat data.

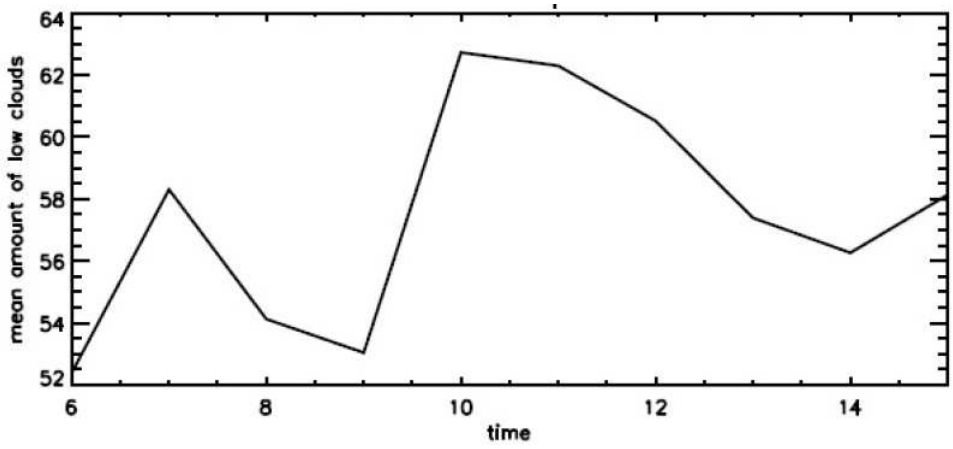

Figure 7.3: .

Meteosat Second Generation daily low cloud cover for the Forbush decrease 11 September 2005. Time in day of month. No effect on low clouds for this FD.

Appendix D: The Papers

The following three papers are presented on the pages hereafter.

Paper I Svensmark, Henrik, Bondo, Torsten and Svensmark, Jacob (2009), *Cosmic ray decreases affect atmospheric aerosols and clouds*, Geophys. Res. Lett., 36, L15101, doi:10.1029, 2009GL038429 (Svensmark et al., 2009).

Paper II Enghoff, Martin B., Pedersen, Jens Olaf P., Bondo, Torsten, Johnson, Matthew S., Paling, Sean and Svensmark, Henrik, *Evidence for the role of ions in Aerosol Nucleation*. Phys. Chem. A, 2008, 112 (41) (Enghoff et al., 2008)

Paper III: Bondo, Torsten, Enghoff, Martin B. and Henrik Svensmark. *"Model of optical response of marine aerosols to Forbush decreases"*. Atmos. Chem. Phys. Discuss., 9, 22833-22863, 2009. (Bondo et al., 2009)

Cosmic ray decreases affect atmospheric aerosols and clouds

Henrik Svensmark,[1] Torsten Bondo,[1] and Jacob Svensmark[1]

Received 31 March 2009; revised 1 June 2009; accepted 17 June 2009; published 1 August 2009.

[1] Close passages of coronal mass ejections from the sun are signaled at the Earth's surface by Forbush decreases in cosmic ray counts. We find that low clouds contain less liquid water following Forbush decreases, and for the most influential events the liquid water in the oceanic atmosphere can diminish by as much as 7%. Cloud water content as gauged by the Special Sensor Microwave/Imager (SSM/I) reaches a minimum ≈7 days after the Forbush minimum in cosmic rays, and so does the fraction of low clouds seen by the Moderate Resolution Imaging Spectroradiometer (MODIS) and in the International Satellite Cloud Climate Project (ISCCP). Parallel observations by the aerosol robotic network AERONET reveal falls in the relative abundance of fine aerosol particles which, in normal circumstances, could have evolved into cloud condensation nuclei. Thus a link between the sun, cosmic rays, aerosols, and liquid-water clouds appears to exist on a global scale.
Citation: Svensmark, H., T. Bondo, and J. Svensmark (2009), Cosmic ray decreases affect atmospheric aerosols and clouds, *Geophys. Res. Lett.*, *36*, L15101, doi:10.1029/2009GL038429.

1. Introduction

[2] Explosive events on the sun provide natural experiments for testing hypotheses about solar influences on the Earth. A conspicuous effect is the sudden reduction, over hours to days, in the influx of galactic cosmic rays (GCRs), first noticed by Scott E. Forbush in 1937. Such Forbush decreases (FDs) are now understood to be the result of magnetic plasma clouds from solar coronal mass ejections that pass near the Earth and provide a temporary shield against GCRs [*Hilary*, 2000]. Whether or not any consequences of these events are perceptible in the weather has been a subject of debate for 50 years [*Ney*, 1959; *Dickinson*, 1975; *Tinsley*, 2008]. Recent attention has focused on the question of whether an effect on clouds due to changes in atmospheric ionization by GCRs is observable [*Svensmark and Friis-Christensen*, 1997; *Marsh and Svensmark*, 2000; *Kniveton*, 2004; *Todd and Kniveton*, 2004; *Harrison and Stephenson*, 2006], or is not observable [*Kristjánsson and Kristiansen*, 2000; *Sloan and Wolfendale*, 2008; *Kristjánsson et al.*, 2008]. Here we report clear signals of changes in both the liquid water content of the Earth's low clouds and the relative abundance of fine atmospheric aerosols, during the days that follow the FDs.

2. Ranking Forbush Decreases by Their Low-Altitude Effects

[3] An important preliminary step in the present work is to distinguish quantitatively between "strong" and "weak" FDs, by calculating changes in ionization in the atmosphere due to each FD. Because we are concerned with clouds in the lower atmosphere, we choose as the reference the average ionization below 3 km altitude during the period for which cloud water data are available, 1987–2007. From responses to an FD in about 130 neutron monitors world-wide and the Nagoya muon detector, the changes in the primary cosmic ray spectrum at 1 AU are derived. This procedure, and the subsequent Monte Carlo simulations of ionization by cosmic ray showers, are explained in the auxiliary material.[2] Table 1 lists the strongest FDs, 1987–2007. The first and second columns give the numerical order and the dates of the Forbush minima in the daily averaged GCRs. The third column is the strength of the FD, defined by the change in the ionization at the minimum, relative to a base period 14 days before the minimum. The value of the ionization decrease is normalized to be relative to the variation in ionization during the solar cycle at a latitude of 45 deg. On average the solar cycle variation in GCR ionization is 10–15% below 6 km altitude [*Bazilevskaya et al.*, 2008].

3. Responses to FDs in Liquid Water Clouds and Aerosols

[4] Three independent sources of satellite data on liquid water clouds are used to explore responses to FD events. The Special Sounder Microwave Imager (SSM/I) [*Wentz*, 1997; *Weng et al.*, 1997] observes changes in the cloud liquid water content (CWC) over the world's oceans. The Moderate Resolution Imaging Spectroradiometer (MODIS) on NASA's Terra and Aqua satellites (land and oceans) gives the liquid water cloud fraction (LWCF). The International Satellite Cloud Climate Project (ISCCP) [*Rossow and Schiffer*, 1991] provides data on IR detection of low clouds (<3.2 km) over the oceans. Substantial declines in liquid water clouds, apparently tracking the declining cosmic rays and reaching minima some days after the GCR minima, were readily detectable for the strongest events in Table 1, whether considered individually or in superpositions of several events.

[5] To investigate a possible mechanism, we use observational data on aerosols in the atmosphere as monitored by the solar photometers of the AERONET program, with

[1]National Space Institute, Technical University of Denmark, Copenhagen, Denmark.

0094-8276/09/2009GL038429$05.00

[2]Auxiliary materials are available in the HTML. doi:10.1029/2009GL038429.

Table 1. Twenty-Six Solar Events in the Period 1987–2007 are Here Ranked According to Their Depression of Ionization in the Earth's Lower Atmosphere, Gauged as a Percentage of the Normal Overall Variation in Ionization During the Course of a Solar Cycle[a]

Order	Date	Decrease (%)
1	**31/10/2003**	119
2	13/6/1991	87
3	**19/1/2005**	83
4	**13/9/2005**	75
5	15/3/1989	70
6	**16/7/2000**	70
7	**12/4/2001**	64
8	29/10/1991	56
9	9/7/1991	54
10	29/11/1989	54
11	**10/11/2004**	53
12	**26/9/2001**	50
13	25/3/1991	48
14	**17/7/2005**	47
15	**25/9/1998**	45
16	**27/7/2004**	45
17	10/9/1992	44
18	**31/5/2003**	44
19	**25/11/2001**	39
20	**15/5/2005**	38
21	**28/8/2001**	37
22	**27/8/1998**	36
23	10/5/1992	35
24	27/2/1992	33
25	**18/2/1999**	33
26	**2/5/1998**	28

[a]Variations are set to 100%. The dates given are those of the minima of the Forbush decreases (FD) reported from neutron monitors. The bold dates are the FD for which AERONET data are available, with the earliest occurring in 1998. In general, the FD were chosen for their strength, so only FD with reduction larger than 7% in the South Pole neutron monitor (cutoff rigidity 0.06 GV) were selected. Three events 13–27 October 1989 were omitted because they were so close in time that they interfered with one another and were also interspersed with large ground level events.

many stations well distributed over the globe. The relative blocking of sunlight of different wavelengths is given by the Angstrom exponent α in the aerosol extinction law, $\tau(\lambda_i) = \tau_1 \lambda_i^{-\alpha}$, where $\tau(\lambda_i)$ is the aerosol optical thickness at a given wavelength λ_i and τ_1 is the approximate optical thickness at a wavelength of 1 micron. In the case of measurements at two wavelengths λ_1 and λ_2 the fitted exponent $\alpha_{1,2}$ provides information about the relative abundance of fine aerosols. Long wavelengths respond to their volume fraction, whilst short wavelengths are sensitive to the effective radius of the fine mode (<250 nm) aerosol [*Schuster et al.*, 2006]. Figure 1a averages the AERONET data and GCR data for the five strongest FDs in the period covered by AERONET from 1998 onward (order numbers 1, 3, 4, 6, and 7 in Table 1). A rapid decrease in the Angstrom exponent for 340 nm and 440 nm closely follows the GCR decline, leading to a minimum about 5 days after the Forbush minimum, and is consistent with an increase in the effective radius of the fine mode due to a progressive decline in the abundance of the smallest particles among the fine mode aerosols, or, equivalently, their enhanced removal to larger particles.

[6] Figure 1b superposes the SSM/I data for CWC for the same five FD events. Notice that the CWC minimum occurs 4 days later than the fine aerosol minimum in the AERONET plot, as might be expected if an aerosol change precedes cloud changes, and if there is no appreciable transport time between the region in which changes occur and the sampling region. Figures 1c and 1d plot observations of the LWCF from MODIS, and low oceanic clouds from ISCCP, superposed for the same events.

4. Clouds and Aerosols in Many FD Events

[7] The robustness of FD effects on the Earth's lower atmosphere was tested by using the events in Table 1 to see

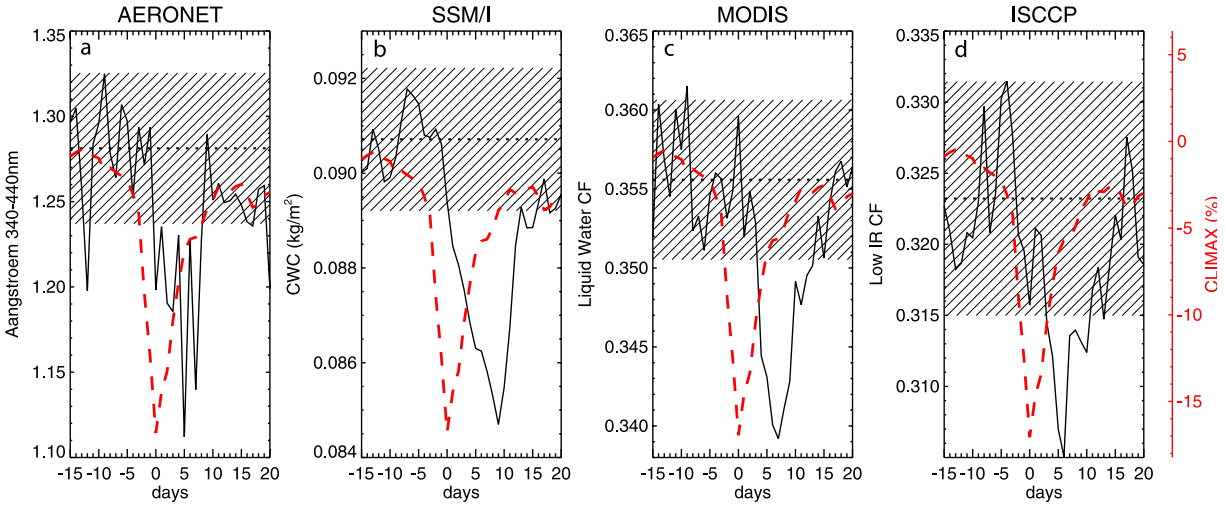

Figure 1. The evolution of (b) cloud water content (SSM/I), (c) liquid water cloud fraction (MODIS), and (d) low IR-detected clouds (ISCCP) is here averaged for the 5 strongest Forbush decreases that their data sets have in common (order numbers 1, 3, 4, 6, and 7 in Table 1) and is compared with (a) the corresponding evolution of fine aerosol particles in the lower atmosphere (AERONET). In (a) each data point is the daily mean from about 40 AERONET stations world-wide, using stations with more than 20 measurements a day. Red curves show % changes in GCR neutron counts at Climax. The broken horizontal lines denote the mean for the first 15 days before the Forbush minimum, and the hatched zones show $\pm 1\sigma$ for the data, estimated from the average variance of a large number of randomly chosen periods of 36 days of each of the four data sets. The effects on clouds and aerosols are not dominated by any single event among the 5 averaged. Examples of SSM/I data for several individual events are shown in the auxiliary material.

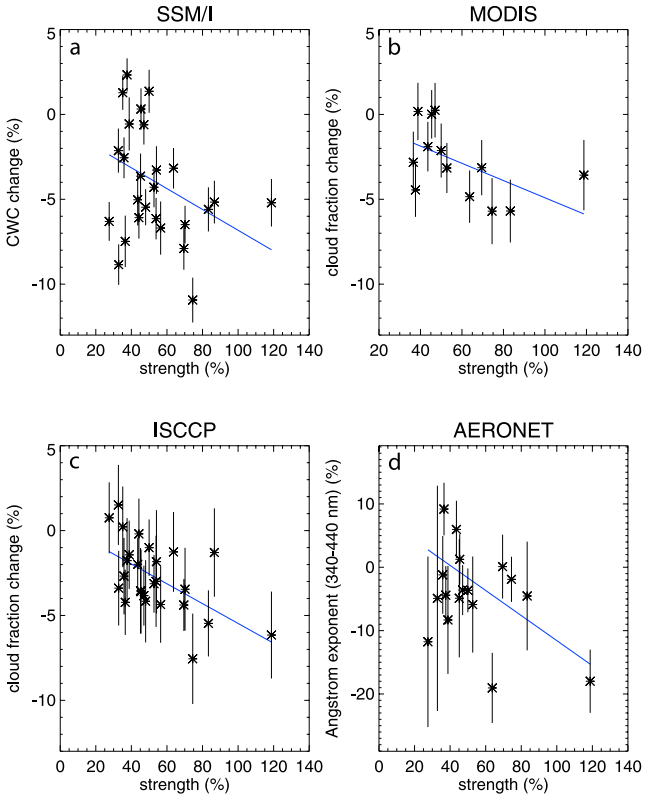

Figure 2. Quantitative comparison of effect of the Forbush Decrease magnitude in each of the four data sets. The number of events shown depends on the longevity of each data set: (a) 26 FDs for cloud water content (SSM/I), (b) 13 FDs for liquid water cloud fraction (MODIS), (c) 26 FDs for low IR cloud fraction, below 3.2 km altitude (ISCCP), and (d) 13 FDs for fine aerosol particles (AERONET). The blue line in each is a weighted linear fit to the data. The slopes are all significantly different from zero (at 0.95 level), and so confirm a stronger decrease in liquid water clouds and in fine aerosols for a stronger FD. The delay τ until the minimum following the FD minimum and regression coefficients ($y = A + Bx$) are for SSM/I $\tau = 7.9 \pm 6.0$ days and $A = -0.69 \pm 0.69$ and $B = -0.061 \pm 0.012$, for MODIS $\tau = 7.8 \pm 5.2$ days and $A = 0.16 \pm 1.37$ and $B = -0.051 \pm 0.023$, for ISCCP $\tau = 10.9 \pm 6.7$ days and $A = 0.37 \pm 0.98$ and $B = -0.058 \pm 0.017$, and for AERONET $\tau = 6.9 \pm 6.5$ days and $A = 8.21 \pm 3.49$ and $B = -0.20 \pm 0.059$.

how the responses vary with the strength of the FD. To start with Figure 2a, each data point was obtained by first filtering the CWC data from SSM/I using a Gaussian of width 2 days and total length of 10 days, to reduce fluctuations. Then the minimum of the filtered curve was identified in the interval day 0 to day 20 after the FD minimum. The CWC minimum was rated as the percentage drop relative to a base level given by the average level on days −15 to −5 before the FD minimum, whilst the uncertainty was defined as the variance of the residuals between the filtered and the unfiltered CWC. The resulting 26 data points plotted in Figure 2a reveal the relation between strength of the FD events and the corresponding minima in CWC.

[8] Two other independent data sets on liquid water clouds were tested in the same way: LWCF from MODIS, matched to 13 events 2000–2007 (Figure 2b), and low IR clouds from ISCCP for 26 events 1987–2007 (Figure 2c). In Figure 2d, the aerosol data from AERONET go through the same analysis, with 17 events 1998–2007. In all four cases, the blue regression lines suggest that the minima in clouds or fine aerosols deepen with increasing FD strength. The slopes differ from zero at the 0.95 significance level (linear regression with subsequent t-test). Using Monte Carlo simulations with random dates instead of the FD dates the distribution of slopes showed that the FD slopes are all significant at the 0.95 level, except for MODIS, where the slope is significant at the 0.92 level.

5. Discussion

[9] The scatters of cloud data in Figure 2, and the lengths of the error bars, show how meteorological noise can easily mask the signal of the cloud response to FD events [*Voiculescu et al.*, 2006]. This is probably why some previous investigators did not detect the full meteorological impact of FDs, and offered their negative results as evidence against the reported link between cosmic ray flux and low cloud cover. For example, *Sloan and Wolfendale* [2008] used the ISCCP data, for which the error bars are particularly large. For MODIS the error bars are smaller, but while we select only 13 FDs in the period 2000–2007, *Kristjánsson et al.* [2008] used about 22 FDs. As a result their data were dominated by weak FDs that would be plotted to the left of our data in Figure 2b, in a region where uncertainties due to variations in meteorology are much greater than the FD signal.

[10] The observed change in aerosols (Figures 1 and 2) can be related to the drop in CWC and LWCF by a loss of the fine aerosols <250 nm that in normal circumstances would have grown into cloud condensation nuclei of $\approx$0.5 μm. Some models of aerosol growth have suggested timescales of the order of several days [*Russell et al.*, 1994; *Arnold*, 2006]. There is observational and experimental evidence that cosmic rays facilitate the formation of ultrafine 10–30 nm sulfuric acid aerosols within a few hours. In the experiment and observations over land close to the surface the condensable vapour concentrations are typically higher than the corresponding values over the oceans, and result in a faster growth rate [*Kulmala et al.*, 2004; *Svensmark et al.*, 2007]. These particles (initially too small to be seen by AERONET) then slowly grow into CCN during the course of some days, mainly by recruiting condensable vapors [*Russell et al.*, 1994]. Our aerosol results can be interpreted as a reduction in the nucleation of ultrafine aerosols, leading to a progressive reduction in CCN that shows up indirectly in the changes in CWC and LWCF about a week after the GCR minimum. Observations are strongly divided on the influence of aerosols on CWC, mainly because meteorological as well as microphysical conditions are involved. Nevertheless, theoretical models suggest that CWC should increase with CCN [*Ackerman et al.*, 2004], in agreement with the present observation. In contrast the LWCF is less ambiguous [*Ackerman et al.*, 2004], where an increase in CCN results in an increase in droplet number and a decrease in droplet size, resulting in less drizzle, longer cloud lifetime, and an increase in cloud fraction.

[11] The response in CWC for the larger events is of the order 7%. For an FD strength of 100% in Figure 2 the change in cloud fraction (ISCCP and MODIS) is of the order 4% ± 2% which is slightly larger than the changes observed during a solar cycle of ≈2% [*Marsh and Svensmark*, 2000]. Our study further indicated that other solar phenomena related to the coronal mass ejections, including changes in total solar irradiance (TSI) or UV and X-ray bursts from flares, are not well correlated with the strength of FDs.

[12] A radically different interpretation of meteorological responses to FDs [*Tinsley*, 2008] invokes effects of the downward ionosphere-earth current density J_z. Impacts of FDs on winter storm vorticity were reported by *Tinsley and Deen* [1991], and when *Todd and Kniveton* [2004] examined ISCCP cloud data for 32 FDs (1983–2000) and noted immediate reductions of high level cloud (especially over the Antarctic plateau in winter) *Tinsley* [2008] interpreted these changes as correlating with J_z. Such processes might conceivably affect cloud water content and aerosol concentrations several days later, but our analysis neither detects nor excludes a role for the J_z mechanism.

6. Conclusion

[13] Our results show global-scale evidence of conspicuous influences of solar variability on cloudiness and aerosols. Irrespective of the detailed mechanism, the loss of ions from the air during FDs reduces the cloud liquid water content over the oceans. So marked is the response to relatively small variations in the total ionization, we suspect that a large fraction of Earth's clouds could be controlled by ionization. Future work should estimate how large a volume of the Earth's atmosphere is involved in the ion process that leads to the changes seen in CCN and its importance for the Earth's radiation budget. From solar activity to cosmic ray ionization to aerosols and liquid-water clouds, a causal chain appears to operate on a global scale.

[14] **Acknowledgments.** We thank H. Spliid for valuable discussions regarding the statistics, and HS thanks Nigel Calder for helpful comments. SSM/I data are produced by Remote Sensing Systems and sponsored by the NASA Earth Science REASoN DISCOVER Project. Data are available at www.remss.com. We thank the Principal Investigators and staff of AERONET http://aeronet.gsfc.nasa.gov for establishing and maintaining the sites used in this investigation. The ISCCP D1 data were obtained from the International Satellite Cloud Climatology Project web site http://isccp.giss.nasa.gov, and the MODIS data from http://modis.gsfc.nasa.gov.

References

Ackerman, A. S., M. P. Kirkpatrick, D. E. Stevens, and O. B. Toon (2004), The impact of humidity above stratiform clouds on indirect aerosol climate forcing, *Nature*, *432*, 1014–1017, doi:10.1038/nature03174.

Arnold, F. (2006), Atmospheric aerosol and cloud condensation nuclei formation: A possible influence of cosmic rays?, *Space Sci. Rev.*, *125*, 169–186.

Bazilevskaya, G. A., et al. (2008), Cosmic ray induced ion production in the atmosphere, *Space Sci. Rev.*, *137*, 149–173.

Dickinson, R. E. (1975), Solar variability and the lower atmosphere, *Bull. Am. Meteorol. Soc.*, *56*, 1240–1248.

Harrison, R. G., and D. B. Stephenson (2006), Empirical evidence for a nonlinear effect of galactic cosmic rays on clouds, *Proc. R. Soc. London. Ser. A*, *462*, 1221–1233, doi:10.1098/rspa.2005.1628.

Hilary, C. V. (2000), Coronal mass ejections and Forbush decreases, *Space Sci. Rev.*, *93*, 55–77.

Kniveton, D. R. (2004), Precipitation, cloud cover and Forbush decreases in galactic cosmic rays, *J. Atmos. Sol. Terr. Phys.*, *66*, 1135–1142, doi:10.1016/j.jastp.2004.05.010.

Kristjánsson, J. E., and J. Kristiansen (2000), Is there a cosmic ray signal in recent variations in global cloudiness and cloud radiative forcing?, *J. Geophys. Res.*, *105*, 11,851–11,863.

Kristjánsson, J. E., C. W. Stjern, F. Stordal, A. M. Fjæraa, G. Myhre, and K. Jónasson (2008), Cosmic rays, cloud condensation nuclei and clouds: A reassessment using MODIS data, *Atmos. Chem. Phys.*, *8*, 7373–7387.

Kulmala, M., H. Vehkamki, T. Petj, M. Dal Maso, A. Lauri, V. M. Kerminin, W. Birmili, and P. H. McMurry (2004), Formation and growth rates of ultrafine atmospheric particles: A review of observations, *J. Aerosol Sci.*, *35*, 143–176.

Marsh, N. D., and H. Svensmark (2000), Low cloud properties influenced by cosmic rays, *Phys. Rev. Lett.*, *85*, 5004–5007.

Ney, E. R. (1959), Cosmic radiation and the weather, *Nature*, *183*, 451–452.

Rossow, W. B., and R. A. Schiffer (1991), ISCCP cloud data products, *Bull. Am. Meteorol. Soc.*, *72*, 2–20.

Russell, L. M., S. N. Pandis, and J. H. Seinfeld (1994), Aerosol production and growth in the marine boundary layer, *J. Geophys. Res.*, *99*, 20,989–21,003.

Schuster, G. L., O. Dubovik, and B. N. Holben (2006), Angstrom exponent and bimodal aerosol size distributions, *J. Geophys. Res.*, *111*, D07207, doi:10.1029/2005JD006328.

Sloan, T., and A. Wolfendale (2008), Testing the proposed causal link between cosmic rays and cloud cover, *Environ. Res. Lett.*, *3*, 024001, doi:10.1088/1748-9326/3/2/024001.

Svensmark, H., and E. Friis-Christensen (1997), Variation of cosmic ray flux and global cloud coverage: A missing link in solar-climate relationships, *J. Atmos. Sol. Terr. Phys.*, *59*, 1225–1232.

Svensmark, H., J. O. P. Pedersen, N. D. Marsh, M. B. Enghoff, and U. I. Uggerhj (2007), Experimental evidence for the role of ions in particle nucleation under atmospheric conditions, *Proc. R. Soc. London, Ser. A*, *463*, 385–396, doi:10.1098/rspa.2006.1773.

Tinsley, B. A. (2008), The global atmospheric electric circuit and its effects on cloud microphysics, *Rep. Prog. Phys.*, *71*, 066801, doi:10.1088/00344885/71/6/066801.

Tinsley, B. A., and G. W. Deen (1991), Apparent tropospheric response to MeV-GeV particle flux variations: A connection via electrofreezing of supercooled water in high-level clouds?, *J. Geophys. Res.*, *96*, 22,283–22,296.

Todd, M. C., and D. R. Kniveton (2004), Short-term variability in satellite-derived cloud cover and galactic cosmic rays: Update, *J. Atmos. Sol. Terr. Phys.*, *66*, 1205–1211.

Voiculescu, M., I. G. Usoskin, and K. Mursula (2006), Different response of clouds to solar input, *Geophys. Res. Lett.*, *33*, L21802, doi:10.1029/2006GL027820.

Weng, F., N. Grody, R. Ferraro, A. Basist, and D. Forsyth (1997), Cloud liquid water climatology from the Special Sensor Microwave/Imager, *J. Clim.*, *10*, 1086–1098.

Wentz, F. J. (1997), A well-calibrated ocean algorithm for SSM/I, *J. Geophys. Res.*, *102*, 8703–8718.

T. Bondo, H. Svensmark, and J. Svensmark, National Space Institute, Technical University of Denmark, Juliane Marie Vej 30, D-2100 Copenhagen Ø, Denmark. (tb@space.dtu.dk; hsv@space.dtu.dk; jacobsvensmark@gmail.com)

Cosmic ray decreases affect atmospheric aerosols and clouds: Auxiliary material

Henrik Svensmark,[1] Torsten Bondo,[1] and Jacob Svensmark[1]

1. Variations in the Primary Cosmic Ray Spectrum Caused by FD

To determine the change in ionization in the atmosphere during a Forbush decrease (FD) variations of the primary cosmic ray spectrum at the top of the Earths atmosphere must be determined. Therefore cosmic ray responses in neutron monitors (NM) and in muon telescopes are studied. Different detectors give information to different parts of the cosmic ray energy spectrum, which will be used to estimate the variation of the primary spectrum. The analysis combines data from the global network of 130 NM (1) and from the Multi-Directional Cosmic-Ray Muon Telescope at Nagoya(2).

NM count mainly the neutrons that are produced in the secondary shower events following the nuclear interactions of the primary cosmic ray particles with the atoms high in the Earth's atmosphere. Count rates and their variations during a FD depend on the altitude and geomagnetic position of the instrument. The counts that a NM registers can be expressed as

$$N(t) = \int_{P_c}^{\infty} S(h,P)J(P,t)dP, \tag{1}$$

where P_c is the cutoff rigidity due to the geomagnetic field,$S(h,P)$ is the yield function (the average number of counts in the NM due to a primary cosmic ray particle of rigidity P), h is the height of the NM above sea level, and $J(P,t)$ is the differential rigidity spectrum at 1 AU as a function of time t.

From the above equation one can define P_m, the median rigidity as

$$N(t)/2 = \int_{P_c}^{P_m} S(h,P)J(P,t)dP, \tag{2}$$

i.e. the rigidity below which the NM registers half its counts. The median rigidity characterizes a NM, since it depends on the location. One problem with this measure is that it changes through the solar cycle. However, this is not a serious matter in the present study, since the FD with which we are dealing are most frequent around solar maximum. We elect to use the median rigidity at solar maximum for all NM. The median rigidity of the NM data is based on vertical cut-off rigidity estimates and ranges from ≈10 GV (South Pole stations) to ≈47 GV (Ahmedabad, India). The 17 different viewing angles of the Multi-directional Nagoya detector represent 17 different paths of the muons through the atmosphere and therefore 17 different response functions. The median rigidity range of the Muon Telescope ranges from 60 to 119 GV (2). So the present work covers a range from 10 GV to 119 GV in median rigidity, and the results are based on daily averages. Figure S1 shows how the relative changes in counts vary across that range of median rigidities.

The availability of data on clouds from the SSM/I instruments of the Defence Meteorological Satellite Program, since 1987, defines the period 1987-2007 over which FD are studied. (AERONET data on aerosols are available since 1998.) During the period of interest FD are identified as a sudden decrease in the neutron counts followed by a recovery over days to weeks. First the day at which the minimum counts, $N(i_{\min})$, occurs is found. Then a reference level of the neutron counts is found prior to the minimum of the FD defined as

$$N_R = \frac{1}{14}\sum_{i_{min}-15}^{i_{min}-1} N(i), \tag{3}$$

i.e. a 14 day average of the neutron counts ending 1 day before the minimum. From this the change in neutron counts is defined as

$$\Delta N = N_{i_{min}} - N_R, \tag{4}$$

and the relative change is defined as

$$\delta N = \frac{\Delta N}{N_R}. \tag{5}$$

Table S1 shows the 26 largest FD events identified in this way. For comparison see (Kudela 2004) (3).

The 130 NM located all over the world, at different altitudes and with different cutoff rigidities, are used to determine the the above relative change for a particular FD $\delta N_{i,k}$, where the index i identifies the NM, and index k the FD. For each FD the relative change in $\delta N_{i,k}$ is related to the station's median rigidity $(P_m)_i$, and a function

$$n_k = A_k (P_m)^{-\gamma_k}, \tag{6}$$

where A_k and γ_k are determined by minimizing the least square deviation to the data . The form of the above function is regularly used and to a good approximation seen in FD modulations of energy spectra (4).

It is possible to relate the foregoing NM responses to changes in $J(P,t)$, the differential rigidity spectrum at 1 AU, by the relation $P_m \rightarrow P$ such that

$$\frac{\delta J_k}{J_k} \approx A_k P^{-\gamma_k}. \tag{7}$$

Figure S2 shows an exact calculation where the primary spectrum is assumed of the form in Eq. (7). Using a yield function for an NM-64 neutron monitor (5) it is therefore possible, using Eq. (2) and Eq. (7) and Eq. (5), to calculate both P_m and $\delta N/N$ as a function of a station's cutoff

rigidity and altitude. The figure demonstrates for a particular FD that the approximation Eq. (7) is satisfactory to within 10%. The main errors are for the lower rigidities but those energies are not important for the ionization in the lower troposphere.

In some studies the force field approximation (6) is used to calculate the heliospheric modulation of cosmic rays (7). But this equation does not describe shocks and diffusive fronts in the heliosphere which characterize coronal mass ejections. Therefore the approach involving the median rigidity is preferred.

2. Variation in the Atmospheric Ionization

With the variation in the differential rigidity spectrum known via Eq. (7) it is possible to calculate the resulting change in the ionization down through the atmosphere. This is done by a Monte Carlo simulation of incoming CR energies and the resulting shower structure of secondary particles. The evolution of the shower is calculated by the CORSIKA program (8) where a primary proton of kinetic energy T and an incident angle to zenith $0 \leq \alpha \leq 70$ deg. are the initial conditions for the cascade. For each particle energy in the range 1 - 1000 GeV, 10,000 showers are calculated, and $I(P,h)$, the average ionization energy deposited at various heights in the atmosphere, is obtained. It is then possible to derive the ion production in the atmosphere as

$$q(h) = \int_{P_c}^{\infty} I(P,h) J(P) dP, \tag{8}$$

where $I(P,h)$ is the ionization at height h caused by a particle with rigidity P. The change in ionization due to a FD is then given by

$$\delta q(h) = \int_{P_c}^{\infty} I(P,h) A_k P^{-\gamma_k} J(P) dP. \tag{9}$$

Figures S3a and S3b show the ionization production as a function of the altitude (9). The differential energy spectrum used in the calculations is based on the Bess spectrometer observations of cosmic rays close to solar minimum (10). The black curve (Figure S3a) is the solar minimum curve and the red curve is for the solar maximum, based on A_{SC} and γ_{SC} in the caption of Table S1. The blue curves are the reduction in ion production due to the FD and based on the the A and γ in Table S1. The lowest curve is the exceptional event in October 2003. Figure S3b contains the same information but now the reduction in ion production is normalized with the reduction from solar max to solar min, i.e. the difference between the black curve and the red curve.

3. Examples of Individual Events

The paper makes use of data on aerosols and clouds averaged for 5 FD events. Doing so averages out some of the meteorological noise, so that the impact of GCR reductions is plainer to see. On the other hand, it might be objected that the choice of events is untypical, or that a single FD showing an accidentally large effect dominates the average. We have examined many plots for individual events, and for all of the strongest ones (judged by the change in low-altitude ionization) the features shown in averaged data are repeated. To illustrate this, we show in Figure S4 the loss of cloud liquid water in each of the first six events in Table 1.

References and Notes

1. NM data can be obtained from ftp://cr0.izmiran.rssi.ru/

2. We acknowledge the Cosmic Ray Section, Solar-Terrestrial Environment Laboratory, Nagoya University who provided the muon data. Data can be obtained from http://www.stelab.nagoya-u.ac.jp/ste-www1/div3/muon/muon1.html

3. K. Kudela, *J. Atmos. & Solar Terr. Phys.*, **66**, 1121 (2004).

4. H. S. Ahluwalia and M. Fikani, *J. Geophys. Res.* **112**, 8105 (2007).

5. J. M. Clem and L. I. Dorman, *Space Sci. Rev.*, **93**, 335 (2000).

6. R. A. Caballero-Lopez and H. Moraal, *J. Geophys. Res.*, **109**, A01101 (2004).

7. Usoskin *et al.*, *J. Geophys. Res.*, **110**, A12108 (2005).

8. More information about CORSIKA can be found at http://www-ik.fzk.de/corsika/

9. For general introduction to ionization in the atmosphere see for example: G. A. Bazilevskaya *et. al*, *Space Sci. Rev.*, DOI 10.1007/s11214-008-9339-y.

10. T. Sanuki et al., *Astro. Phys. J.*, **545**, 1135 (2000).

Figure 1. Relative changes of counts by neutron monitors and the Nagoya Muon Telescope are here plotted against the median rigidity of the stations P_m, for a few FD shown in color. The colored curves are the fitted functions of the form of Eq. (7). The black curve is the fit to the change from solar minimum to solar maximum.

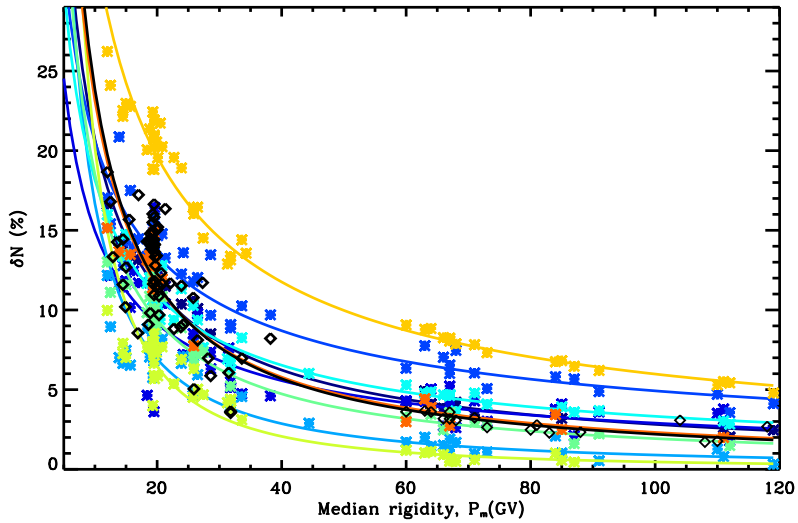

Figure 2. The relative changes in cosmic ray counts diminish as the energies of the primary cosmic ray particles increase. For an explanation of the construction of this plot, see text.

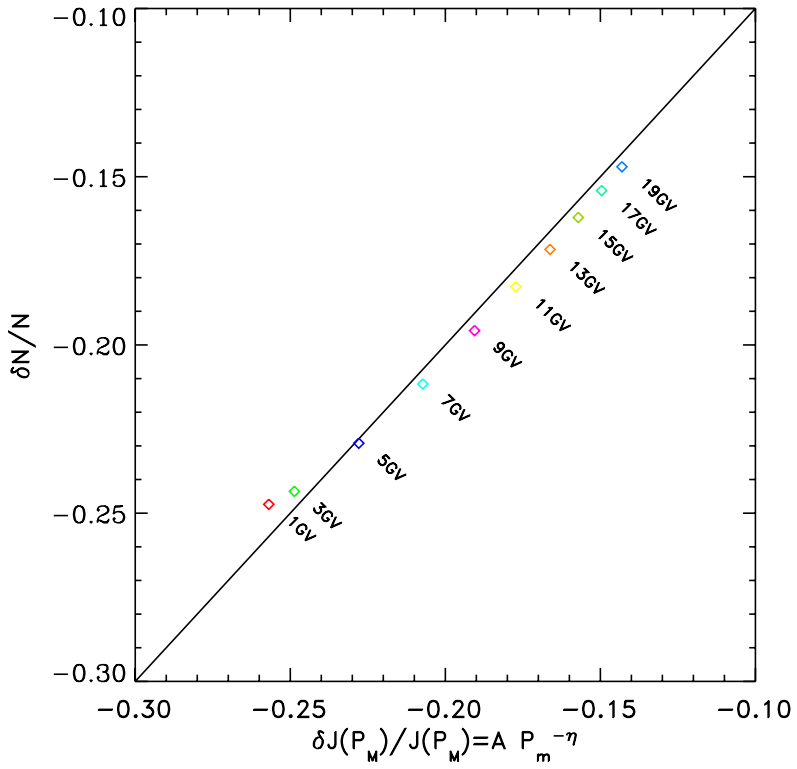

Figure 3. (a) The absolute ion production in the atmosphere (US standard) as a function of altitude. The black curve is the ion production under solar min conditions, and the red curve is during solar max corresponding to a 45 deg. latitude and a cutoff rigidity of 6 GV. The individual blue lines show the depression relative to the solar min conditions due to the FD events in Table S1. The lowermost line is for the very strong FD event in October 2003. (b) The individual FD normalized to the solar cycle variation (the difference between the black curve and the red curve in Figure S3a). Of special interest in the paper are the changes in the lowermost 3 km. Dates are given for the six strongest events at low altitude.

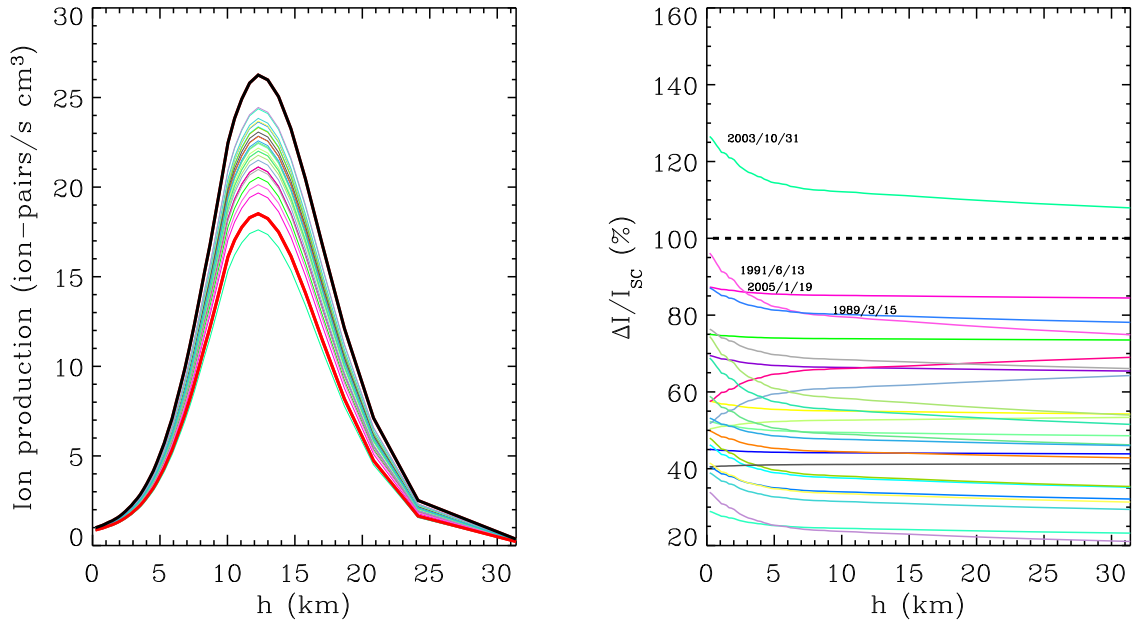

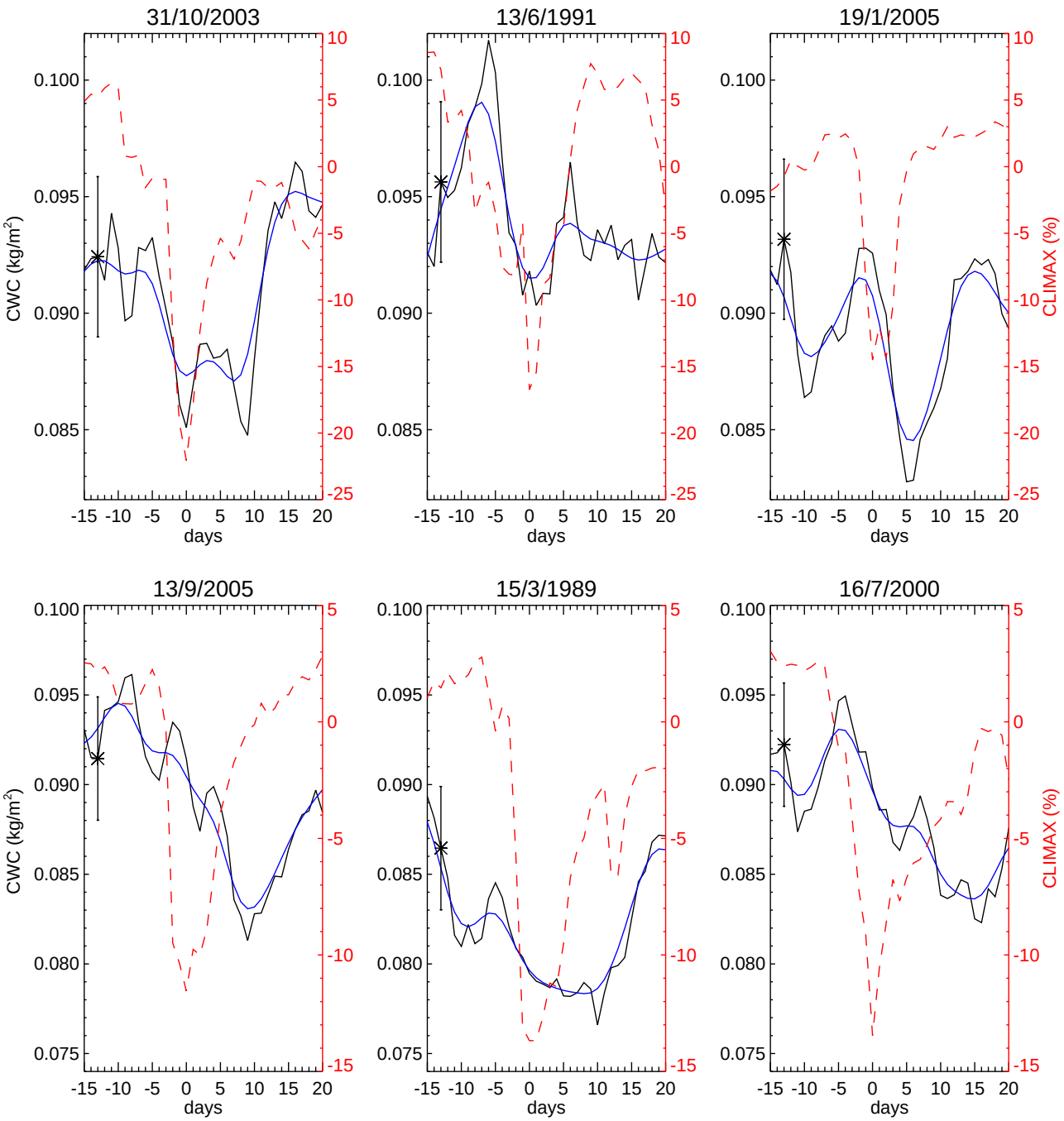
31/10/2003
13/6/1991
19/1/2005
13/9/2005
15/3/1989
16/7/2000
CWC (kg/m^2)
CLIMAX (%)
days

Figure 4. The impact of coronal mass ejections on the liquid water content of clouds is plotted for the six strongest events (order numbers 1-6 in Tables 1 and SM1). The red broken lines show Forbush decreases (FDs) in the influx of galactic cosmic rays (GCRs) as recorded by neutron counts at Climax, Colorado. Each plot covers the period from 15 days before to 20 days after the date of the GCR minimum. The black curves show the daily mean liquid water content of clouds (CWC) over the world's oceans as measured by SSM/I. The blue curves are Gaussian smoothed curves with a width of 2 days and total length of 10 days. The error bar denotes the one sigma natural variability.

Evidence for the Role of Ions in Aerosol Nucleation

Martin B. Enghoff,*,† Jens Olaf Pepke Pedersen,† Torsten Bondo,† Matthew S. Johnson,‡ Sean Paling,§ and Henrik Svensmark†

Center for Sun-Climate Research, National Space Institute, Technical University of Denmark, DK-2100 Copenhagen, Denmark; Copenhagen Center for Atmospheric Research, Department of Chemistry, University of Copenhagen, DK-2100 Copenhagen, Denmark; and Department of Physics and Astronomy, Sheffield University, Sheffield S10 2TN, U.K.

Received: April 25, 2008

Aerosol nucleation has been studied experimentally in purified, atmospheric air, containing trace amounts of water vapor, ozone, and sulfur dioxide. The results are compared with model calculations. It is found that an increase in ionization by a factor of 10 increases the production rate of stable clusters by a factor of ~3, probably due to ion-induced nucleation.

1. Introduction

The role of ions in producing aerosols in the earth's atmosphere is a very active area of research. Atmospheric[1−5] and experimental[6] observations have shown that the nucleation of aerosol particles can occur under conditions that cannot be explained by classical nucleation theory. Several ideas have been put forward to solve this nucleation problem, e.g., ion-induced nucleation[7−9] and ternary nucleation.[5] However, experimental investigations exploring the role of ions in particle production are scarce and often in conditions far removed from those relevant for the lower part of the atmosphere.[10−14]

Recently, experimental work[15] demonstrated that ions, produced by cosmic rays in the atmosphere, are likely to play an important role in the production of new aerosol particles. The mechanism whereby energetic cosmic rays can promote the production of cloud condensation nuclei at low altitudes constitutes a link between cosmic rays and the earth's climate, and there is thus a need to corroborate the results in a different experiment. The present results, which are obtained in the same laboratory, but using a new setup with a much smaller (50 L) reaction chamber, confirm the previous conclusions, which were obtained with a 7 m^3 reaction chamber.

2. Experimental Methods

The present experiments were conducted in a cylindrical reaction chamber (length 100 cm and diameter 25 cm) made of electropolished stainless steel. One end of the chamber consists of a thin Teflon foil to allow transmittance of UV light. The chamber was continuously flushed with air at a rate of 3.2−3.3 L/min to maintain steady-state conditions and allow for mixing. The air consisted of atmospheric air, compressed and dried with an oil-free compressor and filtered using active charcoal, citric acid, and 10 nm as well as 3 nm filters. A mixture of ozone, SO_2, and water vapor was added to the air flow before entering the chamber. The air entered through a tube protuding about 80 cm into the chamber from the opposite end of the Teflon window, and sampling also took place at the tube-insertion end.

The air was humidified by circulating deionized water through a GoreTex tube inserted into the air stream. This allowed the relative humidities to be varied from 5 to 90%. Sulfur dioxide was added to the chamber from a 5 ppm mixture of SO_2 in dry air (Strandmøllen), and ozone was introduced by flowing air through an ozone generator. SO_2 and O_3 flowed through a separate tube with a 3 nm particle filter and was joined with the main air flow at the very entrance to the chamber.

The pressure in the chamber was held at 1 mbar above atmospheric pressure, and the temperature was that of the room, which was temperature stabilized.

A mercury discharge lamp placed about 135 cm from the Teflon window emitted UV radiation primarily at 253.7 nm, which was collimated by a black, 80 mm, $^1/_4$ in. pore size honeycomb wall. This initiated a photochemical reaction where ozone was photolyzed to produce OH radicals, and by reaction with sulfur dioxide and subsequently with oxygen and water, sulfuric acid was produced to begin nucleation. The participation of trace amounts of other compounds (which may not be trapped by the filters) in the nucleation process can, however, not be ruled out.

Temperature, pressure, and relative humidity were monitored as well as ozone and sulfur dioxide concentrations using trace gas analyzers at the 0.1 ppb (Teledyne model 400A) and 0.05 ppb (Thermo model 43 CTL) level, respectively.

Ions in the chamber were produced by cosmic radiation and the decay of the natural abundance of radon. In addition to this, the production of ion pairs could be increased by a 35 MBq Cs-137 gamma source. This source was placed at the long side of the chamber, ~140 cm from the center. The resulting ionization was measured by a Gerdien tube[16] and varied from 770 ion pairs/cm^3 without the gamma source to 3700 ion pairs/cm^3 with the source fully open. The strength of the source could be varied by placing pieces of lead in front of the source. For this experiment we either had the source fully open, fully closed (10 cm of lead), or covered by 1 cm of lead (corresponding to approximately a 50% reduction). From the measured ion densities and other known parameters for the chamber the ion pair production from cosmic radiation and radon is estimated to about 3.7 cm^{-3} s^{-1}. With the gamma source this number increases to about 35 cm^{-3} s^{-1}.

The resulting aerosol production was measured by a TSI Ultra Fine Condensation Particle Counter model 3025A.

* To whom correspondence should be addressed.
† Technical University of Denmark.
‡ University of Copenhagen.
§ Sheffield University.

10.1021/jp806852d CCC: $40.75
Published on Web 09/12/2008

The previous experiments were conducted in a 7 m^3 reaction chamber made of Mylar and Teflon. Inside the chamber two 1.7×1.7 m^2 electrodes were placed to allow for the generation of an electric field, meant to remove ions. External UV lamps were used to initiate the photochemistry in the chamber in a way similar to that described for the present setup. Further details can be found in the paper describing the experiment.[15]

The experiments described in this paper were conducted by allowing SO_2, O_3, the temperature (T), and the relative humidity (RH) to settle into a steady state in the chamber. Prior to the measurements, the chamber was cleansed using UV and ozone for 1 week, followed by 6 days of conditioning before the measurements became reproducible. Typically T was held around 23 °C and RH at 50%. Two series of measurements were performed: the first one (I) with SO_2 set to 4 ppb and O_3 to 23 ppb and a second series (II) with SO_2 set to 30 ppb and O_3 to 68 ppb. Atmospheric levels of SO_2 range from ~20 ppt in the marine surface layer to ~1.5 ppb in polluted areas, and O_3 concentrations lie between 20 and >200 ppb. Whereas our O_3 values are within the range of the atmosphere, our lowest SO_2 values (series I) are somewhat above atmospheric levels. However, with the current setup lower concentrations of SO_2 would lead to particle concentrations below the detection level of the particle counter.

In both series a measurement was initiated with the production of a "burst" of H_2SO_4 following exposure of the chamber to UV light, resulting in the production of aerosols. The peak aerosol concentration lasted for a few minutes before decaying exponentially due to wall and dilution losses. Figure 1 shows a typical measurement of the particles by the condensation particle counter, which measures particles larger than ~3 nm. An initial steep rise in aerosol number to a maximum is followed by a slower decay. The small size of the reaction chamber allowed for a return to initial conditions after about 1.5 h, and the cycle could be repeated with another burst of UV light. In series I the chamber was illuminated for 11 min with 110 min between each measurement, and in series II there was 4 min of exposure to UV at 10 times lower intensity than in series I with 90 min between each measurement.

As a measure of the number of particles produced we integrate the peak over time by adding count numbers from each individual measurement. The results from the two continuous measurement series can be seen in Figure 2, where the integrated peak values are shown as a function of time. During each series the ion density in the reaction chamber was varied by changing the intensity of the Cs-137 source as described above.

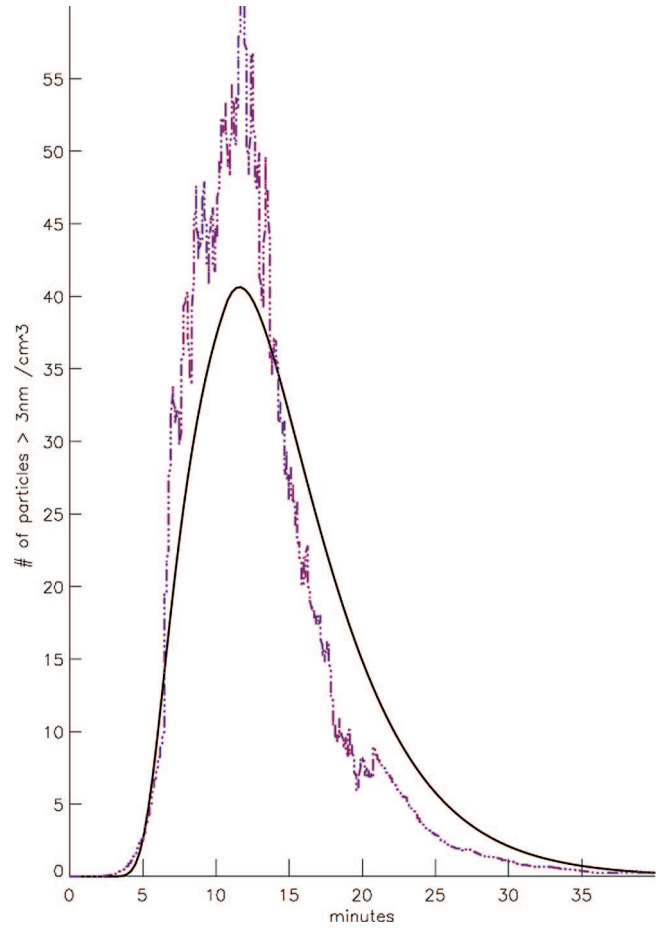

Figure 1. Example of measurement of the particles by the condensation particle counter (dashed line). Time is measured after start of the UV illumination. Only particles larger than ~3 nm are detected by the particle counter. The solid line is the result of a model that generates the same number of particles (see text).

3. Results and Discussion

It is seen from Figure 2 that there is clear dependency of the number of particles on the level of radiation. For series I the mean value of the integrated peak is ~19 600 with no exposure to the gamma source and ~53 600 with full exposure. For series II the value is ~5800, ~11 300, and ~19 500 for no exposure, 1 cm of lead in front of the source, and full exposure, respectively.

A numerical model of neutral sulfuric acid particle growth has been developed to aid the interpretation of the experimental results and to examine the dependence of the particle production at 3 nm to changes in the sulfuric acid gas concentration and particle nucleation rates.

The model is based on the general dynamic equation (GDE) which is a partial differential equation for aerosol particle growth [ref 17, Chapter 12]. A sectional method is used to solve the GDE to determine the number distribution n. Separate bins represent different sizes of the molecular clusters expressed as the number of sulfuric acid molecules in the cluster. The size of the cluster in a given bin increases stepwise by 1 molecule up to 70 molecules (~3.5 nm cluster diameter), where the cluster size is then increased by larger steps, as shown in eq 1. With i being the bin number, $nc(i)$ the size of the cluster in bin i, and $nmax$ a factor used to determine the largest cluster described in the model, the cluster sizes are defined by

$$nc(i) = [0, 1, 2, ..., 69, 70, 75, 85, 100, 120, 145, 175, 210, 250, 250 \times 1.2^{j+1}], \quad j \in [0, nmax] \quad (1)$$

Adopting equivalent notation to that of Lovejoy et al.,[18] the discrete partial derivative of the neutral sulfuric acid cluster distribution function for bin i, $n(i)$, is now given by

$$\frac{\partial n(i)}{\partial t} = \frac{k^c_{i-1}[H_2SO_4]n(i-1)}{(nc_i - nc_{i-2})/2} - \frac{k^c_i[H_2SO_4]n(i)}{(nc_{i+1} - nc_{i-1})/2} + 0.5\sum_l \sum_j k^e_{j,l} n(j)n(l) \frac{(nc_l + nc_j) - nc_{i-1}}{(nc_i - nc_{i-1})} \delta_{(n_l+n_j),[nc_{i-1},nc_i]} + 0.5\sum_l \sum_j k^e_{j,l} n(j)n(l) \frac{nc_{i+1} - (nc_l + nc_j)}{(nc_{i+1} - nc_i)} \delta_{(n_l+n_j),[nc_{i+1},nc_i]} - \lambda_{par} n(i) \quad (2)$$

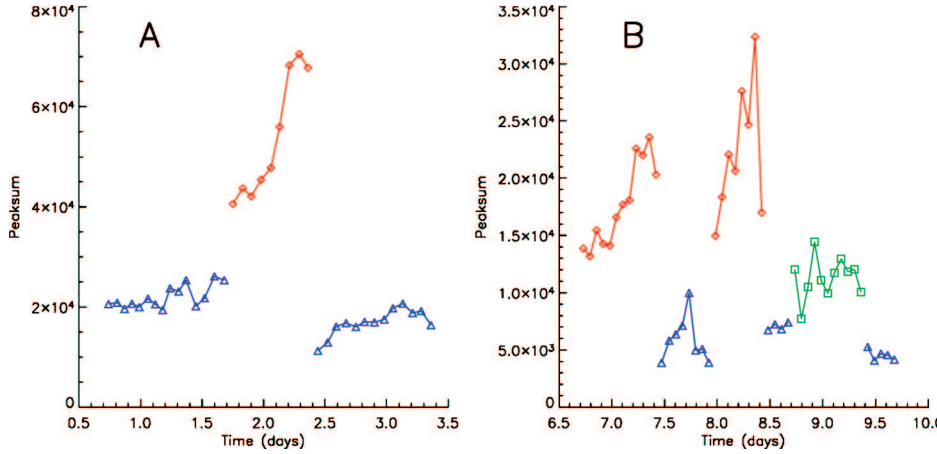

Figure 2. Results from the two measurements series—the integrated peak is shown as a function of time. Blue triangles correspond to measurements without the gamma source (ion production ~3.7 cm^{-3} s^{-1}), red diamonds are with the source open (ion production ~35 cm^{-3} s^{-1}), and green squares are with 1 cm of lead in front of the source (intermediate ion production). RH was ~50% and $T \sim 23$ °C for both series. (A) ~4 ppb SO_2 and ~23 ppb O_3 with 11 min of UV and 110 min between each measurement. (B) ~30 ppb SO_2 and ~68 ppb O_3 with 4 min of exposure to UV at 10 times lower intensity than in the first series and 90 min between each measurement.

The first term is the production of $n(i)$ from the previous bin by the condensation of a sulfuric acid molecule. The second term is similarly the loss due to condensation. The next two terms represent the coagulation of the individual clusters. Here the delta functions and the fractions take the increasing sizes of the bins into account and make sure to fractionalize the coagulated particles into the correct bins. The last term is a loss term used to account for losses of particles to the wall. Notice that evaporation is not considered since the particles are considered to be stable.

The condensation coefficients k_i^c are found according to Laakso et al.[19] with a value of the mass accommodation coefficient of 1,[20] where the mean free paths used to determine k_i^c are determined from Lehtinen et al.[21] The cluster diameter as a function of bin size must also be found. This is nontrivial since the mole fraction of water in the cluster changes with cluster growth. Here it is assumed that an initial sulfuric acid particle is wet, and the results from Seinfeld and Pandis [ref 17, p 486] are used to determine the cluster diameter and mole fraction of water as a function of number of sulfuric acid molecules. Having determined the particle diameter, the individual diffusion coefficients used in k_i^c are given by Poling et al.[22]

The coagulation coefficients are determined from Laakso et al.[19] and can be used in all growth regimes from diameters of a few angstroms to sizes larger than 1 μm. The model does not go into the chemistry of the nucleation but assumes that stable clusters with a size of five sulfuric acid molecules are formed at a rate s.

In each time step the sulfuric acid concentration is found by solving the rate equation

$$\frac{d[H_2SO_4]}{dt} = P_{H_2SO_4} - \lambda_{gas}[H_2SO_4] - [H_2SO_4]\sum_i n_i k_i^c \quad (3)$$

The first term, $P_{H_2SO_4}$, is the production term of sulfuric acid in cm^{-3} s^{-1}, and the second term is a loss term used to account for losses of gas molecules to the wall and dilution (λ_{gas} is the loss rate). The last term represents the loss of gas molecules due to condensation unto clusters, where n_i is the cluster concentration.

The model is initally run with a constant stable cluster production s, meaning that particles are being put into bin 5 at a constant rate. This ensures that steady-state conditions are obtained before turning on the sulfuric gas production $P_{H_2SO_4}$. The experimental data in series I and II are then modeled by turning on the production rate of sulfuric acid $P_{H_2SO_4}$ (for 11 and 4 min, respectively). An example is shown in Figure 1, where the model curve has been fitted to the experimental data for a set value of s and $P_{H_2SO_4}$.

The values of $P_{H_2SO_4}$ will lead to different sulfuric acid gas concentrations. By running the model, it was observed that the sulfuric acid gas concentration is independent of s for the range of values used. This means that the peak sulfuric acid concentration obtained for a particular production rate is also independent of s.

The sulfuric acid and particle losses (to walls and dilution) are set to 3.26 min for series I and 2.71 min for series II (determined experimentally from the decay of the aerosol peaks). The relative humidity was fixed at 50% for both series.

The output of each model run is a time series of the particle population adjusted for the counting effiency of the particle counter. Unique values, comparable with the experimental results, are obtained for each set of parameters by integrating the peaks over time.

For series I the model was run with equidistant ds = 0.05 cm^{-3} s^{-1} with s = [0.05, 7.35] cm^{-3} s^{-1} and equidistant d$P_{H_2SO_4}$ = 45 000 cm^{-3} s^{-1} with $P_{H_2SO_4}$ = [6.5 × 10^4, 2 × 10^6] cm^{-3} s^{-1}. For series II ds = 0.05 cm^{-3} s^{-1} with s = [0.05, 5] cm^{-3} s^{-1} and d$P_{H_2SO_4}$ = 90 000 cm^{-3} s^{-1} with $P_{H_2SO_4}$ = [4 × 10^4, 4 × 10^6] cm^{-3} s^{-1}.

Figure 3 shows these values for the two series I (left) and II (right).

The insets in Figure 3 show model results compared to experimental data for selected values of s and peak sulfuric acid gas concentrations and thus show the effect on the experimental signal of changes in these two parameters. The model fits the experimental data in series I rather well, whereas the actual shape of the model results in series II differs more from the shape of the experimentally obtained peaks. A more detailed model including evaporation might improve this. However, for the purpose of determining approximate values of particle and gas concentrations the model is sufficient.

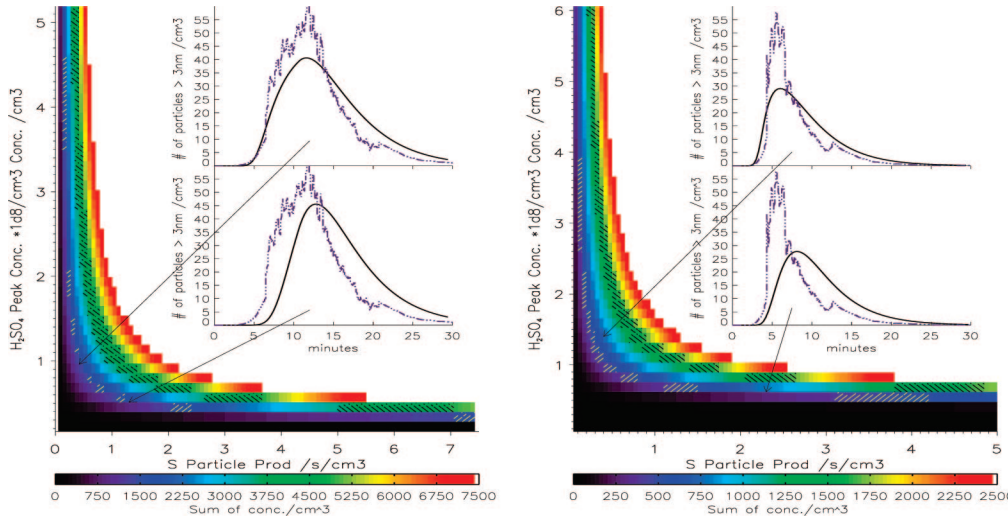

Figure 3. Integrated value of the temporal evolution of the formation of aerosols adjusted for the counting effiency of the particle counter as a function of *s* and sulfuric acid concentration. Left: series I. Right: series II. Hatched with / are the experimental data without sources, and hatched with \ are the experimental data with fully open sources. The experimental data used in this figure are obtained by computing the average of the values in Figure 2 with and without sources and including the 95% confidence interval. The insets shows model results compared to experimental data for selected values of *s* and peak sulfuric acid gas concentrations.

The results show that the number of generated aerosols depend on the level of exposure to the gamma sources—the question is what mechanism controls this. A concern when using γ radiation to ionize the gas is that this may produce additional sulfuric acid directly by radiolysis of water (leading to OH, which reacts with SO_2 and forms H_2SO_4). We can exclude this possibility by looking at the time it takes from when the UV light is turned on in the experiment until the aerosol concentration exceeds a certain level, which we have chosen to be 5 cm^{-3}. An increase in sulfuric acid would cause a faster growth of the particles and thus shorter delay time. In general, this delay time is seen to be reduced when the gamma source is open; however, since there is 7 times more SO_2 in the series II experiment compared to the series I, it would be expected that the relative increase of H_2SO_4 and therefore delay time would be much larger in series II compared to series I. Looking at the relative increase it is, however, 1.31 for series I and 1.35 for series II, i.e., almost identical changes. We thus take this to prove that the observed increase in aerosol production with increased ionization is not due to an increase in sulfuric acid from radiolysis. The delay time and the general shape of the model solution can now be used to constrain the experimental values of *s* and the sulfuric acid concentration. For both series I and II we constrain the sulfuric acid concentration to the range of $C_{H_2SO_4} \approx (0.5-2.5) \times 10^8$ cm^{-3}. This concentration is well below the range where homogeneous nucleation is expected to dominate [ref 17, p 523, Figure 11.11].

Another possible explanation for the results is that the surface properties of the chamber change, such that the loss rate for the particles is reduced or gases are released from the walls. However, no significant change in the loss rate to the walls was observed when the chamber was exposed to the gamma source so this cannot be the explanation either, leaving ion-induced nucleation as the only viable explanation for the observations. For both series, at a given sulfuric acid concentration, an increase in stable cluster production by a factor of ~3 is required to explain the difference between full and no exposure to the gamma source. In this experiment the ion production rate increases by a factor of 10 (from ~4 to ~40 cm^{-3} s^{-1}).

The previous experiments[15] showed a linear dependency of the amount of particles produced on the small ion density and gave an empirical relation between the measured ion concentration and the production rate of new clusters (*s*). According to this relationship ($s = 2.4 \times 10^{-4} n_e$, where n_e is the ion concentration), *s* should go from 0.19 cm^{-3} s^{-1} without exposure to the source to 0.89 cm^{-3} s^{-1} with full exposure. This is well within the limits given by the present results, when the constrained values for the sulfuric acid concentration is used to determine *s*. The increase in cluster production suggested by the previous study, from no to full exposure, is by a factor of 4.8, which is to be compared to the factor of ~3 found in this paper.

4. Conclusions

In conclusion, the present experiment confirms the previous result that ions play a role in nucleating new aerosols in the atmosphere and that the rate of production is sensitive to the ion density. Most likely the aerosols produced in the experiment are formed by sulfuric acid and water, but the participation of other compounds, which may not be removed by the filters, cannot be excluded.

The presence of a penetrating cosmic ray background limits the minimum ionization for which aerosol production can be investigated in our laboratory. An experiment that can be performed under ultralow background radiation conditions is therefore in progress.

Acknowledgment. We thank Freddy Christiansen for help with developing the model.

References and Notes

(1) Hoppel, W. A.; Frick, G. M.; Fitzgerald, J.; Larson, R. E. *J. Geophys. Res.* **1994**, *99*, 443.

(2) Clarke, A. D.; Davis, D.; Kapustin, V. N.; Eisele, F.; Chen, G.; Paluch, I.; Lenschow, D.; Bandy, A. R.; Thornton, D.; Moore, K.; Mauldin, L.; Tanner, D.; Litchy, M.; Carroll, M. A.; Collins, J.; Albercook, G. *Science* **1998**, *282*, 89.

(3) Birmili, W.; Berresheim, H.; Plass-Dülmer, C.; Elste, T.; Gilge, S.; Wiedensohler, A.; Uhrner, U. *Atmos. Chem. Phys.* **2003**, *3*, 361.

(4) Lee, S.-H.; Reeves, J. M.; Wilson, J. C.; Hunton, D. E.; Viggiano, A. A.; Miller, T. M.; Ballenthin, J. O.; Lait, L. R. *Science* **2003**, *301*, 1886.

(5) Kulmala, M.; Pirjola, L.; Mäkelä, J. M. *Nature (London)* **2000**, *404*, 66.

(6) Berndt, T.; Böge, O.; Stratmann, F.; Heintzenberg, J.; Kulmala, M. *Science* **2005**, *307*, 698.

(7) Arnold, F. *Nature (London)* **1980**, *284*, 610.

(8) Raes, F.; Janssens, A.; van Dingenen, R. *J. Aerosol Sci.* **1986**, *17*, 466.

(9) Turco, R. P.; Zhao, J. X.; Yu, F. *Geophys. Res. Lett.* **1998**, *25*, 635.

(10) Bricard, J.; Billard, F.; Madelaine, G. *J. Geophys. Res.* **1968**, *73*, 4487.

(11) Vohra, K. G.; Ramu, M. C. S.; Muraleedharan, T. S. *Atmos. Environ.* **1984**, *18*, 1653.

(12) Nagato, K.; Kim, C. S.; Adachi, M.; Okuyama, K. *J. Aerosol Sci.* **2005**, *36*, 1036.

(13) Kim, C. S.; Adachi, M.; Okuyama, K.; Seinfeld, J. H. *Aerosol Sci. Technol.* **2002**, *36*, 941.

(14) Wilhelm, S.; Eichkorn, S.; Wiedner, D.; Pirjola, L.; Arnold, F. *Atmos. Environ.* **2003**, *38*, 1734.

(15) Svensmark, H.; Pedersen, J. O. P.; Marsh, N. D.; Enghoff, M. B.; Uggerhøj, U. I. *Proc. R. Soc. London A* **2007**, *463*, 385.

(16) Aplin, K. L.; Harrison, R. G. *Rev. Sci. Instrum.* **2000**, *71*, 3037.

(17) Seinfeld, J. H.; Pandis, S. N. In *Atmospheric Chemistry and Physics*, 2nd ed.; Wiley & Sons: New York, 2006.

(18) Lovejoy, E. R.; Curtius, J.; Froyd, K. D. *J. Geophys. Res.* **2004**, *109*, D08204.

(19) Laakso, L.; Mäkelä, J. M.; Pirjola, L.; Kulmala, M. *J. Geophys. Res.* **2002**, *107*, 4427.

(20) Laaksonen, A.; Vesala, T.; Kulmala, M.; Winkler, P. M.; Wagner, P. E. *Atmos. Chem. Phys.* **2005**, *5*, 461.

(21) Lehtinen, K. E. J.; Kulmala, M. *Atmos. Chem. Phys.* **2002**, *3*, 251.

(22) Poling, B. E.; Prausnitz, J. M.; O'Connell, J. P. In *Properties of Gases and Liquids*, 5th ed.; McGraw-Hill: New York, 2001.

JP806852D

Atmos. Chem. Phys. Discuss., 9, 22833–22863, 2009
www.atmos-chem-phys-discuss.net/9/22833/2009/

Atmospheric Chemistry and Physics Discussions

This discussion paper is/has been under review for the journal *Atmospheric Chemistry and Physics (ACP)*. Please refer to the corresponding final paper in *ACP* if available.

Model of optical response of marine aerosols to Forbush decreases

T. Bondo, M. B. Enghoff, and H. Svensmark

National Space Institute, Technical University of Denmark, Copenhagen, Denmark

Received: 18 August 2009 – Accepted: 1 October 2009 – Published: 27 October 2009

Correspondence to: T. Bondo (tb@space.dtu.dk)

Published by Copernicus Publications on behalf of the European Geosciences Union.

Abstract

In order to elucidate the effect of galactic cosmic rays on cloud formation, we investigate the optical response of marine aerosols to Forbush decreases – abrupt decreases in galactic cosmic rays – by means of modeling. We vary the nucleation rate of new aerosols, in a sectional coagulation and condensation model, according to changes in ionization by the Forbush decrease. From the resulting size distribution we then calculate the aerosol optical thickness and Angstrom exponent, for the wavelength pairs 350, 450 nm and 550, 900 nm. For the shorter wavelength pair we observe a change in Angstrom exponent, following the Forbush Decrease, of −6 to +3% in the cases with atmospherically realistic output parameters. For some parameters we also observe a delay in the change of Angstrom exponent, compared to the maximum of the Forbush decrease, which is caused by different sensitivities of the probing wavelengths to changes in aerosol number concentration and size. For the long wavelengths these changes are generally smaller. The types and magnitude of change is investigated for a suite of nucleation rates, condensable gas production rates, and aerosol loss rates. Furthermore we compare the model output with observations of 5 of the largest Forbush decreases after year 2000. For the 350, 450 nm pair we use AERONET data and find a comparable change in signal while the Angstrom Exponent is lower in the model than in the data, due to AERONET being mainly sampled over land. For 550, 900 nm we compare with both AERONET and MODIS and find little to no response in both model and observations. In summary our study shows that the optical properties of aerosols show a distinct response to Forbush Decreases, assuming that the nucleation of fresh aerosols is driven by ions. Shorter wavelengths seem more favorable for observing these effects and great care should be taken when analyzing observations, in order to avoid the signal being drowned out by noise.

ACPD

9, 22833–22863, 2009

1 Introduction

A Forbush Decrease (FD) is a sudden drop in the amount of galactic cosmic rays observed on Earth, due to large Coronal Mass Ejections from the sun (Forbush, 1937; Cane, 2000). The largest of these events cause up to 10–25% changes in the cosmic ray count rate but occur rarely – only about once a year – and typically last from a few days to about a week. A correlation between galactic cosmic rays (controlled by solar activity) and cloud cover has been shown (Marsh and Svensmark, 2003; Harrison and Stephenson, 2006). If this correlation is due to a physical mechanism a response in cloud cover could be expected during or after a Forbush decrease. An investigation of a connection between clouds and cosmic rays on a FD time scale would also be able to narrow down the number of potential explanations for the cloud – cosmic ray connection as no solar parameters (such as total solar irradiance) correlate well with FD Neutron Monitor counts during the span of a Forbush decrease. FD effects in cloud data have been investigated previously (Pudovkin and Veretenenko, 1995; Kniveton, 2004; Todd and Kniveton, 2004; Harrison and Stephenson, 2006; Kristjánsson et al., 2008; Sloan and Wolfendale, 2008; Svensmark et al., 2009) but no definitive conclusion has been reached. Pudovkin and Veretenenko (1995) investigated 65 Forbush decreases from 1969 to 1986 over four latitudinal bands in Russia and found a significant response in cloud cover in the 60–64° band. Todd and Kniveton (2004) found a decrease in high cloud cover over Antarctica, using ISCCP D1 data from 1983 to 2000. They conclude that their result could just as well be due to the uncertainties in polar cloud retrieval as it could be a real signal. Correlations at 20–30° N and 10–20° S also appear when the effects of rainfall are removed (Kniveton, 2004). In Harrison and Stephenson (2006), ground level observations of the diffuse fraction of light due to scattering by particles are found to be affected by Forbush decreases in the period 1968 to 1994. In Tinsley (2008) a review is given of a series of papers investigating how electro-freezing and cloud scavenging also may cause a response in cloud cover to a FD. Kristjánsson et al. (2008) analysed 22 events using MODIS data from pristine Souther Hemisphere

ACPD
9, 22833–22863, 2009

ocean regions. Little significant response in cloud parameters was found even though the correlations improved somewhat by focusing on the six strongest events. Sloan and Wolfendale (2008) found no significant response either. This is in contrast to results from Svensmark et al. (2009) where an epoch analysis of three independent data sets was used to show a decrease in liquid water clouds about 10 days after a FD. These results are explained as a decrease in nucleation mode aerosols growing to affect CCN and cloud cover over a time period similar to the 10 day lag.

Another approach to this issue is to calculate whether it would be plausible to expect a signal at all. Clouds are formed on aerosols and it has been indicated by theory (Arnold, 1980; Laakso et al., 2002; Lovejoy et al., 2004; Yu, 2006), observations (Eichkorn et al., 2002; Lee et al., 2003; Hirsikko et al., 2007; Laakso et al., 2007; Kulmala et al., 2007) and experiments (Kim et al., 1997; Enghoff et al., 2008; Winkler et al., 2008) that ions, formed by cosmic rays, can enhance the formation of these particles. Therefore it can be expected that if a signal in cloud cover, following a Forbush decrease, is to be found, there should also be a signal in the aerosols.

Motivated by the findings in Svensmark et al. (2009) we try to model how such a response would appear in the aerosol optical properties under the assumption that the cluster formation has been modified by the ionization change during the FD. Two parameters are used to describe the optical properties of aerosol populations: Aerosol Optical Thickness (AOT) and the Angstrom exponent (AE). The AOT is being measured routinely throughout the atmosphere by photometers such as it is being done by AERONET (Holben et al., 1998) – a network of aerosol observations covering most of Earth. It is a measure for how much light penetrates the atmosphere at a given wavelength, such that a higher AOT means that less light gets through. Both particle number concentration and radius affects the AOT thus changes in AOT can be interpreted in various ways. The AE (Schuster et al., 2006) is the slope of the line in a $\log(\mathrm{AOT})$ vs $\log(\lambda)$ plot, where λ is the wavelength. Since the AOT at a given λ is more sensitive to particles that are close to λ in size the AE holds information about the size of the observed particle distribution. A major inhibitor to observe FD effects in aerosols

ACPD
9, 22833–22863, 2009

is the existing population of primary aerosols, from pollution, dust storms, sea spray etc. These large particles, which are produced regardless of cosmic rays, is a major sink to freshly nucleated particles (Pierce and Adams, 2007) and can potentially drown out any signal in the aerosol distribution from Forbush decreases. Two recent model papers arrive at different conclusions on the probability of formation of CCN from ultrafine condensation nuclei (Kuang et al., 2009; Pierce and Adams, 2009) which will affect the signal following a FD. This underlines the relevance of further studies on aerosol growth.

We use a basic nucleation and growth model, sensitive to the cosmic ray flux, to simulate the evolution of a particle distribution in marine conditions, during a Forbush event. In order to calculate the optical properties of the particle distribution the growth model is coupled to a Mie Scattering program: Miex (Wolf, 2004). The sea salt optical properties are derived from the optical properties program OPAC (Hess et al., 1998). Finally we compare the modeling results with measurements from AERONET and MODIS (Platnick et al., 2003).

2 Theoretical model

We are interested in determining the changes in the optical properties of a cloud-free marine environment consisting of sulphur gases and sea salt during a Forbush decrease. The theoretical approach is based on 4 steps as illustrated in Fig. 1 and outlined below.

- *Aerosol growth model*: neutral sulphuric acid aerosol growth is simulated in a marine environment where the cluster production is modulated during a FD. In this part three parameters are varied: the gas phase sulphuric acid production rate, the particle loss rate, and the production rate of stable sulphuric acid clusters.
- *Miex part*: the particle distribution as a function of time is input to a Mie Scattering program (Miex), along with the relevant refractive indices, and used to calculate

ACPD
9, 22833–22863, 2009

the extinction coefficients and optical depths.

- *OPAC part*: simultaneously, an optical properties program (OPAC) is used to calculate the optical depth of a fixed sea salt distribution representative for the marine troposphere.
- *Optical properties*: finally, the total optical depth and Angstrom exponent is calculated as a function of time for the combined sea salt distribution and sulphuric acid particles.

2.1 The aerosol growth model

The numerical model is based on the general dynamic equation (GDE) which is a partial differential equation for aerosol particle growth (Seinfeld and Pandis, 2006). A sectional method is used to solve the GDE to determine the number distribution n, where bins of variable sizes represent different sizes of the molecular clusters expressed as the number of sulphuric acid molecules in the cluster. The sizes of these bins can be chosen arbitrarily but can limit the integration accuracy. In this work the initial clusters are sampled with each bin representing the addition of one sulphuric acid molecule up to 70 molecules (approx. 3.5 nm) followed by a slowly increasing bin size to around 450 molecules and then the bin size is increased with a factor of 1.1 per bin.

The model includes the production and loss of particles by condensation of sulphuric acid gas onto particles and the coagulation of the individual particle clusters but evaporation is not considered. The condensation coefficients k_i^c are found according to Laakso et al. (2002) with a value of the mass accommodation coefficient of 1 (Laaksonen et al., 2005). The mean free path used to determine k_i^c is found from Lehtinen and Kulmala (2002). The cluster diameter as a function of bin size must also be found. This is nontrivial since the mole fraction of sulphuric acid will change with cluster growth. Here it is assumed that an initial sulphuric acid particle is wet and Seinfeld and Pandis (2006, Chap. 10) is used to determine the cluster diameter and mole fraction as a function of number of sulphuric acid molecules. The coagulation coefficients are

ACPD
9, 22833–22863, 2009

determined from Laakso et al. (2002). These coefficients can be used for all Knudsen numbers and hence in all growth regimes from diameters of a few angstroms to sizes up to >1 microns. The model does not go into the chemistry of the nucleation but assumes that nucleated particles are placed into a predetermined bin at a given rate. This represents stable particle formation by nucleation. The particles are assumed to be 5 molecules big and are thus placed in bin 5 with a cluster formation rate s. The model is described in more detail in Enghoff et al. (2008).

The rate of change of the sulphuric acid concentration is solved by the following equation :

$$\frac{d\mathrm{H_2SO_4}}{dt} = P_{\mathrm{H_2SO_4}} - [\mathrm{H_2SO_4}] \sum_i n_i \cdot k_i^c \quad (1)$$

Here, the first term, $P_{\mathrm{H_2SO_4}}$, is the production of gaseous sulphuric acid and the second term the gas losses to the aerosols by condensation. In Enghoff et al. (2008) the aerosol growth within a small chamber with wall losses was modeled. In the present setup there are no wall losses. Instead losses to primary particles are included in the condensation equations. The losses are discussed in Sect. 3.

2.2 Miex part

Miex is a Mie Scattering program originally developed to model interstellar dust scattering (Wolf, 2004). However, the code works equally well on an ensemble of aerosol particles over a large wavelength range providing that the size distribution of the aerosols and their refractive index is known. We have modified the code to calculate the extinction coefficient σ_{ext} from an ensemble of wet sulphuric acid particles (SAP) with relative humidity 0.5 and with a size distribution given by the aerosol growth model. The database of index of refraction for sulphuric acid particles as a function of wavelength is given by Hess et al. (1998).

Assuming that the concentration of sulphuric acid particles is exponentially decaying with height (h) in the troposphere (extending from 0–10 km) the optical thickness for

ACPD
9, 22833–22863, 2009

wavelength λ can now be calculated from the extinction coefficient:

$$\tau_{SAP}(\lambda) = \sigma_{ext}(\lambda) N_{SAP} \int_0^{10} \exp^{\frac{-h}{Z}} dh, \quad (2)$$

where Z is the scale height and N_{SAP} is the concentration of sulphuric acid particles calculated by the aerosol model.

2.3 OPAC part

OPAC is software tool designed to calculate optical properties for various atmospheric scenarios including changing cloud cover and aerosol distributions (Hess et al., 1998). The sizes and width of aerosol distributions are changed according to their log-normal distributions. Here, the program is used to calculate extinction coefficients and optical thicknesses τ_{SS} for a clean atmosphere with only a marine boundary layer of sea salt particles. The sea salt distribution remains constant throughout each individual run and only serves as a background. The distribution of sea salt particles has both a coarse and accumulation mode given by:

$$\frac{dN(r)}{dr} = \frac{N}{\sqrt{2\pi} r \log\sigma \ln 10} \quad \exp\left[-0.5\left(\frac{\log r - \log r_{mod}}{\log\sigma}\right)^2\right], \quad (3)$$

where σ(coarse/accu) = [2.03/2.03] and r_{mod}(coarse/accu) =[1.75/0.209] μm and Ncoarse/accu = $[3.2 \times 10^{-3}, 20]\,\mathrm{cm}^{-3}$, respectively. These two modes are assumed to be generated by a wind speed of 8.9 m/s (Hess et al., 1998). As will be described later the contribution from sea salt is varied by systematically changing the concentration of the accumulation and coarse mode.

2.4 Optical properties

The time dependent optical thickness for the sulphuric acid particles at different wavelengths is added to the constant optical depth from sea salt and the Angstrom exponent

ACPD
9, 22833–22863, 2009

between two wavelengths is calculated as the slope of log(τ) vs. log log(λ) for the two wavelengths:

$$\alpha(\lambda_1, \lambda_2, t) = -\log \frac{\tau(\lambda_1, t)}{\tau(\lambda_2, t)} \Big/ \log \frac{\lambda_1}{\lambda_2}, \quad (4)$$

where $\tau(\lambda, t)=\tau_{SAP}(t)+\tau_{SS}$. In this study we focus on the wavelengths λ=350 and 450 nm. These wavelengths detect CCN size particles and can be compared to the angstrom exponents as measured by AERONET (Holben et al., 1998). Furthermore the wavelength pair 550 and 900 nm is used to compare with observations from MODIS (Platnick et al., 2003).

3 Sensitivity study

To establish a steady state of background sulphuric acid particles, initially, the sulphuric acid model is run for a month for various constant cluster formation rates (s), constant sulphuric acid production rates ($P_{H_2SO_4}$), and half lives (κ) of nucleated particles against primary particles. These runs provide steady state solutions for the aerosol distribution in a parameter space containing values of s=[0.0001, 0.0005, 0.001, 0.005, 0.01] $cm^{-3}\,s^{-1}$, $P_{H_2SO_4}$=[$1\times10^3, 5\times10^3, 1\times10^4, 2\times10^4$] $cm^{-3}\,s^{-1}$, and κ=[0.5, 1, 1.5, 2, 1000] days. The production values of sulphuric acid were chosen such that the sulphuric acid gas concentration reached peak values of about 1×10^7 cm^{-3} comparable to the values of Kazil et al. (2006) and Weber et al. (2001). Note that this may be at the high end of the sulphuric acid concentration range. The stable cluster production s is more uncertain. The span of values (two orders of magnitude) represents this uncertainty and is within the range mentioned in Pierce and Adams (2007) and Weber et al. (2001).

In order to estimate the losses of sulphuric acid particles to sea salt and other primary particles the time scale for coagulation losses to the sea salt distribution described in Sect. 2.3 was initially estimated. This was done by running the aerosol

ACPD
9, 22833–22863, 2009

growth program with an initial distribution of ultra fine particles and the sea salt distribution described in Sect. 2.3. Omitting condensation, thus only including coagulation, the half time for the losses of the ultrafine particles was estimated to be of the order of half a day. This run represents full mixing between sea salt and sulphuric acid particles and is therefore the upper limit for the coagulation loss of nucleation mode particles to sea salt particles. Under these assumption a range of realistic half-time losses of κ=0.5, 1, 1.5, 2 days was set and the loss constant for the program determined as $\kappa_{par} = \ln(2)/(\kappa \times 60)$. A value of κ=1000 days was also considered as the extreme case where no losses to primary particles are expected. The downside of this approach is that the loss rates has no dependency on particle size.

An additional loss process for particles is rain. On smaller scales rain is a discrete and abrupt process that basically cleans out an area for particles. Since we consider a sort of average over the ocean we have chosen to incorporate losses to rain into our general loss term κ_{par}. General lifetimes for fine particles is days to weeks (Seinfeld and Pandis, 2006, p. 383) which fits well with our choice of loss rates

The 1 month initialization runs provide the starting point for a new run where the cluster production rate, s, is modulated by a Forbush decrease. At t=0 the Forbush decrease is turned on and the aerosol growth is changed over a period of 36 days with a FD minimum after 15 days. The Forbush decrease profile change in ionization *dQ(t)* is created by a mean of five major Forbush decreases (31 October 2003, 13 September 2005, 13 June 1991, 19 January 2005, 15 March 1989) from the Climax Neutron monitor including 15 days before and 20 days after the minimum. This gives a profile, $F(t)$, with a 15% FD decrease minimum (the dotted line in Fig. 2). To create the corresponding relative change in ionization *dQ(t)* it is assumed that a major Forbush decrease is on the same scale as variations in ionization over the solar cycle, i.e. ≈10% (Usoskin et al., 2004) and $F(t)$ is scaled such that the base level is at zero and the minimum is at 10%:

$$dQ(t)(t) = (1. + 0.1 \cdot \frac{F(t) - F(0)}{\max(F(t)) - \min(F(t))}) \quad (5)$$

ACPD
9, 22833–22863, 2009

The aerosol model produces stable clusters at a given unit size. Assuming some form of ion induced nucleation takes place, the production rate, s, must depend on the ionization, Q. Note that we do not consider the specific mechanism of how s depends on Q but only look at the functional form. This makes the study independent of the exact underlying nucleation mechanism.

Three simple schemes are then possible:

- Square root dependency (standard case)
- Linear Dependency
- Additional nucleation mechanisms occuring simultaneously

3.1 Square root dependency

In the standard case s is proportional to the ion concentration, I, which in a steady state situation is proportional to the square root of Q, due to the following relation:

$$\frac{dI}{dt} = Q - \alpha I^2 \tag{6}$$

Nucleation experiments by (Svensmark et al., 2007) have also hinted at a square root dependency and for the main part of the paper we will assume this to be the case, such that when Q is varied throughout a Forbush decrease, s will follow dQ like:

$$s(t) = s_0\sqrt{dQ(t)} \tag{7}$$

3.2 Linear dependency

In the case that larger aerosols are present an additional loss term to account for loss of ions by attachment to these aerosols is added to Eq. (6): $-\beta IN$. If this is the dominating loss term then the steady state solution for the ions become linearly dependent on Q.

ACPD
9, 22833–22863, 2009

To account for this scenario, or an alternate nucleation mechanism, the detailed case shown in Fig. 2 was also run with a direct correlation between s and dQ: $s(t) = s_0 dQ(t)$. Here it is assumed that the stable clusters are directly produced before neutralization by recombination happens.

3.3 Additional nucleation mechanisms occuring simultaneously

Only sulphuric acid ion induced nucleation is simulated in this study. To investigate how other nucleation mechanisms occuring at the same time influence the results, a third nucleation scheme is examined in which $s(t)=0.5\times s_0\sqrt{dQ(t)}+0.5\times s_0$. In this case the last term is not affected by the ionization and thus simulate that additional nucleation mechanisms (such as homogeneous or ternary nucleation) may happen simultaneously.

These alternate schemes allows us to see how the magnitude of change in AE due to the Forbush decrease changes with varying nucleation. If more elaborate schemes for nucleation of stable clusters are taken into account *s(Q)* becomes more complex (Lovejoy et al., 2004; Modgil et al., 2005). For this study the simple relations listed above will suffice and the results are described in Sect. 7.

4 Output of model from a single run

In Fig. 2 the upper plot is the output from a single run with κ=1.5 days, $P_{H_2SO_4}$=20 000 $cm^{-3}\,s^{-1}$, s=0.001 $cm^{-3}\,s^{-1}$ and shows the Angstrom exponent (black line) as a function of the 36 days representing the FD (black dashed). The effective radius (red) as well as the number of H_2SO_4 particles: N_{total} (blue solid), N>3 nm (blue dashed) and N>100 nm (blue point-dashed) is also shown. The two lower plots gives the optical depths at λ=350 and 450 nm used to calculate the upper plot.

For this choice of parameters it is observed how the Angstrom exponent decreases by ≈2% to a minimum approximately 3 days after the FD minimum. The explanation

ACPD
9, 22833–22863, 2009

is that at the onset of the FD the cluster production, s, and hence the number of small particles decreases. Since the loss rate remains constant this causes the total particle number to decrease and a subsequent minimum in τ_{350} is observed around the time of the FD minimum. A couple of days after the FD minimum the optical depth for λ=350 nm returns to its initial value. Note that this happens several days before the particle number returns to its original value. The reason being that as the number of particles go down, the remaining ones increase in size, due to reduced competition for the sulphuric acid. As the particle radius increases, so does the optical thickness. The same pattern is observed for λ=450 nm, however the optical depth increases above its original value, before it relaxes back. This is due to a higher sensitivity to the particle radius, since this wavelength is further away from the effective radius of the particle population (174 nm). The difference in behaviour for the optical thickness at the two wavelengths show the complex dependence of the AOT on particle number and radius. Furthermore this is the reason for the observed lag of 3 days in the dip of the AE compared to the dip in the FD. An obvious interpretation of this lag, if seen in observational data, would be to attribute it to the time it takes from the decrease in production of small particles to propagate up to sizes detectable at the employed wavelengths. Our analysis, however, shows that this is not the only possible explanation, but that the increase in radius of the remaining population must also be considered.

5 Output of model from parameter space

In Fig. 3 the whole parameter space is explored. Each box represents a value of s and $P_{H_2SO_4}$. In each box the colors represent the loss values of κ=0.5, 1, 1.5, 2, 1000 days increasing from a value of 0.5 days (bottom) to 1000 days (top). For each loss value the first number gives the base level of the Angstrom exponent defined as the mean of the first 10 days of Angstrom exponent output (t=−15 to −5 in Fig. 3). The second number is then the per mille deviation of the largest extremum of day −5–20 from the base level, with positive numbers meaning an increase in AE and vice versa. The two

ACPD
9, 22833–22863, 2009

following numbers are the mean of the 10 first days of the effective radius in nm and sulphuric acid concentration in cm^{-3} (divided by 10^7), respectively.

Three types of responses are behind the different percentage responses. The standard case is the one outlined in Sect. 4 where a small dip appears in the Angstrom exponent. However, in a few cases the choice of input parameters gives a peak in the Angstrom exponent indicating that a decrease in small particle population may also lead to increases in AE. This happens when the effective radius gets below a certain point around 80 nm (depending somewhat on s and $P_{H_2SO_4}$), far away from the probing wavelengths of 350 and 450 nm. A switch in sensitivity then seems to happen causing the low wavelength to be more sensitive to the change in effective radius than the high wavelength, as opposed to what was seen in the single run of Sect. 4. Since the AOT at 350 nm then increases the most as the radius of the particle population grows, this causes an increase in the AE. The third response is the case where no mixing occurs (κ=1000 days). Here very large changes in the AE is typically observed. These rather large percentage changes are more a result of an unstable initial precondition run than a real decrease in Angstrom exponent caused by the modulation of cluster production. When there is no loss for the particles, steady state is never reached and therefore the effective radius continues to grow, causing a decrease of the AE, throughout these runs. Since the AE is then much lower after the FD, simply because of this overall growth of the population, artificially high changes appear. The runs with κ=1000 days should generally be regarded with care.

For a constant loss rate and cluster production an increase in $P_{H_2SO_4}$ in general leads to higher Angstrom exponent base level. This is explained by the larger increase in available condensable gas enabling better growth of the smaller particles. This will cause the optical depth to increase for 350 nm and hence the Angstrom exponent to increase. Note also that the effective radius increases with $P_{H_2SO_4}$, in all cases. However, if the effective radius gets too high then an increase in $P_{H_2SO_4}$ can cause a decrease in AE level since the sensitivity of the AOT at 450 starts to increase. Similarly, for a constant sulphuric acid and cluster production an increase in κ leads to higher Angstrom

ACPD
9, 22833–22863, 2009

exponent base level. This is natural since higher half lives results in fewer small particles being removed.

And again, for a constant loss rate and sulphuric acid production an increase in s in general leads to higher Angstrom exponent base level. This is explained by an increase in the number concentration of smaller particle, causing the AOT at 350 nm to increase at a higher rate than at 450 nm. Additionally a high s leads to a decrease in effective radius, due to an increased competition for the sulphuric acid. In a few cases this actually causes the AE to decrease as s increases (for instance for $P_{H_2SO_4}$ =1000.0 cm^{-3} s^{-1} and s going from 0.00500 to 0.01000 cm^{-3} s^{-1}.

As can be observed the baseline values vary from small negative numbers to a maximum around 1.4 in Angstrom exponent. In Sano (2004) the average Angstrom exponent over the ocean is about 0.5. In Kazil et al. (2006) and Weber et al. (2001) the sulphuric acid concentration over the oceans was found based on both modelling and measurements. Here values of sulphuric acid concentration in the lower troposphere over the ocean was about 10^7 cm^{-3}. If these values are compared with our results this can be used to restrict the solution space of sulphuric acid production and cluster production to the region 0.0005 cm^{-3} s^{-1} ≤ s ≤0.001 cm^{-3} s^{-1} and $P_{H_2SO_4}$ ≥5000 cm^{-3} s^{-1} and the region 0.005 cm^{-3} s^{-1} ≤ s ≤0.01 cm^{-3} s^{-1} with $P_{H_2SO_4}$ =5000 cm^{-3} s^{-1}. This region is shaded in grey in the figure and indicates the most probable optical response in the marine troposphere to Forbush decreases under the assumption of a square root dependency of the cluster formation rate to the ion production. As can be observed the expected average change in percentage of the Angstrom exponent is of the order of −6 to 3% in the shaded region, compared to the initial 10% modulation in ionization.

The AE change is a function of the relative change in the two optical depths. These in turn depend strongly on particle size and number. Ignoring negative AE base levels and those very close to 0 there does seem to be some trends in the AE change. When the effective radius increase so does the AE change (for constant half-lifes). This is seen clearly, for instance, for $P_{H_2SO_4}$ going from 5000 cm^{-3} s^{-1} to 20 000 cm^{-3} s^{-1}, for all half-lives. When R_{eff} goes below a certain limit, around 80 nm as noted above, the change

ACPD
9, 22833–22863, 2009

switches from negative to positive. An example of this is for $P_{H_2SO_4}$=5000 cm^{-3} s^{-1} and s going from 0.001 to 0.005 cm^{-3} s^{-1}. These results indicate that wavelengths close to the effective radius of the particle population are best suited for making observations of the response in AE to Forbush decreases.

Finally, a similar analysis was performed for the wavelength pair of 550–900 nm. The reason for selecting this wavelength pair is that the MODIS instrument (Platnick et al., 2003) as well as AERONET measures these or similar wavelength pairs. However, this wavelength pair probes sizes of the particle distribution where almost no particles remain. Therefore smaller decreases or increases (of the order of maximum 1%) in the Angstrom exponent are observed. This will be elaborated on in Sect. 8 where the model results are compared with observations.

6 Modifying the sea salt distribution

The sea salt modes used in this study are described in Sect. 2.3. In this section we examine the sensitivity of our results to changes in these modes.

Natural sea salt can have a wide range of sizes (Pierce and Adams, 2006), from a few nano meter (Clarke et al., 2006) and up to micrometers (O'Dowd et al., 1999). Due to limitations in the available data for refractive indices we have limited our sensitivity study to variations in the two modes provided by OPAC. Firstly a run, based on the case in Fig. 2, was made where all sea salt was removed, to gauge the overall contribution of the sea salt to the optical parameters. The AE increased from 0.72 to 1.14 which is well in line with the understanding that smaller particles yield higher AE. The optical thicknesses at 350 nm and 450 nm dropped by 0.045 and 0.046, respectively. The base values were 0.156 and 0.130, meaning that the sea salt contributes 29% to the optical thickness at 350 nm and 36% at 450 nm.

Figure 4 shows the output of 9 different runs, again based on the case in Fig. 2, where the number density of the two sea salt modes have been varied. Both modes

ACPD
9, 22833–22863, 2009

have been run with its standard value *(st)* provided by OPAC, a 50% decrease (d50), and a 50% increase (i50), producing the 9 plots shown in the figure, such that d50i50 means that the accumulation mode has been decreased by 50% and the coarse mode increased similarly. The strongest response in the AE comes from changes in the accumulation mode, which is to be expected since the median size of this mode (209 nm) is much closer to the wavelengths used to find the AE (350 nm and 450 nm) compared with the coarse mode (1.75 μm). Changing the accumulation mode of sea salt by 50% in either direction shifts the baseline of the AE by about 20%. Similar changes in the coarse mode only yields very small changes in the AE.

Interestingly the dip in AE due to the Forbush decrease seems to be more or less undisturbed by the changes in sea salt, changing from 2.2% in the d50d50 case to 2.3% for i50i50. For the run with no sea salt the dip is also 2.2%. To investigate this further a run was made where the amount of sea salt was increased to an amount corresponding to a high wind speed of 18 m^2. This was done using the empirical law found by Mulcahy et al. (2008), stating that the marine aerosol optical thickness scales with the square of the windspeed. The AE thus decreased to 0.28 and the dip increased to 2.7%. These runs show that the amount of sea salt mostly serves as a sort of baseline change to the optical thickness and thus AE, whereas the dip in the AE is not affected greatly. The caveat here is that a change in sea salt would normally be accompanied by a change in loss rate for the nucleated particles, which is not modeled here. Instead effects of changing loss rates are looked at separately in Sect. 5.

7 Modifying cluster formation rate

The responses shown in the previous section are dependent on how ionization influences cluster formation. Based on results from Svensmark et al. (2007) a square root dependency of the cluster formation rate was assumed (see Sect. 3). This however is still an open question and it is therefore natural to investigate other mechanisms. This section indicates how other mechanisms may influence the results of the two previous

ACPD
9, 22833–22863, 2009

sections.

Figure 5 shows the result from the single run (see Sect. 4) with the two alternate nucleation schemes as presented in Sect. 3. The left plot is identical to upper plot in Fig. 2. In the middle plot a linear dependency of the cluster formation rate to the ionization is examined. Here it can be seen that removing the square root dependency increases the dip in Angstrom exponent by about 50% due to the larger variations in cluster formation rate. In the right plot the cluster formation is again assumed to have a square root dependency and additionally 50% of the perturbation by the FD is now removed by adding a constant term to the time varying cluster production. Here the response goes down with about 50%. This means that the effect of Forbush decreases is dependent on both how ionization affect nucleation as well as the ratio of effectiveness of the different competing nucleation mechanisms in the marine troposphere.

8 Comparison with observations

Svensmark et al. (2009) made an epoch analysis of AERONET data from 5 major FD events. Angstrom exponent data (340–440 nm) from approximately 40 stations (stations with more than 20 measurements a day) were superposed and averaged over the 5 events (31 October 2003, 13 September 2005, 19 January 2005, 16 July 2000, 12 April 2001). In this section we compare those results with the model runs. Additionally we investigate the wavelength pair 550, 900 nm which can be compared with both AERONET and MODIS data.

The left of Fig. 6 shows a comparison of Angstrom exponents for the short wavelength pair from the model (350, 450 nm) and from the average of the 5 FDs from AERONET (340, 440 nm). The right of Fig. 6 shows the wavelength pairs AERONET (500, 870 nm), MODIS (550, 865 nm), and Model (550, 900 nm). The dashed line is the average of the FD signal over the events listed above. First, it is observed that the values for AERONET are higher than the values for both the model and MODIS. This is because the land based AERONET stations have more small mode fraction particles

ACPD
9, 22833–22863, 2009

due to aerosols from e.g. pollution, dust, and biomass burnings. [1]

The left figure shows a slight significant signal for the short wavelength pair for AERONET where a decrease in the Angstrom exponent is observed a couple of days after the FD minimum for the 5 events. However, for the longer wavelength pairs in the right figure both for MODIS and AERONET no significant signal seem to be present. Since we are comparing an ocean based model with land based observations no direct comparison can be made but we can however point to some trends. There is a systematic decrease of a factor of approximately 2–4 in signal for going from the small wavelength pair to the larger in our model. Assuming that the weak signal observed in Svensmark et al. (2009) is real then the signal from the long wavelength pairs could be lowered into the climatic noise of the Angstrom exponent observations. If a linear dependency of the cluster formation rate is assumed this effect would even be more pronounced (see Sect. 7). This seems to be confirmed by the left of Fig. 6 although more observations would be needed to examine this in more detail. Therefore if an ion induced mechanism is working as in our model, it is expected that observations based on the shorter wavelength pair would be the most favourable for seeing the FD effect.

9 Summary

Under the assumption that ion induced nucleation play a role in the marine troposphere, a simple aerosol growth model in combination with a Mie scattering code and an optical properties program was used to model Angstrom exponents over the tropospheric ocean for two wavelength pairs (350, 450 nm and 550, 900 nm) during a Forbush decrease by modulating the nucleation rate over time by the ionization profile from the Forbush decrease. The marine environment was modeled by a fixed-in-time

[1] Note that the FD events are not identical to the ones used in the model but that the average of the peak is more or less the same. For the purpose of this exercise this is more than adequate.

ACPD
9, 22833–22863, 2009

bimodal sea salt distribution and a variable sulphuric acid aerosol distribution. A large parameter space was explored by altering nucleation mode cluster production rates, sulphuric acid production, loss rates, as well as exploring alternative nucleation mechanism. Distinct but highly varying responses in the optical properties were found by changing the initial parameter settings. For the short wavelength pair (350, 450 nm) changes in the Angstrom exponent of about −6 to 3% was found for realistic settings of the Angstrom exponent base level values and sulphuric acid concentration as compared to the marine troposphere. For the longer wavelength pair (550, 900 nm) the changes were generally a factor of 2–4 lower. This seems to match with observations from AERONET and MODIS were an epoch analysis of 5 major FD event reveal a slight significant signal in the wavelength pair (340, 440 nm) and not in the longer wavelength pair (550, 900 nm).

The study encourages more global observations of Angstrom exponents at smaller wavelength pairs and improving the signal to noise ratio further. This may help to improve the understanding of the importance of ion induced nucleation and of how secondary aerosol distributions affect the marine optical properties. Future work related to the model should focus on implementing a dynamic sea salt distribution and investigating other nucleation schemes and growth rates further.

References

Arnold, F.: Multi-ion complexes in the stratosphere – Implications for trace gases and aerosol, Nature, 284, 610–611, 1980. 22836

Cane, H.: Coronal mass ejections and forbush decreases, Space Sci. Rev., 93, 55–77, 2000. 22835

Clarke, A., Owens, S., and Zhou, J.: An ultrafine sea-salt flux from breaking waves: Implications for cloud condensation nuclei in the remote marine atmosphere, J. Geophys. Res.-Atmos., 111, doi:10.1029/2005JD006565, 2006. 22848

Eichkorn, S., Wilhelm, S., Aufmhoff, H., Wohlfrom, K. H., and Arnold, F.: Cosmic ray-induced

ACPD

9, 22833–22863, 2009

aerosol-formation: First observational evidence from aircraft-based ion mass spectrometer measurements in the upper troposphere, Geophys. Res. Lett., 29, 43–1, 2002. 22836
Enghoff, M. B., Pedersen, J. O. P., Bondo, T., Johnson, M. S., Paling, S., and Svensmark, H.: Evidence for the Role of Ions in Aerosol Nucleation, J. Phys. Chem. A, 112, 10305–10309, doi:10.1021/jp806852d, 2008. 22836, 22839
Forbush, S. E.: On the Effects in Cosmic-Ray Intensity Observed During the Recent Magnetic Storm, Physical Review, 51, 1108–1109, doi:10.1103/PhysRev.51.1108.3, 1937. 22835
Harrison, R. G. and Stephenson, D. B.: Empirical evidence for a nonlinear effect of galactic cosmic rays on clouds, Proceedings of the Royal Society A, 462, 1221–1233, 2006. 22835
Hess, M., Koepke, P., and Schult, I.: Optical Properties of Aerosols and Clouds: The Software Package OPAC., B. Am. Meteorol. Soc., 79, 831–844, doi:10.1175/1520-0477(1998)079, 1998. 22837, 22839, 22840
Hirsikko, A., Yli-Juuti, T., Neiminen, T., Vartiainen, E., Laakso, L., Hussein, T., and Kulmala, M.: Indoor and outdoor air ions and aerosol particles in the urban atmosphere of Helsinki: characteristics, sources and formation, Boreal Environ. Res., 12, 295–310, 2007. 22836
Holben, B., Eck, T., Slutsker, I., Tanré, D., Buis, J., Setzer, A., Vermote, E., Reagan, J., Kaufman, Y., Nakajima, T., Lavenu, F., Jankowiak, I. and Smirnov, A.: AERONET – A federated instrument network and data archive for aerosol characterization, Rem. Sens. Environ, 66, 1–16, 1998. 22836, 22841, 22857
Kazil, J., Lovejoy, E. R., Barth, M. C., and O'Brien, K.: Aerosol nucleation over oceans and the role of galactic cosmic rays, Atmos. Chem. Phys., 6, 4905–4924, 2006, http://www.atmos-chem-phys.net/6/4905/2006/. 22841, 22847
Kim, T. O., Adachi, M., Okuyama, K., and Seinfeld, J. H.: Experimental Measurement of Competitive Ion-Induced and Binary Homogeneous Nucelation in $SO_2/H_2O/N_2$ Mixtures, Aerosol Sci. Tech., 26, 527–543, 1997. 22836
Kniveton, D. R.: Precipitation, cloud cover and Forbush decreases in galactic cosmic rays, J. Atmos. Terr. Phys., 66, 1135–1142, 2004. 22835
Kristjánsson, J. E., Stjern, C. W., Stordal, F., Fjraa, A. M., Myhre, G., and Jónasson, K.: Cosmic rays, cloud condensation nuclei and clouds a reassessment using MODIS data, Atmos. Chem. Phys., 8, 7373–7387, 2008, http://www.atmos-chem-phys.net/8/7373/2008/. 22835
Kuang, C., McMurry, P. H., and McCormick, A. V.: Determination of cloud condensation nuclei production from measured new particle formation events, Geophys. Res. Lett., 36, 9,

doi:10.1029/2009GL037584, 2009. 22837
Kulmala, M., Riipinen, I., Sipilä, M., Manninen, H. E., Petäjä, T., Junninen, H., Dal Maso, M., Mordas, G., Mirme, A., Vana, M., Hirsikko, A., Laakso, L., Harrison, R. M., Hanson, I., Leung, C., Lehtinen, K. E. J., and Kerminen, V.-M.: Toward Direct Measurement of Atmospheric Nucleation, Science, 318, 89–92, doi:10.1126/science.1144124, 2007. 22836
Laakso, L., Mäkelä, J. M., Pirjola, L., and Kulmala, M.: Model studies on ion-induced nucleation in the atmosphere, J. Geophys. Res. Atmos., 107, 4427–4445, doi:10.1029/2002JD002140, 2002. 22836, 22838, 22839
Laakso, L., Gagné, S., Petäjä, T., Hirsikko, A., Aalto, P. P., Kulmala, M., and Kerminen, V.-M.: Detecting charging state of ultra-fine particles: instrumental development and ambient measurements, Atmospheric Chemistry and Physics, 7, 1333–1345, 2007. 22836
Laaksonen, A., Vesala, T., Kulmala, M., Winkler, P. M., and Wagner, P. E.: Commentary on cloud modelling and the mass accommodation coefficient of water, Atmos. Chem. Phys., 5, 461–464, 2005, http://www.atmos-chem-phys.net/5/461/2005/. 22838
Lee, S.-H., Reeves, J. M., Wilson, J. C., Hunton, D. E., Viggiano, A. A., Miller, T. M., Ballenthin, J. O., and Lait, L. R.: Particle Formation by Ion Nucleation in the Upper Troposphere and Lower Stratosphere, Science, 301, 1886–1889, doi:10.1126/science.1087236, 2003. 22836
Lehtinen, K. E. J. and Kulmala, M.: A model for particle formation and growth in the atmosphere with molecular resolution in size, Atmos. Chem. Phys. Discuss., 2, 1791–1807, 2002, http://www.atmos-chem-phys-discuss.net/2/1791/2002/. 22838
Lovejoy, E. R., Curtius, J., and Froyd, K. D.: Atmospheric ion-induced nucleation of sulfuric acid and water, J. Geophys. Res. Atmos., 109, 1–11, doi:10.1029/2003JD004460, 2004. 22836, 22844
Marsh, N. and Svensmark, H.: Galactic cosmic ray and El Niño-Southern Oscillation trends in International Satellite Cloud Climatology Project D2 low-cloud properties, J. Geophys. Res. Atmos., 108, 4195–4205, doi:10.1029/2001JD001264, 2003. 22835
Modgil, M., Kumar, S., Tripathi, S., and Lovejoy, E.: A parameterization of ion-induced nucleation of sulphuric acid and water for atmospheric conditions, J. Geophys. Res. Atmos., 110, 19, doi:10.1029/2004JD005475, 2005. 22844
Mulcahy, J. P., O'Dowd, C. D., Jennings, S. G., and Ceburnis, D.: Significant enhancement of aerosol optical depth in marine air under high wind conditions, Geophys. Res. Lett., 35, doi:10.1029/2008GL034303, 2008. 22849

ACPD
9, 22833–22863, 2009

O'Dowd, C., McFiggans, G., Creasey, D. J., Pirjola, L., Hoell, C., Smith, M. H., Allan, B. J., Plane, J. M. C., Heard, D. E., Lee, J. D., Pilling, M. J., and Kulmala, M.: On the photochemical production of new particles in the coastal boundary layer, Geophys. Res. Lett., 26, 1707–1710, doi:10.1029/1999GL900335, 1999. 22848

Pierce, J. and Adams, P.: Global evaluation of CCN formation by direct emission of sea salt and growth of ultrafine sea salt, J. Geophys. Res. Atmos., 111, D06203, doi:10.1029/2005JD006186, 2006. 22848

Pierce, J. R. and Adams, P. J.: Efficiency of cloud condensation nuclei formation from ultrafine particles, Atmos. Chem. Phys., 7, 1367–1379, 2007, http://www.atmos-chem-phys.net/7/1367/2007/. 22837, 22841

Pierce, J. R. and Adams, P. J.: Can cosmic rays affect cloud condensation nuclei by altering new particle formation rates?, online available at: http://dx.doi.org/10.1029/2009GL037946 Geophys. Res. Lett., 36, L09820+, doi:10.1029/2009GL037946, 2009. 22837

Platnick, S., King, M. D., Ackerman, S. A., Menzel, W. P., Baum, B. A., Riedi, J. C., and Frey, R. A.: The MODIS cloud products: algorithms and examples from terra, IEEE Transactions on Geoscience and Remote Sensing, 41, 459–473, doi:10.1109/TGRS.2002.808301, 2003. 22837, 22841, 22848

Pudovkin, M. I. and Veretenenko, S. V.: Cloudiness decreases associated with Forbush decreases of galactic cosmic rays., J. Atmos. Terr. Phy., 57, 1349–1355, 1995. 22835

Sano, I.: Optical thickness and Angstrom exponent of aerosols over the land and ocean from space-borne polarimetric data, Adv. Space Res., 34, 833–837, 2004. 22847

Schuster, G. L., Dubovik, O., and Holben, B. N.: Angstrom exponent and bimodal aerosol size distributions, J. Geophys. Res. Atmos., 111, 14 pp., doi:10.1029/2005JD006328, 2006. 22836

Seinfeld, J. and Pandis, S.: Atmospheric Chemsitry and Physics : From Air Pollution to Climate Change, Wiley, 2 edn., 2006. 22838, 22842

Sloan, T. and Wolfendale, A. W.: Testing the proposed causal link between cosmic rays and cloud cover, Environ. Res.Lett., 3, p. 024001, doi:10.1088/1748-9326/3/2/024001, 2008. 22835, 22836

Svensmark, H., Pedersen, J. O. P., Marsh, N. D., Enghoff, M. B., and Uggerhøj, U. I.: Experimental evidence for the role of ions in particle nucleation under atmospheric conditions, P. Roy. Soc. A, 463, 385–396, doi:10.1098/rspa.2006.1773, 2007. 22843, 22849

Svensmark, H., Bondo, T., and Svensmark, J.: Cosmic ray decreases affect atmospheric

ACPD

9, 22833–22863, 2009

aerosols and clouds, online available at: http://dx.doi.org/10.1029/2009GL038429 Geophys. Res. Lett., 36, L15101+, doi:10.1029/2009GL038429, , 2009. 22835, 22836, 22850, 22851

Tinsley, B. A.: The global atmospheric electric circuit and its effects on cloud microphysics, Rep. Prog. Phys., 71, p. 066801, doi:10.1088/0034-4885/71/6/066801, 2008. 22835

Todd, M. C. and Kniveton, D. R.: Short-term variability in satellite-derived cloud cover and galactic cosmic rays: an update, J. Atmos. Terr. Phys., 66, 1205–1211, 2004. 22835

Usoskin, I. G., Gladysheva, O. G., and Kovaltsov, G. A.: Cosmic ray-induced ionization in the atmosphere: spatial and temporal changes, J. Atmos. Sol.-Terr. Phys., 66, 1791–1796, doi:10.1016/j.jastp.2004.07.037, 2004. 22842

Weber, R. J., Chen, G., Davis, D. D., Mauldin III, R. L., Tanner, D. J., Eisele, F. L., Clarke, A. D., Thornton, D. C., and Bandy, A. R.: Measurements of enhanced H_2SO_4 and 3–4 nm particles near a frontal cloud during the First Aerosol Characterization Experiment (ACE 1), J. Geophys. Res., 106, 24107–24117, doi:10.1029/2000JD000109, 2001. 22841, 22847

Winkler, P. M., Steiner, G., Vrtala, A., Vehkamaki, H., Noppel, M., Lehtinen, K. E. J., Reischl, G. P., Wagner, P. E., and Kulmala, M.: Heterogeneous nucleation experiments bridging the scale from molecular ion clusters to nanoparticles, Science, 319, 1374–1377, doi:10.1126/science.1149034, 2008. 22836

Wolf, S.: Mie Scattering by Ensembles of Particles with Very Large Size Parameters, Comput. Phys. Commun., 162, 113–123, 2004. 22837, 22839

Yu, F.: From molecular clusters to nanoparticles: second-generation ion-mediated nucleation model, Atmos. Chem. Phys., 6, 5193–5211, 2006, http://www.atmos-chem-phys.net/6/5193/2006/. 22836

Table 1. List of abbreviations.

AE	Angstrom exponent
AERONET	Aerosol Robotics Network (Holben et al., 1998)
AOT	Aerosol Optical Thickness
FD	Forbush decrease
I	Ion concentration
ISCCP	International Satellite Cloud Cover Project
κ	Half life of particles
κ_{par}	Loss rate of particles
k_i^c	Condensation coefficient
$k_{i,j}^e$	Coagulation coefficient
MODIS	Moderate Resolution Imaging Spectroradiomete
n_i	Particle number
$P_{H_2SO_4}$	Production rate of sulphuric acid
Q	Ionisation rate
s	Production rate of stable clusters
SAP	Sulphuric Acid Particles
τ	Optical thickness

ACPD
9, 22833–22863, 2009

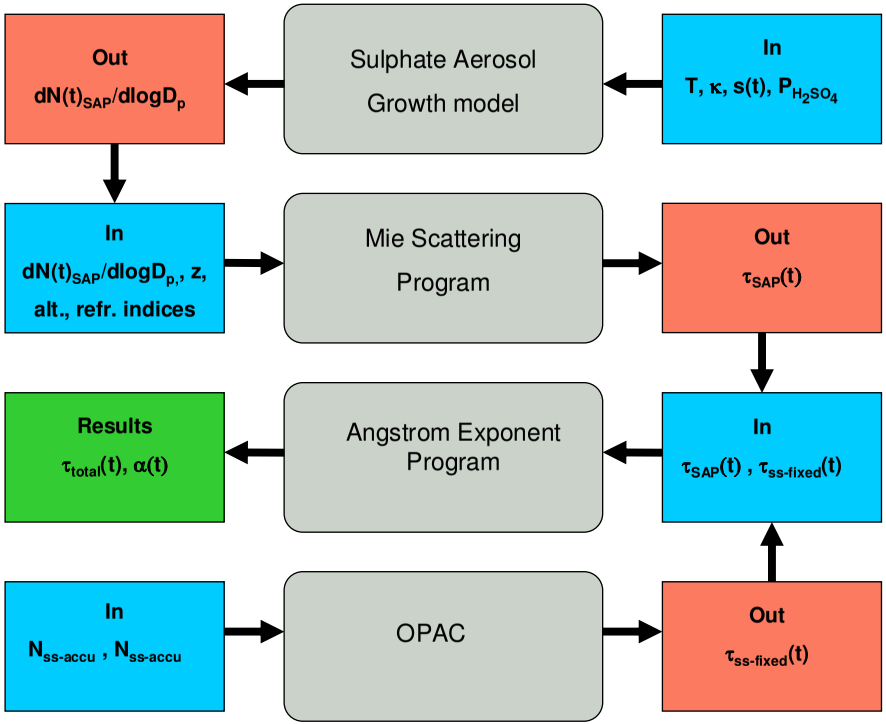

Fig. 1. Flowchart of the theoretical model based on 4 steps. Definitions of input and outputs. See text for more details.

ACPD
9, 22833–22863, 2009

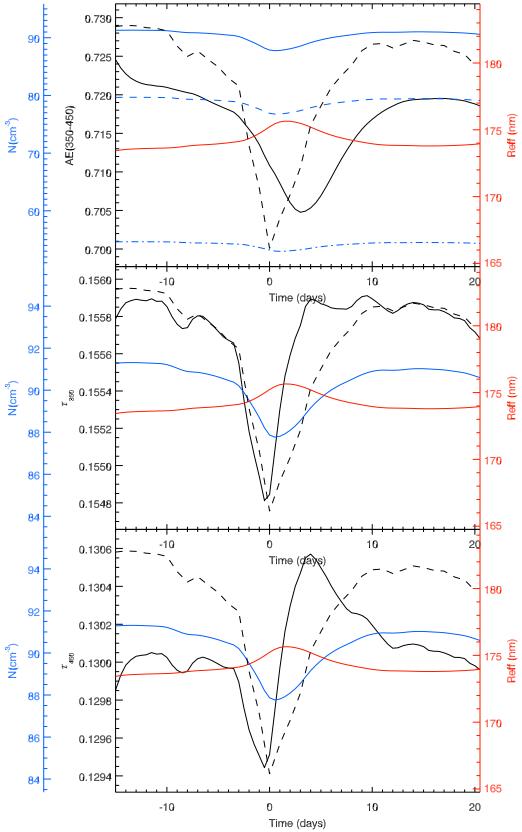

Fig. 2. The upper plot is model output from a single run with κ=1.5 days, p=20000 cm^{-3} s^{-1}, s=0.001 cm^{-3} s^{-1} and shows the Angstrom exponent (black line) over 36 days for the FD (black dashed). The effective radius (red) and the number of H_2SO_4 particles: N_{total} (blue solid), N>3 nm (blue dashed) and N>100 nm (blue point-dashed) are also shown. The two lower plots show the optical depths at λ=350 nm and 450 nm.

ACPD
9, 22833–22863, 2009

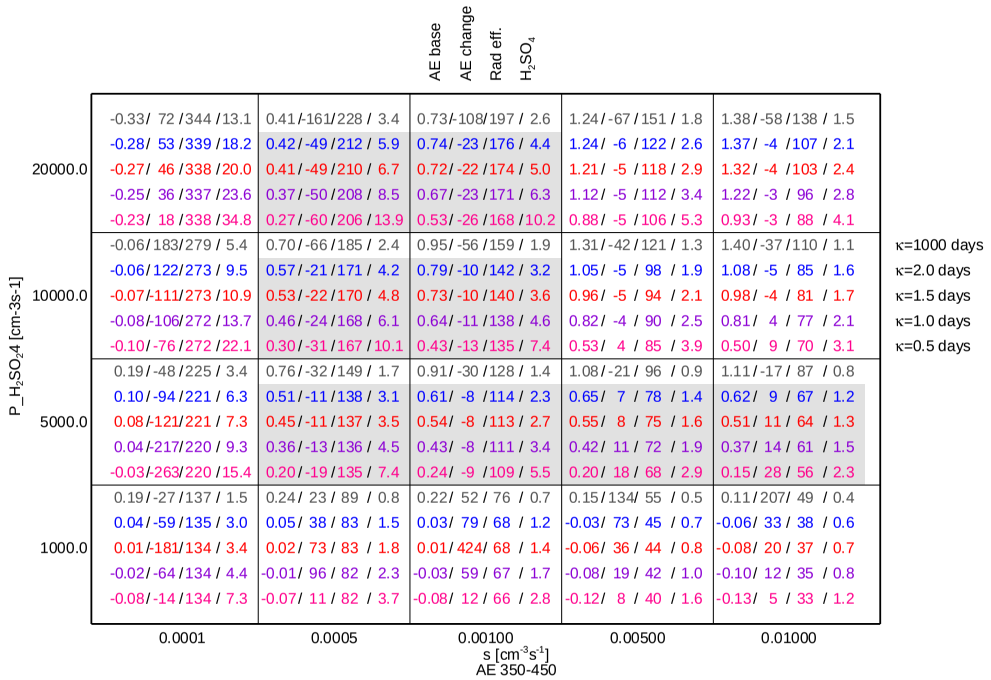

Fig. 3. Model overview of the sensitivity study of various optical parameters and sulphuric acid concentrations as function of loss rates, sulphuric acid production rates and cluster production rates as described in Sect. 5. Each box represents a value of s and $P_{H_2SO_4}$. In each box the colors represent the loss values of κ=0.5, 1, 1.5, 2, 1000 days increasing from a value of 0.5 days (bottom) to 1000 days (top). For each loss value the first number gives the base level of the Angstrom exponent defined as the mean of the first 10 days of Angstrom exponent output (t=−15 to −5 days). The second number is the per mille deviation of the largest extremum of days −5 to 20 from the base level. Positive numbers mean an increase in AE and vice versa. The two following numbers are the mean of the 10 first days of the effective radius in nm and sulphuric acid concentration in cm^{-3} (divided by 10^7), respectively.

ACPD
9, 22833–22863, 2009

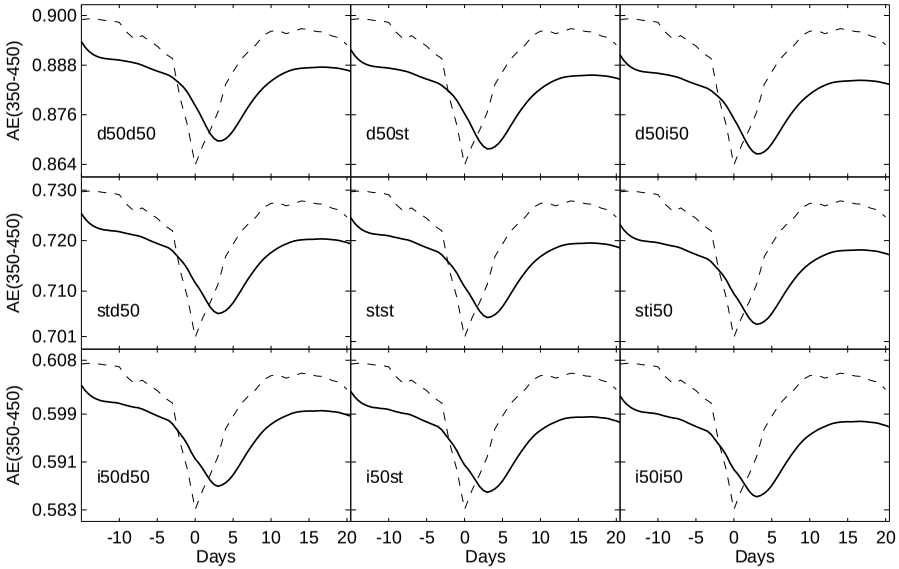

Fig. 4. Variations of the sea salt distribution. This figure shows the output of 9 runs, based on the run described in Sect. 4, but with different levels of sea salt. d50 refers to a 50% decrease in a mode, *st* to the standard value, and i50 to a 50% increase. The accumulation mode is listed first and the coarse mode last. The full line shows the AE, the dotted line the FD profile.

ACPD
9, 22833–22863, 2009

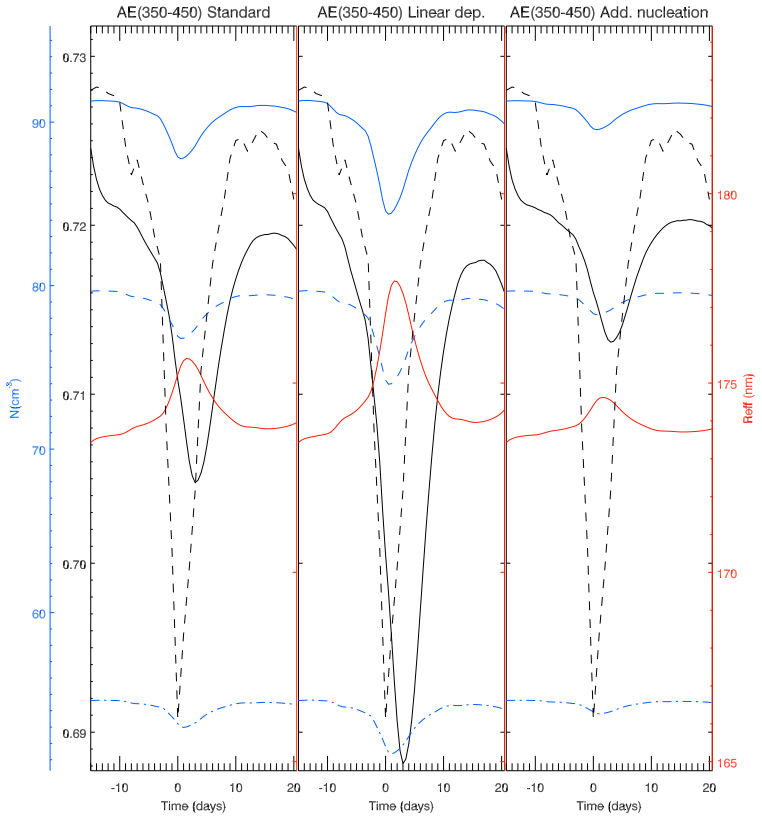

Fig. 5. Alternate nucleation schemes as described in Sect. 7. The figure is based on Fig. 2 with: (left) standard case, (middle) linear cluster formation dependency (right) 50% alternative nucleation.

ACPD
9, 22833–22863, 2009

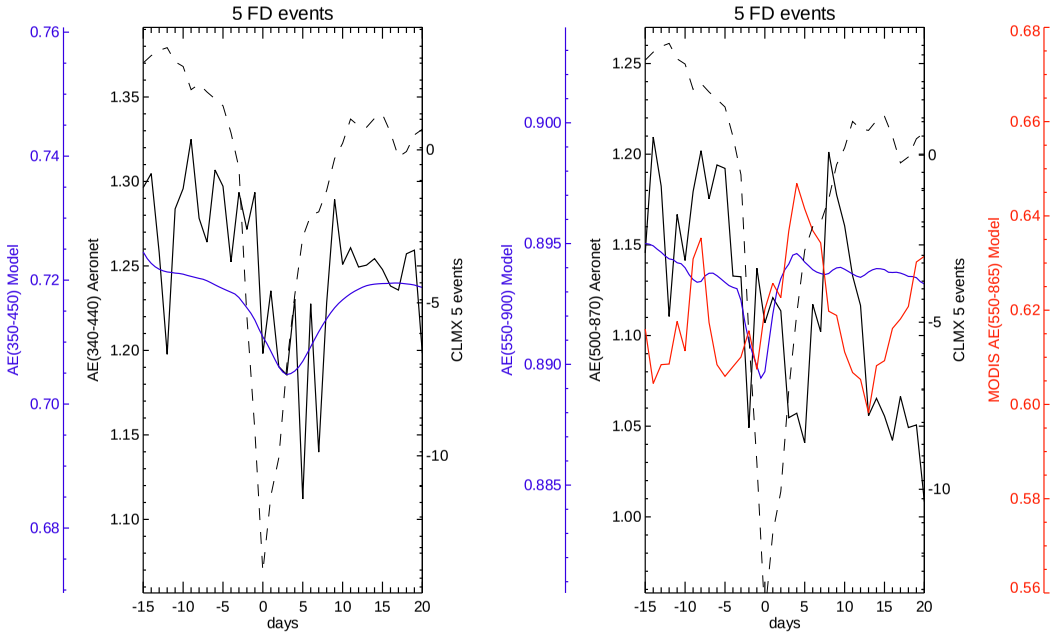

Fig. 6. Angstrom exponents from model and observations (MODIS and AERONET) for short wavelength pairs and long wavelength pairs. The observations are based on an epoch analysis where the signal from 5 FD events are superposed and averaged for each day.

ACPD
9, 22833–22863, 2009

DTU Space
National Space Institute
Technical University of Denmark

Juliane Maries Vej 30
DK-2100 København Ø

Tel. +45 3532 5700
Fax +45 3536 2475

www.space.dtu.dk